Nonclassical correlations in the motion of dissociated Feshbach molecules

Dissertation der Fakultät für Physik
der Ludwig-Maximilians-Universität München

vorgelegt von Clemens Gneiting
aus Heilbronn

München, den 1. Februar 2010

1. Gutachter: Dr. Klaus Hornberger

2. Gutachter: Prof. Dr. Ulrich Schollwöck

Tag der mündlichen Prüfung: 12. März 2010

Zusammenfassung

Der Nachweis nichtklassischer Eigenschaften in der Quantenmechanik spielt eine zentrale Rolle für deren Konsolidierung und stellt nach wie vor ein aktuelles Forschungsgebiet dar. In dieser Dissertation schlage ich zwei eigenständige Szenarien zur Beobachtung von Bell-Korrelationen in der Bewegung zweier makroskopisch separierter Materieteilchen vor. Damit würden wesentliche Charakteristika für Nichtklassizität, nämlich quantenmechanische Verschränkung und das Superpositionsprinzip, einem System mit unmittelbarer klassischer Interpretation aufgeprägt.
Beide Szenarien verwenden die graduelle Dissoziation ultrakalter Feshbach-Moleküle und führen zur makroskopischen Delokalisierung der einzelnen Atome. Ich beschreibe die jeweiligen Abläufe, einschließlich der optischen Führung der Wellenpakete und deren interferometrische Verarbeitung, bis hin zu den abschließenden Ortsmessungen. In beiden Fällen wird die Möglichkeit, eine Bell-Ungleichung zu verletzen, untersucht. Dies geschieht zunächst in einem allgemein gehaltenen Rahmen, mit dem Ziel, den störenden Einfluss der dispersiven Zeitentwicklung zu verstehen. Anschließend entwickle ich eine gekoppelte Kanal-Beschreibung der Feshbach-Dissoziation; aufbauend auf dieser wird dann die Möglichkeit einer Bell-Verletzung mit geeignet gewählten, experimentell realisierbaren Dissoziationszuständen nachgewiesen. In der vorgeschlagenen experimentellen Umsetzung ließen sich Delokalisierungen und inter-atomare Abstände auf der Größenordnung von Zentimetern erreichen.

Abstract

This thesis proposes two complementary scenarios to observe Bell correlations in the motion of two macroscopically separated material particles. Both are based on the gradual dissociation of ultracold Feshbach molecules and result in macroscopic delocalizations of the single-atom states. By giving a full account of these scenarios, including the coupled-channel description of the Feshbach dissociation, the optically guided dispersive propagation, interferometric processing and the final position measurements, I demonstrate for both cases their potential to violate a Bell inequality under experimentally viable conditions that correspond to delocalizations and interatomic separations on the order of centimeters.

I am indebted to my advisor Klaus Hornberger for his continuous support and encouragement. It was a great pleasure to work with him, since he would always listen to my questions and problems and had confidence in my progress. He guided me, but still left me the freedom to develop my own ideas and follow my own line of thoughts.
I am also grateful to my colleagues from the quantum optics group, in particular to Johannes Trost, whom I was happy to share the office with for many years. I benefited from his expertise in many helpful discussions. Special thanks go to Matthias Leiß, who made important contributions to the hedgehog-rabbit entanglement scenario during his time in our group as a bachelor student.
I would also like to thank all my friends inside and outside university who have made the last years a wonderful time to me.
Finally, many thanks to my mother Isolde and Walter for their great support during all my studies.

Contents

Chapter 1

Introduction

Quantum mechanics (QM) is rightly considered our most successful physical theory, explaining everything from subnuclear particles up to solid state properties and beyond, and giving rise to revolutionary new technologies. Even theories such as string theory that intend to supersede state of the art physics and resolve the seemingly last remaining puzzle in physics, the unification of QM with the theory of gravity, are constructed on the principles of QM. At the same time, there has been a debate about its status as a fundamental theory that persists ever since its formulation. What provides the basis for putting it into question over and over again? What distinguishes QM from other, "classical", theories of physical phenomena?

Divided world... In contrast to "classical" theories, which claim to give a direct account of nature, the quantum mechanical formalism comes along with a fundamental discrepancy between the way it describes the world and our perception of it. The quantum mechanical wave functions seem not to admit a naive realistic interpretation, and orthodox QM resolves the apparent contradiction between classically well-defined properties and their quantum superpositions by attributing a privileged role to the measurement process as a means to mediate between these otherwise irreconcilable positions. The prize to pay is, besides the inherent indeterminism expressed by Born's rule, the abandonment of an "objective reality", since according to this philosophy it is the measurement which "creates" the properties, whereas the wave function is degraded to the status of a mere catalogue of our knowledge about the system. Such an epistemic attitude towards the interpretation of QM seems also favorable when considering the in general entangled wave functions of many-particle systems, which do not admit their embedding in ordinary space and render the concept of logically separable physical objects questionable.

...or not? However, the division of the world into two parts, one that is described appropriately by QM, and another consisting of observers and classical apparatuses, must be considered unsatisfactory from the point of view of a "classical" physicist, who seeks a physical theory that gives a uniform and complete account of logically independent objects and their (possibly local) interactions, independent of observers or whether being measured or not. While the "Copenhagen interpretation" and modern quantum information theorists accept this dualism as a fundamental epistemological limit, there have thus been several proposals to resolve the measurement problem and at the same time to regain an undivided description of reality, most by assuming an objective interpretation of QM. Mentioning the most prominent, the Bohmian approach, e.g., considers QM

universally valid, but to be completed by (hidden) definite particle trajectories carrying the desired classical properties [1, 2]. Spontaneous collapse models, on the other hand, consider QM complete, but unrestrictedly valid only in the microscopic regime (where "microscopic" has to be defined appropriately), whereas macroscopically unique properties are guaranteed by introducing nonlinear stochastic modifications to the Schrödinger equation preventing superpositions from reaching the "classical" regime [3, 4]. Probably mostly favored among physicists nowadays, however, are those approaches that consider QM complete and universally valid, the emergence of classicality merely being an issue concerning the correct interpretation of the formalism; decoherence theory and the many-world interpretation are among those [5–9]. But despite of its great successes in explaining the vanishing of quantum mechanical coherences by the interaction with the ubiquitous environment, decoherence theory cannot give a complete account for the definite outcomes in measurements.

Probing the borderline In view of the variety of competing proposals the status of QM must be considered pending: Is the "Heisenberg cut" really as arbitrary as suggested by the operational viewpoint? Can the resolution of the measurement problem, the emergence of classicality really be traced back to an intricate interplay between quantum mechanical degrees of freedom, much in the sense decoherence theory proposes? Or do entanglement and the superposition principle encounter principal barriers at the transition to classicality? Where does this transition from a holistic bunch of quantum particles to a "measurement apparatus" occur, being virtually indispensable for an objective world to be in compliance with our experience? It seems advisable to remain open-minded, in particular the more one advances into presumably classical territory.

1.1 Scope of the thesis

Goal In this thesis I propose scenarios to challenge the classical perspective by delocalizing and entangling the free motion of two material particles over macroscopic scales. Such experiments would probe both pillars of nonclassicality, the superposition principle and entanglement, in a genuine classical system, since persistent material particles can claim their objective existence much more than elusive photons, whose role as an interaction exchange particle rather attributes them to the forces than to matter. Pinpointing the hierarchy with the above discussion in mind, one may say that, while photons effect clicks in detectors, atoms *are* detectors. Moreover, delocalization of the particle motion affects the fundamental question to what extent particles should be describable by trajectories, the basis of Newtonian mechanics. Any serious attempt to account for the emergence of our experienced world should give rise to these trajectories at some stage. Alternative theories, in turn, are expected to reflect their divergence from QM most profoundly in the spatial degrees of freedom. This is challenged even the more, since in the proposed experiment both the single-particle delocalization and the inter-particle separation reach the macroscopic scales of everyday life on the order of centimeters, which are amenable even without auxiliary devices and hence would naively be attributed to the tamed classical world we usually experience. Finally, the nonclassicality is revealed by employing simple position measurements, which admit an immediate classical interpretation completing the classical correspondence.

While some of these aspects have already been probed separately in previous experiments (see also [10–16]), e.g. entanglement at macroscopic separation on the order

of 100 kilometers with photons [17, 18], or motional entanglement of microscopically separated ions in an ion trap [19, 20], or interference of massive fullerenes with delocalizations on the scale of micrometers [21, 22], the combined testing of all of them simultaneously would set a further milestone at the front line between QM and classicality.

Implementation The presented scheme is based on the gradual dissociation of an ultracold Feshbach molecule. It thus relies on the unprecedented expertise that has been experimentally achieved in producing and manipulating even molecular Bose-Einstein condensates, reaching a level of control where quantum effects become amenable [23–34]. Ultimately, the scheme aims at reproducing Bell state correlations in the motional degree of freedom. The violation of a Bell inequality then serves to unambiguously confirm the entanglement and at the same time the delocalization. To this end, the scheme utilizes a sequence of magnetic field pulses in order to delocalize each of the dissociated atoms into two spatially distinct wave packets, where the state of the two counterpropagating atoms entangles the wave packets corresponding to the same dissociation instant. By either generating subsequent wave packets that propagate with the same or with differing velocities, one obtains two complementary ways to reconcile the underlying continuous variable system with operationally dichotomic correlations similar to those supported by the spin-1/2 singlet state. While the former scenario is supplemented by subsequent interferometric processing to mimic a Bell test with correspondence to the spin-based formulation even on the state level, the latter can dispense with the interferometers, recovering the Bell test only on an operational level.

The violation of a Bell inequality implies that QM does not admit an explanation of the correlations without resorting to entanglement, the quantum mechanical way of expressing the impossibility of a description by separate systems. From a more fundamental point of view, and apart from the locality loophole, which lies not in the focus of this proposal, such a Bell violation would extend the refutation of any (possibly effective) local realistic description to the motion of material particles, and even to macroscopic parameter regimes. This refutation would pose an even more severe threat to the plausibility of the objective view point than the established nonlocality in internal or photonic degrees of freedom.

I investigate the possibility of a Bell violation in both mentioned scenarios. Besides specifying frame parameters where the resulting scales are experimentally under control, e.g. the ability to resolve the fringe pattern or to guide the atoms optically, this comprises in particular to determine the constraints on the wave packets due to the detrimental effect of inevitable matter wave dispersion [35, 36]. A confirmative answer in the conceived scenarios thus requires the precise knowledge of the generated Feshbach dissociation states for given magnetic field pulses. To this end, I develop the formalism to obtain the asymptotic dissociation state for arbitrary pulses based on a coupled-channel approach [37]. Both scenarios are then shown to support a Bell violation for appropriate choices of the dissociation pulses [38].

1.2 Structure

The thesis is structured as follows: In **Chapter 2** I recapitulate Bell's derivation of his inequality, which is based on Bohm's spin version of the EPR Gedankenexperiment, with the test of local realism in mind. **Chapters 3 and 4** then introduce two classes of matter

wave states that, on the one hand, are capable to generate Bell state correlations, and, on the other hand, are amenable within the considered Feshbach dissociation scenario. While *dissociation-time entangled* (DTE) states achieve the correspondence to a Bell test by mimicking both the spin singlet state and the subsequent spin measurements with superposed wave packets of equal velocity, the *hedgehog-rabbit entangled* (HRE) states superpose wave packets of different velocities, where two-time position measurements in the overlap regions and their appropriate dichotomization reveal the Bell correlations on an operational level. In both cases the resulting correlations are investigated for not further specified, dispersing wave packets, yielding general conditions to be met by the dissociation states to achieve a Bell violation.

Chapter 5 presents a common experimental frame for both scenarios, based on the partial dissociation of a molecular Bose-Einstein condensate and on subsequent optical guidance, admitting atomic velocities on the order of cm/s and particle separations of up to 10 cm. The coupled-channel description of the Feshbach dissociation dynamics and the derivation of the resulting asymptotic dissociation state for a general time-dependent magnetic field behavior in **Chapter 6** then provides the basis for feasibility studies concerning the DTE and the HRE scenarios.

Chapter 7 applies the general formalism derived in Chapter 6 to describe the generation of a DTE state by appropriate magnetic field pulses. This dissociation state is then used to study a possible Bell violation by building on the preliminary results from Chapter 3. An analogous treatment of the HRE scenario in **Chapter 8** continues the investigation of Chapter 4, now specializing to the corresponding dissociation state. In both cases, experimentally viable pulse parameters predicting robust Bell violations are determined. Besides summarizing the results of the thesis, I conclude in **Chapter 9** by discussing possible extensions and variations of the Feshbach dissociation scheme and the DTE and HRE scenarios.

Chapter 2

Probing nonclassicality

As already mentioned in the Introduction, no satisfactory resolution for the apparent irreconcilability of QM with the classical perspective has been found so far. Instead of trying to give such an explanation at a single stroke, one line of research thus aims at pinpointing the origins of this irreconcilability by testing isolated concepts that are taken for granted from the classical point of view. In the case of the Bell theorem, the classical concept at test is *local realism* [39–41]. (In brief, this means that correlations between separated, non-interacting objects should be explainable by a common past; below, I give a precise definition.) Other nonclassicality tests assume, e.g., *noncontextuality* (independent physical quantities should be able to take independent measured values) [42–44], *macroscopic realism* (properties of macroscopic objects should be independent of whether being measured or not) [45], *Lorentz invariance* (of the hidden variable underpinning) [46] or *crypto-nonlocal realism* (a nonlocal, but no-signaling hidden variable underpinning, such that locally all measurements can be described by classical mixtures of pure states, in reminiscence of particle properties) [47–49]. All these tests share the same philosophy: they derive measurable consequences of the presumed classical concept that are in conflict with the predictions of QM; given that nature confirms QM, one then gains the insight that any theory substituting QM would have to do without this property. This way one can systematically learn about the possibilities and limitations of any conceivable future theory constructed to complete QM.

We apply Bell's theorem in order to establish the nonclassicality in our scenarios. Besides probing locality,[1] one of the most sacrosanct principles in modern physics, in an unprecedented generality, the violation of a Bell inequality can serve to confirm both the entanglement and the delocalization of the considered two-particle states. In this chapter, I recapitulate the derivation of Bell's inequality and its violation in the spin-based experiment originally considered by him [39], and I discuss issues and challenges one faces when one intends to apply it to the motion of material particles.

2.1 Entanglement vs. local realism

Bell's analysis represents the culmination of a development that started with the bare intuition that entanglement may tell us something fundamental about the constitution of nature. It was recognized already shortly after the formulation of QM that the in general nonseparable wave function of a system of several particles does not admit a

[1] Those physicists, who prefer to consider QM a local theory in view of its no-signaling property, would rather refer to probing 'separability'.

naive realistic interpretation in ordinary space, but would require to concede the reality of the higher-dimensional configuration space [50]. This may have been the reason for de Broglie to secede from the guiding wave interpretation initially promoted by him, whereas supporters of the de Broglie-Bohm theory consider it a merit of their theory to render nature's nonlocality explicit [51]. The inevitable nonlocal aspects of QM may also have been the reason for Schrödinger to denote entanglement "the characteristic trait of QM", in the sense that among all the counter-intuitive features of QM mainly entanglement may spoil the hope to regain a "classical", local interpretation of nature [52].

The argument of Einstein, Rosen and Podolsky

In contrast to those who attribute to QM some kind of nonlocality, Einstein, Podolsky and Rosen (EPR) advocate locality and instead employ entanglement in order to attack the complementary principle, answering the question "Can quantum-mechanical description of physical reality be considered complete?" in their famous paper to the negative [53]. They consider the following motionally entangled (improper) two-particle state,

$$|\Psi_{\mathrm{EPR}}\rangle = \int \mathrm{d}x |x\rangle_1 |x\rangle_2 = \int \mathrm{d}p |p\rangle_1 |-p\rangle_2, \tag{2.1}$$

which describes perfect correlations both in position and in momentum, whereas the single-particle properties are completely undetermined. Measuring either position or momentum of one of the particles then also determines the result of the corresponding subsequent measurement of the other particle. EPR argue that, given the two particles have ceased to interact at some point in the past, the second particle must have had this property prior to measurement (the property must have been an "element of reality", as referred to by EPR), because otherwise some "spooky action at a distance" would have to be in charge of communicating the measurement outcomes between the particles to ensure the correlations. Since this holds both for position and momentum, which are conjugate variables and hence cannot take definite values simultaneously according to the complementary principle, EPR conclude that QM is incomplete, in the sense that the theory does not reflect all elements of reality.

Consequently, EPR believed in the possibility of a local realistic underpinning of their Gedankenexperiment, and indeed the EPR state (2.1) can be approximated by Gaussian states, which admit a classical interpretation in the case of "classical" measurements such as position and momentum. In brief, one may say that, based on locality and the belief that correlations must be founded on preexisting "elements of reality", EPR infer the quantum mechanically denied reality of such preexisting local properties from the correlations between the two distant parties. By turning the argument around, it was Bell's merit to demonstrate that such preexisting local properties cannot account for all quantum mechanical correlations, thus rendering the EPR premise of local realism wrong.

2.2 The Bell experiment

How can one probe local realism? Taking the non-existence of properties prior to measurement serious suggests that quantum mechanical correlations are more intimately related to the "free will" decisions which local observables one measures than classically explainable, since classically the presumed preexisting properties are by definition

logically independent of these decisions. As already hinted at in the EPR experiment, a clash between the quantum mechanical prediction and local realism may thus be provoked by comparing measurements of noncommuting observables, whose simultaneous existence is excluded by the complementary principle. Employing an appropriate entangled state may then evoke correlations that cannot be reduced to shared randomness given the measurement events are spacelike separated.

The adequate playground for such an attempt is not given by the EPR Gedankenexperiment though, but by its reformulation in a more transparent spin-based setting [39, 54], see Figure 2.1. Since Bell's investigations are based on this scenario, we will refer to it as *Bell experiment* from now on. Downgrading the motional degrees of freedom to the mere passive role of separating the two particles, we instead take their spins to be in the entangled singlet state,

$$|\Psi^-\rangle = (|\uparrow\rangle_1|\downarrow\rangle_2 - |\downarrow\rangle_1|\uparrow\rangle_2)/\sqrt{2}. \tag{2.2}$$

Let us assume that the particles are remote, they may even be continuously moving apart from each other, such that we can exclude any kind of (local) interaction between them. Spin measurements on both sides (e.g. with Stern-Gerlach magnets) along the directions $\vec{n}_1$ and $\vec{n}_2$, respectively, yield the correlation function

$$\begin{aligned} C^-(\vec{n}_1,\vec{n}_2) &= \langle\Psi^-|\vec{n}_1\cdot\vec{\sigma}_1\otimes\vec{n}_2\cdot\vec{\sigma}_2|\Psi^-\rangle \\ &= -\vec{n}_1\cdot\vec{n}_2, \end{aligned} \tag{2.3}$$

where we have identified $(\vec{\sigma}_i)_x = |\uparrow\rangle_i\langle\downarrow|_i + |\downarrow\rangle_i\langle\uparrow|_i$, $(\vec{\sigma}_i)_y = -i|\uparrow\rangle_i\langle\downarrow|_i + i|\downarrow\rangle_i\langle\uparrow|_i$ and $(\vec{\sigma}_i)_z = |\uparrow\rangle_i\langle\uparrow|_i - |\downarrow\rangle_i\langle\downarrow|_i$, meaning that the basis $|\uparrow\rangle_i$, $|\downarrow\rangle_i$ is aligned along the z-direction. As anticipated by inspection of (2.2) and in analogy with the EPR state, one finds perfect (anti-)correlations for equally aligned measurement directions. Moreover, measurements with arbitrarily oriented axes are easily implemented in this spin setting, in contrast to the EPR experiment, where only single-particle position and momentum measurements are viable. We will see below that combinations of non-trivially twisted orientations are required to refute local realism.

Equivalently to the correlation function, one can consider the joint probability to detect the outcomes $\sigma_1,\sigma_2 \in \{1,-1\}$,

$$\begin{aligned} P^-(\sigma_1,\sigma_2|\vec{n}_1,\vec{n}_2) &= |\langle\vec{n}_1,\sigma_1|\langle\vec{n}_2,\sigma_2|\Psi^-\rangle|^2 \\ &= \frac{1}{4}[1-\sigma_1\sigma_2\cos(\varphi_1-\varphi_2)], \end{aligned} \tag{2.4}$$

where $|\vec{n}_i,\sigma_i\rangle$ denote the eigenfunctions of $\vec{n}_i\cdot\vec{\sigma}_i$. In the second line we have parametrized the measurement directions by $\vec{n}_i = (\sin\theta_i\cos\varphi_i, \sin\theta_i\sin\varphi_i, \cos\theta_i)^{\mathrm{T}}$ and set $\theta_1 = \theta_2 = \pi/2$ for convenience. We will find below that this restriction to measurements in the plane perpendicular to the orientation of the spins ("in plane"-measurements) does not diminish the possibility of a Bell violation. Note that the correlation function and the joint probability are connected via

$$C^-(\vec{n}_1,\vec{n}_2) = \sum_{\sigma_1,\sigma_2=\pm1} \sigma_1\sigma_2 P^-(\sigma_1,\sigma_2|\vec{n}_1,\vec{n}_2). \tag{2.5}$$

Usually, one considers the singlet state to discuss the Bell experiment, since it is isotropic in the sense that its correlations (2.3) are invariant under synchronous rotations of the measurement directions. For the purpose of comparison with later results, it is

however useful to consider the more general Bell state (which is equivalent regarding the potential to violate a Bell inequality)

$$|\Psi_{\text{Bell}}\rangle = (|\uparrow\rangle_1|\uparrow\rangle_2 + e^{i\phi}|\downarrow\rangle_1|\downarrow\rangle_2)/\sqrt{2}, \tag{2.6}$$

yielding the joint probability

$$P_{\text{Bell}}(\sigma_1,\sigma_2|\varphi_1,\varphi_2) = \frac{1}{4}[1+\sigma_1\sigma_2\cos(\varphi_1+\varphi_2-\phi)] \tag{2.7}$$

for "in plane"-measurements, and the corresponding correlation function

$$C_{\text{Bell}}(\varphi_1,\varphi_2) = \cos(\varphi_1+\varphi_2-\phi). \tag{2.8}$$

We will see below that the singlet correlations (2.3) and the Bell state correlations (2.8), respectively, are stronger than classical correlations in the sense that they depend stronger on the control parameters than classically admissible, and hence can serve to refute local realism, the presumed completion of QM by preexisting properties.

2.3 Bell inequalities

While EPR premise locality in order to derive the incompleteness of QM, a rather metaphysical conclusion, Bell, driven by intuition about the nonlocal consequences of QM, put locality itself into question. Turning the EPR argument around by assuming that such hidden variables indeed exist, he could derive a quantitative, testable statement on the possibility of such a complete account as a base for correlations. An essential contribution to this end was turning towards the dichotomic spin setting with its flexibility concerning amenable spin observables. In the following I recapitulate the derivations of Bell and CHSH, respectively [39, 40].

Realism

Let us assume that there exist hidden variables that are responsible for the outcomes σ_1 and σ_2 of the measurements in the Bell experiment. The measurement outcomes σ_1, σ_2 in an individual run can then considered to be determined by the underlying hidden variable $\lambda \in \Lambda$ and the chosen spin observables characterized by the measurement directions $\vec{n}_1$ and $\vec{n}_2$, $\sigma_1(\vec{n}_1,\vec{n}_2,\lambda)$, $\sigma_2(\vec{n}_1,\vec{n}_2,\lambda)$. Note that it is important to distinguish the settings from the hidden variables, since the former share the "free will" of the experimenter which observable to measure, while the latter exists by definition prior to measurement and hence are independent of it. Indeed, one may say that Bell's major accomplishment was the neat separation of the roles and mutual dependences of the hidden variables, the settings (control parameters) and the outcomes. The resulting correlation function emerges from averaging over a multitude of runs with their corresponding hidden variables,

$$C_{\text{HV}}(\vec{n}_1,\vec{n}_2) = \int_\Lambda d\lambda\,\rho(\lambda)\sigma_1(\vec{n}_1,\vec{n}_2,\lambda)\sigma_2(\vec{n}_1,\vec{n}_2,\lambda) \tag{2.9}$$

where the hidden variables follow some unknown probability distribution $\rho(\lambda)$ ($\rho(\lambda) \geq 0$, $\int_\Lambda d\lambda\,\rho(\lambda) = 1$), which is by definition independent of the settings. Note that the "hidden variable" λ may be thought of as being a single variable or several, discrete or continuous, as denoting initial conditions or the physical state of the system as described by any possible future theory; the argument does not require to be specific about this.

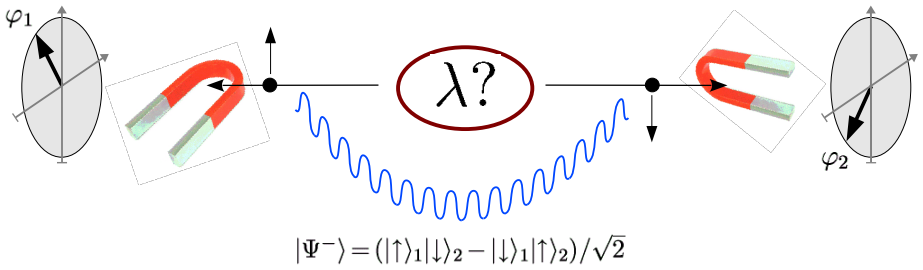

Figure 2.1: Bell experiment based on Bohm's version of the EPR argument: A pair of remote, spin-entangled particles in the singlet state $|\Psi^-\rangle = (|\uparrow\rangle_1|\downarrow\rangle_2 - |\downarrow\rangle_1|\uparrow\rangle_2)/\sqrt{2}$ is exposed to spin measurements (e.g. with Stern-Gerlach magnets) along arbitrary directions $\vec{n}_i = (\sin\theta_i\cos\varphi_i, \sin\theta_i\sin\varphi_i, \cos\theta_i)^{\mathrm{T}}$, yielding the correlation function $C^-(\vec{n}_1,\vec{n}_2) = -\vec{n}_1\cdot\vec{n}_2$. Restricting to measurements in the plane perpendicular to the spin orientation (note that for the sake of clarity I deliberately depict them parallel in the figure), the correlation function reduces to $C^-(\vec{n}_1,\vec{n}_2) = -\cos(\varphi_1-\varphi_2)$, which violates the CHSH inequality maximally for appropriate choices of the control parameters φ_i. As in the EPR experiment, locality is incorporated by deciding about the measured observables (parametrized by the control parameters φ_i) only after the particles have ceased to interact and are remote. One may then assume that the measurement outcomes on one side do not depend on the "free will" settings on the other side. A loophole-free test with that respect would require that the measurement events are spacelike separated, which even excludes the hypothetical (subluminal) communication of the measurement settings based on an underlying hidden variable theory. Excluding such a communication, violation of the CHSH inequality refutes local realism, the presumed "complete" account of the physical state denoted by the hidden variables λ. Since the formulation of the CHSH inequality does not make any assumptions on the underlying physical realization, one may also strive for generating the required dichotomic correlations by employing degrees of freedom other than spin, may they be discrete or continuous. This thesis presents two approaches to come up with Bell correlations based on the motion of the particles.

Locality

While the expression (2.9) merely determines the correlation function by preexisting properties ("realism"), which alone does not have the potential to lead to any usable restrictions as compared to quantum mechanical correlations, we can promote (2.9) to a *local* realistic description by additionally taking into account that the outcomes on each side should not depend on the settings of the other side, $\sigma_1(\vec{n}_1,\lambda)$ and $\sigma_2(\vec{n}_2,\lambda)$, respectively. This assumption, implementing locality, constitutes the heart of Bell's argument, rendering its striking consequences possible. The correlation function, which now reads

$$C_{\mathrm{LHV}}(\vec{n}_1,\vec{n}_2) = \int_\Lambda \mathrm{d}\lambda\rho(\lambda)\sigma_1(\vec{n}_1,\lambda)\sigma_2(\vec{n}_2,\lambda), \tag{2.10}$$

turns out to be sufficiently restrictive to come into conflict with QM. Let me emphasize that, most remarkably, Bell clear-sightedly reduced the locality requirement to a relation between the settings and the outcomes, releasing him from making any assumptions about the hidden variables and their dynamics whatsoever.

As obvious and intuitive as the separability assumption in (2.10) may be, in order to make sure that no local communication between the measurement setting on one side and the outcome on the other side is possible one must demand that the measurement events are spacelike separated (and strictly speaking, even the decisions which observables to measure). But even if this is not provided there are good reasons for advocating the plausibility of (2.10) from the point of view of a classical physicist, who expects to recover the existence of separate systems and the possibility to explain correlations by shared randomness at least with respect to certain not yet probed "classical" parameter regimes and degrees of freedom, without the need to employ any conspirative unknown interaction in charge of communicating the settings, be it local or not. Moreover, assuming the existence of a local communication mechanism to reproduce quantum mechanical correlations exactly within the light cone should result in an abrupt breakdown of the correctness of quantum mechanical predictions at the transition to spacelike separations. In view of this rather peculiar behavior, it appears more reasonable to extend the presumed validity of (2.10) from spacelike separations to timelike ones.

Aside from that, (2.10) can also be interpreted in terms of QM, denoting correlations that emerge from a separable state; in this line of argument, a contradiction with (2.10) then witnesses the entangled nature of the underlying quantum mechanical state.

2.3.1 Bell's inequality

The correlation function (2.10) comprises the presumed local realism, and comparing it with (2.5), one indeed realizes that it appears to leave less freedom on how to come up with correlations than QM. How can we reveal this clash with QM? Above we suspected that the quantum mechanically excluded simultaneous existence of noncommuting observables should play a crucial role; hence Bell's final clue was to consider combinations of correlation functions with differently oriented spin observables. In detail, he considers the difference

$$\begin{aligned} |C_{\mathrm{LHV}}(\vec{a},\vec{b}) - C_{\mathrm{LHV}}(\vec{a},\vec{c})| &= \left| \int_\Lambda \mathrm{d}\lambda\rho(\lambda)[\sigma_1(\vec{a},\lambda)\sigma_2(\vec{b},\lambda) - \sigma_1(\vec{a},\lambda)\sigma_2(\vec{c},\lambda)] \right| \\ &= \left| \int_\Lambda \mathrm{d}\lambda\rho(\lambda)[1-\sigma_2(\vec{b},\lambda)\sigma_2(\vec{c},\lambda)]\sigma_1(\vec{a},\lambda)\sigma_2(\vec{b},\lambda) \right| \\ &\leq \int_\Lambda \mathrm{d}\lambda\rho(\lambda)[1-\sigma_2(\vec{b},\lambda)\sigma_2(\vec{c},\lambda)], \end{aligned} \tag{2.11}$$

where the triangle inequality for integrals was used in the last step. Based on the singlet state (2.2), Bell then assumes perfect anti-correlation for equally aligned measurement directions,

$$\sigma_1(\vec{a},\lambda) = -\sigma_2(\vec{a},\lambda), \tag{2.12}$$

which allows him to replace the last term in (2.11) by the corresponding correlation function, yielding the inequality that now carries his name,

$$|C_{\rm LHV}(\vec{a},\vec{b}) - C_{\rm LHV}(\vec{a},\vec{c})| \leq 1 + C_{\rm LHV}(\vec{b},\vec{c}). \tag{2.13}$$

The Bell theorem states that any hidden variable account of the Bell experiment satisfying the requirements of local realism (2.10) must as well satisfy Bell's inequality (2.13). This provokes two obvious questions: What has QM to say about it; and what nature?

2.3.2 CHSH inequality

In its original form (2.13) is not really suited for an experimental testing, since the assumed perfect anti-correlations (2.12) are unrealistic from an experimental point of view, where one must always take imprecisions into account. This was recognized by Clauser, Horne, Shimony and Holt (CHSH), who generalized Bell's derivation with that respect [40]. Instead of premising the perfect correlations (2.12), they merely assume the existence of measurement directions $\vec{b}$, $\vec{b}'$ such that the experimentally gained correlations achieve

$$C_{\rm exp}(\vec{b}',\vec{b}) = 1 - \delta, \tag{2.14}$$

with $0 \leq \delta \leq 1$ (Bell requires $\delta = 0$ for $\vec{b}' = -\vec{b}$). Dividing the set of hidden variables Λ into two regions Λ_+, Λ_- such that $\Lambda_\pm = \{\lambda | \sigma_1(\vec{b}',\lambda) = \pm\sigma_2(\vec{b},\lambda)\}$ allows them to write

$$\begin{aligned} C_{\rm LHV}(\vec{b}',\vec{b}) &= \int_\Lambda {\rm d}\lambda \rho(\lambda)\sigma_1(\vec{b}',\lambda)\sigma_2(\vec{b},\lambda) = \int_{\Lambda_+} {\rm d}\lambda\rho(\lambda) - \int_{\Lambda_-} {\rm d}\lambda\rho(\lambda) \\ &= 1 - 2\int_{\Lambda_-} {\rm d}\lambda\rho(\lambda) = 1-\delta, \end{aligned} \tag{2.15}$$

which implies $\int_{\Lambda_-} {\rm d}\lambda\rho(\lambda) = \delta/2$. The correlation on the right hand side of (2.11) can thus be rewritten as

$$\begin{aligned} &\int_\Lambda {\rm d}\lambda\rho(\lambda)\sigma_2(\vec{b},\lambda)\sigma_2(\vec{c},\lambda) \\ &\quad = \int_\Lambda {\rm d}\lambda\rho(\lambda)\sigma_1(\vec{b}',\lambda)\sigma_2(\vec{c},\lambda) - 2\int_{\Lambda_-} {\rm d}\lambda\rho(\lambda)\sigma_1(\vec{b}',\lambda)\sigma_2(\vec{c},\lambda) \\ &\quad \geq C_{\rm LHV}(\vec{b}',\vec{c}) - 2\int_{\Lambda_-} {\rm d}\lambda\rho(\lambda)|\sigma_1(\vec{b}',\lambda)\sigma_2(\vec{c},\lambda)| = C_{\rm LHV}(\vec{b}',\vec{c}) - \delta. \end{aligned} \tag{2.16}$$

With this (2.11) yields the CHSH inequality

$$|C_{\rm LHV}(\vec{a},\vec{b}) - C_{\rm LHV}(\vec{a},\vec{c})| \leq 2 - C_{\rm LHV}(\vec{b}',\vec{b}) - C_{\rm LHV}(\vec{b}',\vec{c}). \tag{2.17}$$

Note that we did not require δ to be small; (2.17) can thus be applied to arbitrary quantum states. However, we will find that its violation is only possible for small δ. Below I give a quantitative criterion for its violation in terms of the visibility of the fringe pattern, which is directly connected to δ.

The relation (2.17) gives the original inequality derived by CHSH; its most widely used variant can be conveniently regained in hindsight when considering the quantity

$$\begin{aligned} X &:= \sigma_1(\vec{a},\lambda)\sigma_2(\vec{b},\lambda)+\sigma_1(\vec{a},\lambda)\sigma_2(\vec{b}',\lambda)+\sigma_1(\vec{a}',\lambda)\sigma_2(\vec{b},\lambda)-\sigma_1(\vec{a}',\lambda)\sigma_2(\vec{b}',\lambda) \\ &= \sigma_1(\vec{a},\lambda)\left[\sigma_2(\vec{b},\lambda)+\sigma_2(\vec{b}',\lambda)\right]+\sigma_1(\vec{a}',\lambda)\left[\sigma_2(\vec{b},\lambda)-\sigma_2(\vec{b}',\lambda)\right] \\ &= \pm 2. \end{aligned} \tag{2.18}$$

The triangle inequality $|\int_\Lambda \mathrm{d}\lambda\,\rho(\lambda)X| \leq \int_\Lambda \mathrm{d}\lambda\,\rho(\lambda)|X|$ then yields

$$|C_{\mathrm{LHV}}(\vec{a},\vec{b})+C_{\mathrm{LHV}}(\vec{a},\vec{b}')+C_{\mathrm{LHV}}(\vec{a}',\vec{b})-C_{\mathrm{LHV}}(\vec{a}',\vec{b}')| \leq 2, \tag{2.19}$$

which one usually refers to when talking about the CHSH inequality. In the following I will term (2.19) simply Bell inequality, and a Bell test corresponds to testing whether a physical setup satisfies or violates it.

2.4 Bell violation

Both the singlet correlations (2.3) and the Bell correlations (2.8) violate the Bell inequality (2.19), already when restricting to "in plane"-measurements, $\theta_1=\theta_2=\pi/2$. In the case of the singlet, e.g., the maximal violation is achieved by the choice $\varphi_1=0$, $\varphi_1'=\pi/2$, $\varphi_2=\pi/4$ and $\varphi_2'=-\pi/4$, and for (2.8) correspondingly by $\varphi_1=\phi/2$, $\varphi_1'=\phi/2+\pi/2$, $\varphi_2=\phi/2-\pi/4$ and $\varphi_2'=\phi/2+\pi/4$,

$$\begin{aligned} &|C_{\mathrm{Bell}}(\phi/2,\phi/2-\pi/4)+C_{\mathrm{Bell}}(\phi/2,\phi/2+\pi/4) \\ &+C_{\mathrm{Bell}}(\phi/2+\pi/2,\phi/2+\pi/4)-C_{\mathrm{Bell}}(\phi/2+\pi/2,\phi/2-\pi/4)| = 2\sqrt{2} \geq 2. \end{aligned} \tag{2.20}$$

As anticipated from the complementary principle, the violation is based on comparing measurements of noncommuting observables. Indeed, it is well known that it is not possible to violate a Bell inequality by measuring commuting observables [55]. The required non-trivial twisting to observables "in between" the "canonical" observables σ_x, σ_y, σ_z may indicate why the EPR experiment restricted to mere single-particle position and momentum measurements is insufficient. Remarkably, the violation achieved in (2.20) is not only maximal for the Bell state (2.6), but for any quantum mechanical state, as was shown by Cirel'son [56]. General no-signaling theories, on the other hand, can violate Cirel'son's bound, and intense ongoing research attempts to pinpoint what singles QM out among them, what causes nature not to exploit the full extent of correlations as admitted by relativity [57–63].

The maximal violation in (2.20) implies the perfect correlations (2.8), but, as recognized by CHSH, this corresponds to an idealized situation, whereas an experimentally realistic consideration should take a non-vanishing diminishing δ of the correlations into account, see (2.14). In terms of the joint probability (2.7) this results in a reduced visibility v of the fringe pattern,

$$P(\sigma_1,\sigma_2|\varphi_1,\varphi_2)=\frac{1}{4}[1+\sigma_1\sigma_2 v\cos(\varphi_1+\varphi_2-\phi)], \tag{2.21}$$

where $0 \leq v \leq 1$. A violation in (2.20) is then ensured given the visibility exceeds the threshold $v > 1/\sqrt{2}$, since the corresponding correlation function is reduced by a factor v as compared to (2.8).

2.5 Application to motion

Bell derived his inequality with the spin-based Bell experiment in mind; however, an analysis of the derivation reveals that it is completely operational with respect to both the outcomes and the settings, in the sense that it makes no explicit use of the assumed underlying spin system. One may thus just as well strive for realizations based on other degrees of freedom. In fact, the first experiments testing local realism were performed with photons, where the entanglement resided in their polarization [41, 64, 65].

It is not even necessary to require that the employed degrees of freedom are dichotomic (meaning that they are two-valued variables), since Bell's derivation only assumes the range of the outcomes to be bounded by $[-1,1]$; however, from (2.14) and (2.21) we know that only the extremal outcomes contribute to sufficiently distinct correlations as demanded by a Bell violation, which renders it favorable to consider dichotomic outcomes. In the case of continuous variables this amounts to giving a prescription of how to end up with such binary outcomes.

For instance, one can define pseudo-spin or displaced parity operators on the quadrature amplitudes of a single-mode light field with the annihilation operator a [66]. On the one hand, one finds a spin algebra by defining

$$\begin{aligned} s_z &= \sum_{n=0}^{\infty} [|2n+1\rangle\langle 2n+1| - |2n\rangle\langle 2n|] \\ s_- &= \sum_{n=0}^{\infty} |2n\rangle\langle 2n+1| = (s_+)^\dagger, \end{aligned} \tag{2.22}$$

where $|n\rangle$ are the eigenstates of the number operator $N = a^\dagger a$. On the other hand, the annihilation operator defines a complementary pair of hermitian quadrature operators via $a = (X_1 + iX_2)/2$. This way one can relate measured field quadratures to pseudo-spin values. Note that such a complementary pair of quadrature operators can be interpreted in terms of the usual position and momentum operators. Arbitrarily oriented pseudo-spin measurements in general require measurements of linear combinations of the quadrature operators X_i, which can be realized easily within a homodyne detection scheme. One finds that two-mode squeezed vacuum states (the "regularized" EPR states) violate the CHSH inequality when measuring non-trivially twisted combinations of quadrature operators [66–68], as it was already the case in the spin experiment.

The ability to measure these mode observables renders a Bell violation possible, even though the EPR states have a positive phase space representation. This is possible since the Wigner representations of the pseudo-spin projectors have values outside of the interval $[0,1]$ and consequently cannot be interpreted as conditional probabilities [69,70]. However, only position measurements are easily realizable for free material particles, the case we are interested in. A direct implementation of the pseudo-spin approach with EPR states thus seems not to be practical in this situation. One may argue that the free time evolution of the (Heisenberg picture) position operators (partly) recovers the ability to perform arbitrary position-momentum measurements, and harmonic trapping of the particles could even restore the full correspondence to the quadrature measurements; however, while it is not obvious whether one can establish the full correspondence in the former case, the experimental implementation of the latter seems to be exceedingly hard. In both cases, it seems unlikely that the necessary measurement accuracy can be achieved with present day technology.

An alternative route thus proposes to employ nonclassical quantum states, instead, in the sense that they have a partly negative phase space representation. In particular,

one may hope that macroscopically delocalized phase space distributions support robust quantum interference effects that restore the possibility to violate a Bell inequality, even when one is restricted to position measurements with limited accuracy. In this thesis I present two scenarios that employ such highly nonclassical quantum states of material particles. The first considers motional states that admit an effectively dichotomic interpretation themselves, the second assigns dichotomic values to the measurement outcomes in a way adapted to the nonlocal interference.

Let me note that there exist other entanglement tests that are applicable to EPR-like Gaussian states. For instance, only entangled states can violate Heisenberg-like uncertainty relations of the kind $[x_{\mathrm{cm}}, p_{\mathrm{rel}}] \geq \hbar/2$, where x_{cm} and p_{rel} may denote the center of mass position and the relative momentum of a diatomic system, respectively. Such tests are used in existing proposals to verify EPR correlations in the dissociation states of ultracold molecules [71–73]. However, a Bell violation constitutes a considerably more convincing demonstration of nonclassicality, since it is conclusive independent of whether QM is valid or not. And as mentioned above, the states we consider would realize macroscopic delocalizations of the atomic wave functions, another desirable nonclassical feature that Gaussian states lack and which allows these states to uncover their nonclassicality by robust interference effects. One goal of this thesis thus is to convince the reader that such highly nonclassical states are realizable by dissociating ultracold Feshbach molecules. A detailed description of the conceived dissociation scheme will be given in the Chapters 5 and 6.

Finally, it should be mentioned that there exist extensions of Bell's theorem to arbitrary (finite) numbers of parties, settings and outcomes [74, 75]; however, they neither appear to be better suited to the case of continuous variables nor do they come along with an essential conceptual gain as compared to the above dichotomic Bell test. Existing Bell inequalities that are explicitly designed for unbounded continuous variables, on the other hand, are only shown to be useful in the case of field quadrature measurements and more than 10 parties [76,77]. In our diatomic dissociation scheme a dichotomic Bell test thus seems to be most appropriate.

Chapter 3

Dissociation-time entanglement

We seek motional states that can serve as a basis for realizing Bell correlations and thus make it possible to perform a Bell test. In the last chapter I argued that EPR-like Gaussian states are not useful in the case of free material particles, where only position measurements are easily realized. I proposed to employ nonclassical quantum states, instead, which could disburden the Bell test on the measurement side. Here I introduce the first of the two macroscopically nonclassical states investigated in this thesis; both have the potential to achieve robust Bell violations based on single-particle interferometry and simple position measurements.

The scenario considered in this chapter implements a Bell test by providing direct correspondence to the spin-based Bell test both on the state level and on the measurement level. The state preparation, which entangles and superposes macroscopically distinct wave packets, is inspired by photonic time-bin entanglement and is implemented naturally by the double-pulse dissociation of a diatomic molecule. Here I sketch the basic idea of the state generation only briefly, to an extent required for the general discussion in this chapter. Its detailed description within the Feshbach dissociation scheme will be given in Chapter 7.

After introducing switched single-particle interferometry and subsequent position measurements as a means to mimic spin measurements, I elaborate to which degree the Bell state correlations can be reproduced when taking into account the effect of detrimental, yet unavoidable dispersion [36]. Although dispersion generically decreases the visibility of the resulting fringe pattern, careful choices of the parameters are shown to exhibit the potential to violate a Bell inequality.

3.1 Motional binning by gradual molecular dissociation

The structure of the class of states considered in this chapter is understood best in terms of the general generation procedure. Starting from a trapped diatomic molecule, two equal dissociation pulses separated by a time period τ create the superposition of two subsequent dissociations (“early” and “late”). Later, when we specialize to the dissociation of Feshbach molecules, magnetic field pulses will serve to lift the molecular bound state above its dissociation threshold; however, the specific implementation is irrelevant for the general discussion here. The dissociations must be coherent in the sense that no information is leaked to the environment about the time of dissociation. Then an observer cannot tell whether the dissociation took place at the early or at the late instant, while both atoms must have started their journey at the same time. In this sense, the

generated two-particle state may be called dissociation-time entangled (DTE). Due to momentum conservation the dissociated atoms propagate in opposite directions along a one-dimensional wave guide, with each atom delocalized into a pair of consecutive wave packets, corresponding to the early and the late dissociation instant, see Fig. 3.1(a). A macroscopic time period τ then results in a superposition of macroscopically distinct wave packets, allowing us to address them individually. As we will see in Chapter 5, the proposed experimental setup based on ultracold Feshbach molecules indeed renders scales on the order of centimeters realistic [35].

We take the dissociation pulses to be equal in this chapter. The early and the late wave packets then propagate at the same speed, which keeps them sufficiently long spatially distinct and thus permits to address them individually in subsequent interferometric processing. As we will see below, this way the wave packets describe effectively dichotomic properties. In Chapter 4 we will extend the scheme to unequal dissociation pulses, resulting in early and late wave packets of different velocities. There we loose the dichotomic analogue on the state level, whereas a different measurement prescription sustains the Bell state correlations.

Note that the DTE state differs fundamentally from the Gaussian states describing EPR-type correlations. As opposed to Gaussian states, it displays a strongly structured, partly negative Wigner function. This is reflected most profoundly in the possible interference between the macroscopically distinct early and late wave packets. Below, we will use their interference to formulate a Bell test in terms of simple position measurements.

3.1.1 Time-bin entanglement

The idea to encode qubits in spatially distinct wave packets was originally introduced for photons [78], building upon the concept of energy-time entanglement [79]. A pulsed laser in combination with an interferometric delay loop placed in front of a parametric down-conversion crystal permits to generate twin-photons which are entangled in their creation time. The resulting state, which has been termed time-bin entangled (TBE), takes the form

$$|\Psi_{\mathrm{tbe}}\rangle = \frac{1}{\sqrt{2}}(|\mathrm{E}\rangle_1|\mathrm{E}\rangle_2 + \mathrm{e}^{\mathrm{i}\phi_\tau}|\mathrm{L}\rangle_1|\mathrm{L}\rangle_2), \tag{3.1}$$

where $|\mathrm{E}\rangle_i$ and $|\mathrm{L}\rangle_i$ denote spatially distinct traveling photonic modes corresponding to the early and the late creation time [78]. Since photons do not disperse in vacuum they differ merely by their spatial displacement, their shape may be taken to be identical. The TBE state (3.1) can be visualized in analogy to the DTE state depicted in Fig. 3.1(b), although we will see that they differ in important aspects.

Since the relevant entanglement resides in the relation between the early and late modes, we can interpret the creation times as a dichotomic property constituting an effectively two-dimensional state space (per photon). By identifying, say, "early" with "spin up" and "late" with "spin down", the state $|\Psi_{\mathrm{tbe}}\rangle$ evidently corresponds to the Bell state (2.6), $|\Psi_{\mathrm{Bell}}\rangle = \frac{1}{\sqrt{2}}(|\uparrow\rangle_1|\uparrow\rangle_2 + \mathrm{e}^{\mathrm{i}\phi}|\downarrow\rangle_1|\downarrow\rangle_2)$. Provided that the early and the late wave packet components are spatially sufficiently distinct, a switched, asymmetric Mach–Zehnder interferometer makes it possible to perform the analogue of a general spin measurement, see Fig. 3.2 and the discussion below [78]. Such a photonic TBE state has indeed been used successfully for establishing nonlocal correlations over fiber distances of more than 50 km [78,80,81] in a similar setup as in Fig. 3.2, though without switching.

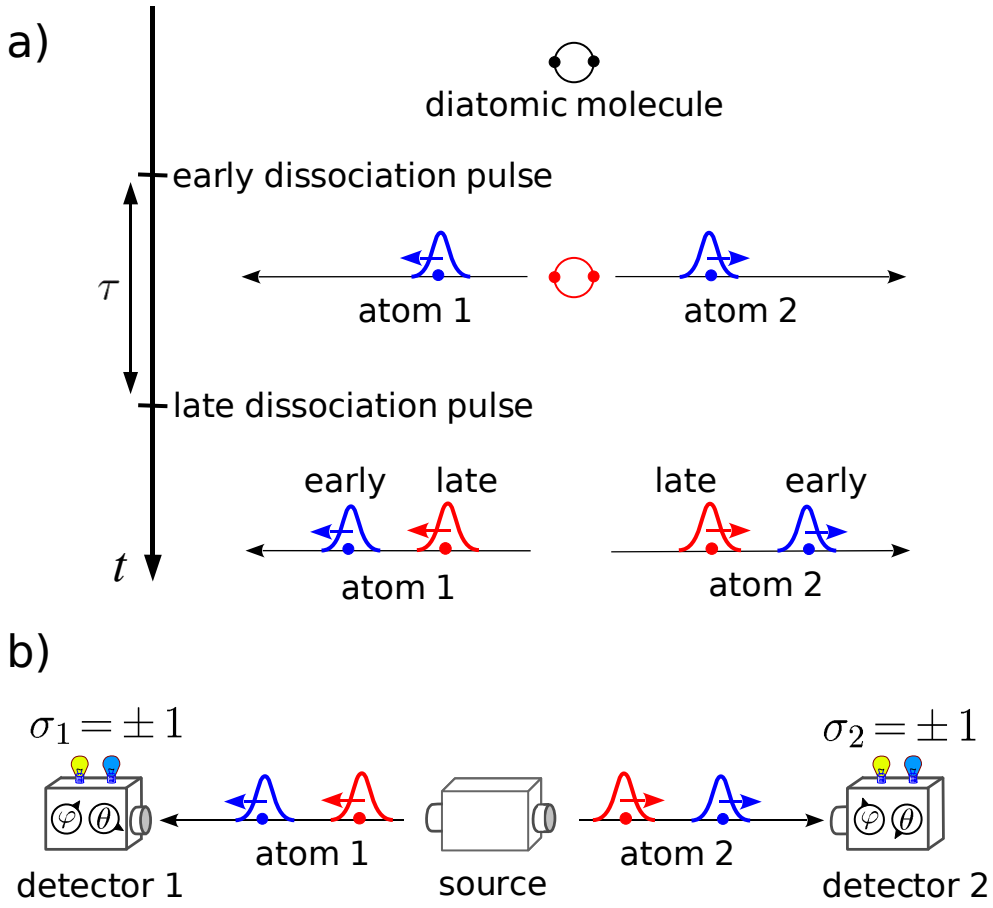

Figure 3.1: (a) Generation of a dissociation-time entangled pair of atoms. A diatomic molecule is exposed to two equal, subsequent dissociation pulses separated by a time period τ. Anticipating the Feshbach dissociation scheme, one may think of magnetic field pulses that lift the molecular bound state above its dissociation threshold. The early pulse is chosen such that the atoms remain bound with a given probability; the second pulse dissociates the remaining molecular state component. Each atom then has an early and a late wave packet component such that the resulting state of two counterpropagating particles is entangled in the dissociation times. (b) If the wave packet components of the dissociation-time entangled atoms are spatially sufficiently separated, they encode effectively dichotomic properties which are amenable to a Bell test in terms of switched single-particle interferometry and position measurements, see Fig. 3.2.

From now on we will interpret the TBE state (3.1) as a matter wave state, which follows from identifying $|\mathrm{E}\rangle_i$ and $|\mathrm{L}\rangle_i$ with the early and the late wave packet components of two freely moving atoms. Like for the photons, the early and late wave packets are taken to propagate at the same velocity. And as in the photonic case, we assume that the early and the late wave packets of each particle are identical in shape.[1] It is important to note that the dispersive spreading experienced by matter waves (in contrast to photonic modes, which keep their shape during their travel through free space) does not spoil this identity of the wave packets, since they are all affected in the same way. As we will see, this renders the TBE Bell test described below resistant with respect to detrimental dispersion effects and thus retains the perfect photonic correspondence with the spin-based Bell experiment.

3.1.2 Dissociation-time entanglement

It should be emphasized that the TBE state (3.1) is not the natural outcome in a molecular two-time dissociation process. In fact, it seems practically impossible to produce the TBE state with material particles. As outlined above, the scheme conceived in this thesis relies on the controlled dissociation of a weakly bound Feshbach molecule with the help of a Feshbach resonance. An appropriately chosen magnetic field pulse causes the atomic components to dissociate and propagate in opposite directions. A sequence of two magnetic field pulses then generates the desired superposition of two dissociation times. It is clear that only the relative motion of the two atoms is (directly) affected by the dissociation, therefore the center of mass motion (of an untrapped molecule) remains separable from the relative motion, unlike in the TBE product of single-particle states. And even more incisively, we should take into account that the early wave packets experience dispersive spreading in the time period τ between the two dissociation pulses. This effects a dispersion-induced distortion between the early and the late wave packets. A generic DTE state thus takes the form

$$|\Psi_{\mathrm{dte}}\rangle = \frac{1}{\sqrt{2}}\left(\widehat{\mathrm{U}}_{\tau}^{(0)}|\Psi_0\rangle + \mathrm{e}^{\mathrm{i}\phi_\tau}|\Psi_0\rangle\right), \tag{3.2}$$

with the single-dissociation state

$$|\Psi_0\rangle = \frac{1}{\sqrt{2}}|\psi_0^{\mathrm{cm}}\rangle\left(|\psi_0^{\mathrm{rel}}\rangle + \widehat{\mathrm{P}}|\psi_0^{\mathrm{rel}}\rangle\right). \tag{3.3}$$

Here, $\widehat{\mathrm{P}}$ is the parity operator, and we assume that the early and the late dissociation occur with equal probability. In the following, we take the state $|\Psi_{\mathrm{dte}}\rangle$, and accordingly $|\Psi_{\mathrm{tbe}}\rangle$, to describe a one-dimensional, longitudinal motion, implying that the transverse components of the motion are confined to the ground state of an atom guide. The state $|\psi_0^{\mathrm{rel}}\rangle$ denotes the wave packet of the relative motion after a single dissociation pulse propagating into positive direction, while $|\psi_0^{\mathrm{cm}}\rangle$ describes the wave packet of the center of mass motion residing at the former position of the molecule.

Note how the DTE state (3.2) differs from the above TBE state (3.1) as it is not composed of two single-particle product states, but superposes the relative coordinate of the two atoms (at a single dissociation time). Due to the symmetry of the dissociation process, each particle has an amplitude to propagate in each direction. Moreover, the

[1] Remarkably, a successful Bell test does not require that the early wave packets of the two particles are identical in shape (and similar for the late ones), since they do not have to interfere in the protocol considered below.

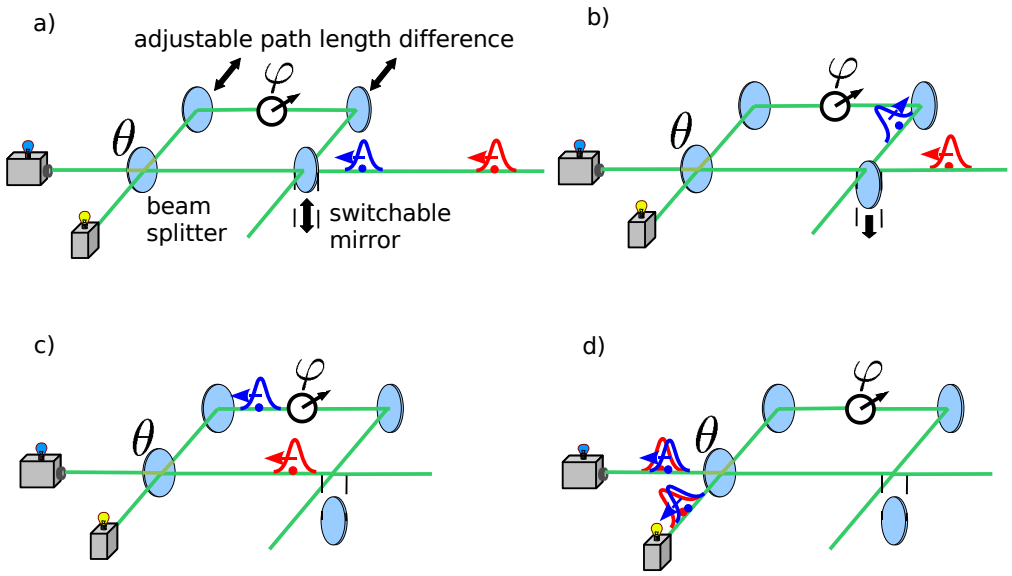

Figure 3.2: State analysis with an asymmetric Mach–Zehnder interferometer. (a) When the early wave packet component arrives, the switchable mirror is in place and deflects it into the long arm. (b) The switchable mirror is removed before the arrival of the late wave packet. (c) The early wave packet acquires an optional phase shift φ in the long arm, whereas the late wave packet propagates through the short arm. (d) The path difference is chosen such that it cancels the distance between the early and the late wave packet components, which then interfere in the output ports of the interferometers. Detecting the atom in one of the output ports, at a given phase φ and splitting ratio θ, amounts to a measurement analogous to a spin-1/2 detection in an arbitrary direction.

DTE state incorporates the unavoidable dispersion-induced distortion between the early and the late state components, described by the free time-evolution operator $\widehat{\mathrm{U}}_{\tau}^{(0)}$.

3.2 Interferometric spin measurement analogue

A crucial property of both the TBE state (3.1) and the DTE state (3.2) is that they are amenable to a Bell test based on interferometric state transformation and subsequent position measurements. Before tackling the motional Bell experiment with the experimentally appropriate DTE state (3.2), it is instructive to first describe the interferometric setup and the effect of dispersion with the TBE state (3.1). This will render the correspondence of the interferometric transformation to a spin measurement most transparent.

3.2.1 Interferometric protocol

The setup is based on switched, asymmetric Mach–Zehnder interferometers, as shown in Fig. 3.2. Their action can be described as follows: The early wave packet components are deflected by the switches into the long arms of the interferometers, where they acquire optional phase shifts φ_i before the beam splitters distribute them onto their output ports according to their splitting ratios, as parameterized by the angles θ_i. The switches are timed such that they let pass the late wave packet components, which then propagate straight to the beam splitters where they are also distributed according to the splitting

ratios θ_i. When the path length difference between the interferometer arms is chosen such that it exactly cancels the distance between the early and the late wave packets, the latter will overlap in the output ports of each interferometer and interfere. Assuming ideal phase shifters and beam splitters, the early and late state components $|\mathrm{E}\rangle_i$ and $|\mathrm{L}\rangle_i$ of the TBE state (3.1) transform according to

$$\begin{aligned} |\mathrm{E}\rangle_i &\rightarrow \mathrm{e}^{\mathrm{i}\varphi_i}\cos\theta_i|+\rangle_i + \mathrm{e}^{\mathrm{i}\varphi_i}\sin\theta_i|-\rangle_i \\ |\mathrm{L}\rangle_i &\rightarrow \sin\theta_i|+\rangle_i - \cos\theta_i|-\rangle_i, \end{aligned} \tag{3.4}$$

where $|+\rangle_i$ and $|-\rangle_i$ denote wave packet components in the two output ports of interferometer $i = 1,2$ at a stage of the time evolution when the particles must have passed the interferometers. This mapping requires that the components $|\mathrm{E}\rangle_i$ and $|\mathrm{L}\rangle_i$ of the initial state are identical wave packets up to their spatial displacement, that is $|\mathrm{L}\rangle_i = \mathrm{e}^{\mathrm{i}\widehat{\mathrm{p}}_i s_i/\hbar}|\mathrm{E}\rangle_i$, with s_i denoting their separation. Remember that this property was assumed for the TBE state (3.1). Moreover, the states $|\mathrm{E}\rangle_i$ and $|\mathrm{L}\rangle_i$ must be spatially sufficiently distinct, such that they can be distinguished by the switches, even when taking dispersion-induced wave packet spreading into account. Note that it is not important to be specific about the particular instant, at which we consider the wave packet components $|+\rangle_i$ and $|-\rangle_i$, since we will only be interested in the overall detection probabilities per port, which unitary time evolution guarantees to remain unaffected by any subsequent time evolution. In this sense, the present treatment already incorporates dispersion, since we do not have to assume that the wave packets $|+\rangle_i$ and $|-\rangle_i$ are equal in shape to the wave packets $|\mathrm{E}\rangle_i$ and $|\mathrm{L}\rangle_i$.

3.2.2 TBE correlations

After passing the interferometers, the TBE state can be written in accordance with (3.4) as

$$|\Psi'_{\mathrm{tbe}}\rangle = \frac{1}{2^{2/3}} \sum_{\sigma_1,\sigma_2=\pm} \left[\mathrm{e}^{\mathrm{i}(\varphi_1+\varphi_2)} + \sigma_1\sigma_2\mathrm{e}^{\mathrm{i}\phi_\tau}\right] |\sigma_1\rangle_1|\sigma_2\rangle_2. \tag{3.5}$$

For clarity, I have taken 50:50 beam splitters ($\theta_1 = \theta_2 = \pi/4$). As argued in Chapter 2, this restriction to effective "in-plane" spin measurements does not come with any loss of significance, since it still admits the maximal violation of a Bell inequality. The joint probability for detecting the particles in a particular output port combination thus reads ($\sigma_{1,2} = \pm 1$)

$$\begin{aligned} \mathrm{P}_{\mathrm{tbe}}(\sigma_1,\sigma_2|\varphi_1,\varphi_2) &= |\langle\sigma_1|_1\langle\sigma_2|_2|\Psi'_{\mathrm{tbe}}\rangle|^2 \\ &= \frac{1}{4}[1+\sigma_1\sigma_2\cos(\varphi_1+\varphi_2-\phi_\tau)], \end{aligned} \tag{3.6}$$

which yields the corresponding correlation function

$$\begin{aligned} C_{\mathrm{tbe}}(\varphi_1,\varphi_2) &= \sum_{\sigma_1\sigma_2=\pm} \sigma_1\sigma_2\mathrm{P}_{\mathrm{tbe}}(\sigma_1,\sigma_2|\varphi_1,\varphi_2) \\ &= \cos(\varphi_1+\varphi_2-\phi). \end{aligned} \tag{3.7}$$

As desired, the detection probability (3.6) and the TBE correlation function (3.7) take the same form as in the spin-based Bell experiment, compare with (2.7) and (2.8), and are thus equally capable to violate the CHSH-inequality [40] $|C(\varphi_1,\varphi_2)+C(\varphi_1,\varphi'_2)+C(\varphi'_1,\varphi_2)-C(\varphi'_1,\varphi'_2)| \leqslant 2$ maximally, e.g., for the choices $\varphi_1 = \phi/2$, $\varphi_2 = \phi/2-\pi/4$, $\varphi'_1 = \phi/2+\pi/2$, and $\varphi'_2 = \phi/2+\pi/4$ (see Chapter 2). This demonstrates the perfect

correspondence of the TBE Bell experiment with the spin-based Bell test and indicates that the interferometric transformation indeed mimics a spin measurement on the TBE state. In this interferometric scheme, the output ports provide dichotomic outcomes, whereas the phase shifts φ_i and the beam splitting ratios θ_i take the role of the Bell control parameters.

The perfect agreement of the TBE correlation function (3.7) with the spin-based correlation function (2.8) reveals that the nonlocal correlations are not affected by the dispersive spreading of the wave packets. This follows from the assumption that the early and the late wave packets are identical up to a spatial displacement. We will see below that this is not valid for the more realistic DTE state (3.2), where the dispersion-induced distortion between the early and the late wave packets is taken into account.

From an experimental point of view, the natural quantity to be measured is the arrival time of the particles at the detectors. The two-time probability density $\mathrm{pr}(\sigma_1,\sigma_2;t_1,t_2)$ for detecting the particles at times t_1, t_2 in a particular output port combination constitutes in general a complicated fringe pattern as a function of the φ_i, θ_i and t_i. It depends not only on the shape of the wave packets and their dispersion-induced modifications due to the overall propagation time, but also on the particular implementation of the measurement [82–85]. The integrated probability $\mathrm{P}_{\sigma_1,\sigma_2} = \int \mathrm{d}t_1\mathrm{d}t_2\mathrm{pr}(\sigma_1,\sigma_2;t_1,t_2)$, however, only measures the overall likelihood for finding the particles in a particular output port combination. It is thus unaffected by the particular shape of the wave packets and any dispersion-induced modification thereof, since unitary time evolution implies the conservation of probability in the output ports. Strictly speaking, this is valid only if measurement-induced reflections of the wave packets at the detectors can be excluded [82–86]. But since our setup does not require prominent temporal or spatial resolution of the measurement, we can safely neglect this effect. For this reason, we may identify the integrated probability $\mathrm{P}_{\sigma_1,\sigma_2}$ with (3.6).

3.2.3 Spin measurement analogue

I conclude this section by presenting a more formal argument why the above state transformation (3.4) acting on a general (single-particle) "time-bin" superposition state $|\psi\rangle = a|\mathrm{E}\rangle + b|\mathrm{L}\rangle$, $|a|^2+|b|^2=1$, followed by the detection in one of the output ports can formally be understood as the analogue of a "spin" measurement with respect to the measurement axis $\vec{n} = (\sin(2\theta)\cos\varphi, \sin(2\theta)\sin\varphi, \cos(2\theta))$. To this end, we define the analogues of Pauli matrices $\hat{\sigma}_x = |\mathrm{E}\rangle\langle\mathrm{L}| + |\mathrm{L}\rangle\langle\mathrm{E}|$, $\hat{\sigma}_y = -i|\mathrm{E}\rangle\langle\mathrm{L}| + i|\mathrm{L}\rangle\langle\mathrm{E}|$, $\hat{\sigma}_z = |\mathrm{E}\rangle\langle\mathrm{E}| - |\mathrm{L}\rangle\langle\mathrm{L}|$, and $\widehat{\vec{\sigma}} = (\hat{\sigma}_x, \hat{\sigma}_y, \hat{\sigma}_z)$. The interferometric transformation (3.4) and the subsequent detection of the transformed state $|\psi'\rangle$ in the output ports can then be equivalently understood as a measurement of the observable $\vec{n}\cdot\widehat{\vec{\sigma}}$ with respect to the untransformed state $|\psi\rangle$. This is most easily seen by noting that the transformation (3.4) acts like an expansion of the incoming time-bin state into the eigenstates $|\vec{n},+\rangle, |\vec{n},-\rangle$ of $\vec{n}\cdot\widehat{\vec{\sigma}}$. With this, the joint detection probability may equally well be written as

$$\mathrm{P}_{\mathrm{tbe}}(\sigma_1,\sigma_2|\vec{n}_1,\vec{n}_2) = |\langle\vec{n}_1,\sigma_1|_1\langle\vec{n}_2,\sigma_2|_2|\Psi_{\mathrm{tbe}}\rangle|^2, \tag{3.8}$$

and the correlation function is given by

$$C_{\mathrm{tbe}}(\vec{n}_1,\vec{n}_2) = \langle\Psi_{\mathrm{tbe}}|\left[\vec{n}_1\cdot\widehat{\vec{\sigma}}_1\right]\otimes\left[\vec{n}_2\cdot\widehat{\vec{\sigma}}_2\right]|\Psi_{\mathrm{tbe}}\rangle. \tag{3.9}$$

We thus find the prescriptions to determine these quantities to be formally equivalent to the spin case, rendering the reduction of the binned motion to a dichotomic property manifest.

3.3 Bell test with dissociation-time entanglement

Up to now, we established a motional Bell test for the TBE state (3.1). However, from an experimental point of view, the DTE state (3.2) is much more relevant, since its structure is naturally produced by the dissociation of a diatomic molecule. In the following I will describe the effect of the above interferometric transformation on the DTE state (3.2).

The DTE wave function differs from the TBE state in two important points: (i) it does not separate into single-particle states at a particular dissociation time and (ii) the dispersive time evolution between the early and the late dissociation process implies different shapes for the early and late wave packet components. Furthermore, we now specify the phase shifters to be implemented by varying the arm lengths of the interferometers, which effects an additional mismatch between the early and the late state components. All these modifications require a more sophisticated theoretical description of the setup. It turns out that time-dependent scattering theory provides the appropriate framework.

3.3.1 Scattering description

Scattering theory applies when the system dynamics under consideration permits to relate asymptotic *in*-states to asymptotic *out*-states [87]. Then, given one is only interested in the relation between these asymptotic states, the exact time evolution connecting the *in* and the *out* states can be split up into an "instantaneous" transformation describing the accumulated effect of the interaction potential and a subsequent free time evolution $\widehat{\mathrm{U}}_t^{(0)}$. In our case,

$$|\Psi'_{\mathrm{dte}}\rangle := \widehat{\mathrm{U}}_t|\Psi_{\mathrm{dte}}\rangle = \widehat{\mathrm{U}}_t^{(0)}\widehat{\mathrm{S}}|\Psi_{\mathrm{dte}}\rangle, \tag{3.10}$$

where $|\Psi'_{\mathrm{dte}}\rangle$ denotes the DTE state at a given stage of evolution when the passage through the interferometers is completed, and the scattering operator $\widehat{\mathrm{S}}$ describes the "raw" action of the interferometers.

In our case, another subtlety comes into play, since we have to distinguish the effect of the interferometers depending on whether the switch is in place ("on"), enforcing deflection into the longer arm, as for the early state component, or absent ("off"), admitting undeflected passage, as for the late state component:

$$|\Psi'_{\mathrm{dte}}\rangle = \widehat{\mathrm{U}}_t^{(0)}\left(\widehat{\mathrm{S}}^{(\mathrm{on})}\widehat{\mathrm{U}}_\tau^{(0)}|\Psi_0\rangle + \mathrm{e}^{\mathrm{i}\phi_\tau}\widehat{\mathrm{S}}^{(\mathrm{off})}|\Psi_0\rangle\right). \tag{3.11}$$

Here we presuppose that dispersion-induced spreading does not spoil the spatial distinctness of the early and the late wave packets. In order to specify the structure of the scattering matrices $\widehat{\mathrm{S}}^{(\mathrm{on})}$ and $\widehat{\mathrm{S}}^{(\mathrm{off})}$, it is convenient to rewrite the DTE state (3.2) as

$$|\Psi_{\mathrm{dte}}\rangle = \frac{1}{\sqrt{2}}\left(|\Psi_{\mathrm{dte}}^{(+)}\rangle + |\Psi_{\mathrm{dte}}^{(-)}\rangle\right) \tag{3.12}$$

with

$$|\Psi_{\mathrm{dte}}^{(+)}\rangle = \frac{1}{\sqrt{2}}\left(\widehat{\mathrm{U}}_\tau^{(0)}|\Psi_0^{(+)}\rangle + \mathrm{e}^{\mathrm{i}\phi_\tau}|\Psi_0^{(+)}\rangle\right), \tag{3.13}$$

where $|\Psi_0^{(+)}\rangle = |\psi_0^{\mathrm{cm}}\rangle|\psi_0^{\mathrm{rel}}\rangle$ and $|\Psi_{\mathrm{dte}}^{(-)}\rangle = \widehat{\mathrm{P}}|\Psi_{\mathrm{dte}}^{(+)}\rangle$. Now $|\Psi_{\mathrm{dte}}^{(+)}\rangle$ describes a two-particle state with particle 1 exclusively propagating into positive direction (and particle 2 into the negative one). This allows one to assign each particle to a definite interferometer, e.g., interferometer 1 to particle 1 (and interferometer 2 to particle 2). The same applies

to $|\Psi^{(-)}_{\rm dte}\rangle$, only with the particles exchanged. Focusing on $|\Psi^{(+)}_{\rm dte}\rangle$, the projection of the scattered state $|\Psi^{(+)'}_{\rm dte}\rangle$ onto a particular output-port combination σ_1, σ_2 reads

$$\begin{aligned}\left(\hat{\Pi}_{\sigma_1}\otimes\hat{\Pi}_{\sigma_2}\right)|\Psi^{(+)'}_{\rm dte}\rangle &= \frac{\widehat{\rm U}^{(0)}_t}{\sqrt{2}}\Big\{\widehat{\rm U}^{(0)}_\tau\left[\widehat{\rm S}^{(\rm on)}_{\sigma_1}\otimes\widehat{\rm S}^{(\rm on)}_{\sigma_2}\right]|\Psi^{(+)}_0\rangle \\ &\quad +{\rm e}^{{\rm i}\phi_\tau}\left[\widehat{\rm S}^{(\rm off)}_{\sigma_1}\otimes\widehat{\rm S}^{(\rm off)}_{\sigma_2}\right]|\Psi^{(+)}_0\rangle\Big\}. \end{aligned} \tag{3.14}$$

Here, $\hat{\Pi}_{\sigma_i}$ is the projection operator onto the region behind the output port labeled by $\sigma_i=(\pm)_i$ of the ith interferometer. The scattering matrix components $\widehat{\rm S}^{(\rm on/off)}_{\sigma_i} = \hat{\Pi}_{\sigma_i}\widehat{\rm S}^{(\rm on/off)}_i$ describe the mapping from an *in*-state to the *out*-state component of a particular beam splitter output port. For example, $\widehat{\rm S}^{(\rm on)}_{\sigma_1=+1}|{\rm in}\rangle$ yields the *out*-state component in the output port labeled by $\sigma_1=+1$ with the switch in place ("on"). For the early wave packets, the switch is in place, causing deflection into the long arm. The offset from the optimum path length difference is reflected in a translation of the early wave packets with respect to the late ones. The late wave packets, on the other hand, pass straight through the short arm before they are distributed into the output ports according to the splitting ratio of the beam splitter. For the scattering matrix components $\widehat{\rm S}^{(\rm on)}_{\sigma_i}$ and $\widehat{\rm S}^{(\rm off)}_{\sigma_i}$, one thus obtains

$$\begin{aligned}\widehat{\rm S}^{(\rm on)}_{\sigma_i=+1} &= {\rm e}^{{\rm i}\hat{p}_i\ell_i/\hbar}\cos\theta_i, \qquad \widehat{\rm S}^{(\rm off)}_{\sigma_i=+1} = \sin\theta_i, \\ \widehat{\rm S}^{(\rm on)}_{\sigma_i=-1} &= {\rm e}^{{\rm i}\hat{p}_i\ell_i/\hbar}\sin\theta_i, \qquad \widehat{\rm S}^{(\rm off)}_{\sigma_i=-1} = -\cos\theta_i, \end{aligned} \tag{3.15}$$

where the translation operators $\exp({\rm i}\hat{p}_i\ell_i/\hbar)$ implement the additional displacements ℓ_i of the early state component (switch "on") with respect to the late ones.

3.3.2 DTE correlations

Like for the TBE state, the joint probability for detecting the particles in a particular output-port combination σ_1, σ_2 is obtained from the projection ${\rm P}^{(+)}_{\rm dte}(\sigma_1,\sigma_2|\ell_1,\ell_2) = |\left(\hat{\Pi}_{\sigma_1}\otimes\hat{\Pi}_{\sigma_2}\right)|\Psi^{(+)'}_{\rm dte}\rangle|^2$. Hence, with (3.14) and (3.15), we get

$$\begin{aligned}{\rm P}^{(+)}_{\rm dte}(\sigma_1,\sigma_2|\ell_1,\ell_2) &= \frac{1}{4}\Big[1+\sigma_1\sigma_2{\rm Re}\Big\{{\rm e}^{-{\rm i}\phi_\tau}\langle\Psi^{(+)}_0|{\rm e}^{{\rm i}\hat{p}_1\ell_1/\hbar}{\rm e}^{-{\rm i}\hat{p}_1^2\tau/(2m\hbar)} \\ &\quad \otimes{\rm e}^{{\rm i}\hat{p}_2\ell_2/\hbar}{\rm e}^{-{\rm i}\hat{p}_2^2\tau/(2m\hbar)}|\Psi^{(+)}_0\rangle\Big\}\Big], \end{aligned} \tag{3.16}$$

where we have for simplicity taken the beam splitters to be symmetric ($\theta_i=\pi/4$) and the particles to be of equal mass m. Evaluating the matrix element in momentum representation, with the abbreviations $\vec{p}=(p_1,p_2)^{\rm T}$ and $\vec{\ell}=(\ell_1,\ell_2)^{\rm T}$, yields

$$\begin{aligned}{\rm P}^{(+)}_{\rm dte}(\sigma_1,\sigma_2|\ell_1,\ell_2) &= \frac{1}{4}\Big[1+\sigma_1\sigma_2{\rm Re}\Big\{{\rm e}^{-{\rm i}\phi_\tau}\int_{-\infty}^{\infty}{\rm d}p_1\int_{-\infty}^{\infty}{\rm d}p_2{\rm e}^{{\rm i}\vec{p}\cdot\vec{\ell}/\hbar} \\ &\quad \times{\rm e}^{-{\rm i}\vec{p}^2\tau/(2m\hbar)}|\langle p_1,p_2|\Psi^{(+)}_0\rangle|^2\Big\}\Big]. \end{aligned} \tag{3.17}$$

The intermediate result (3.17) already reveals some important features of the setup: Firstly, the overall free time evolution $\widehat{\rm U}^{(0)}_t$ in (3.14) drops out for the detection probability, as it was the case for the TBE state. Hence, only the dispersion-induced distortion

between the early and late wave packets, which is due to the period τ between the two dissociation processes, causes potential harm to the fringe pattern of the detection probability as a function of the arm length variations. Next, only the two-particle momentum distribution $|\langle p_1,p_2|\Psi_0^{(+)}\rangle|^2$ of the single dissociation pulse component $|\Psi_0^{(+)}\rangle$ enters the detection probability $\mathrm{P}_{\mathrm{dte}}^{(+)}(\sigma_1,\sigma_2|\ell_1,\ell_2)$. As a consequence, $\mathrm{P}_{\mathrm{dte}}^{(+)}(\sigma_1,\sigma_2|\ell_1,\ell_2)$ is invariant under momentum phase transformations $\langle p_1,p_2|\Psi_0\rangle \to \exp[\mathrm{i}\xi(p_1,p_2)]\langle p_1,p_2|\Psi_0\rangle$, which includes spatial translations. This means that the signal is unaffected by shot-to-shot shifts of the source position with respect to the interferometers (as long as the interferometric procedure is still feasible).

The fact that the correlation signal depends merely on the two-particle momentum distribution also shows that it is straightforward to generalize the detection probability to nonpure and nonseparable states, $|\Psi_0^{(+)}\rangle\langle\Psi_0^{(+)}| \to \rho_0^{(+)}$, and correspondingly $|\langle p_1,p_2|\Psi_0^{(+)}\rangle|^2 \to \mathrm{pr}(p_1,p_2) := \langle p_1,p_2|\rho_0^{(+)}|p_1,p_2\rangle$. In particular, the separability of the center of mass and the relative motion, as it is assumed for the single-dissociation state (3.3), was not used to derive (3.17). In fact, we will see in Chapter 6 that the Feshbach dissociation state only approximately separates into center of mass and relative motion if an experimentally realistic setup is considered.

So far, I have restricted my investigation to the DTE state $|\Psi_{\mathrm{dte}}^{(+)}\rangle$ with each particle propagating into a given direction. It is clear that I could have followed the same reasoning for the DTE state $|\Psi_{\mathrm{dte}}^{(-)}\rangle$, only with the labels for the particles exchanged, such that the corresponding joint detection probability $\mathrm{P}_{\mathrm{dte}}^{(-)}(\sigma_1,\sigma_2|\ell_1,\ell_2)$ equals $\mathrm{P}_{\mathrm{dte}}^{(+)}(\sigma_1,\sigma_2|\ell_1,\ell_2)$. Finally, since our setup is not sensitive to interference between $|\Psi_{\mathrm{dte}}^{(+)}\rangle$ and $|\Psi_{\mathrm{dte}}^{(-)}\rangle$, the detection probability for the symmetric DTE state $|\Psi_{\mathrm{dte}}\rangle = \frac{1}{\sqrt{2}}\big(|\Psi_{\mathrm{dte}}^{(+)}\rangle + |\Psi_{\mathrm{dte}}^{(-)}\rangle\big)$ follows from

$$\begin{aligned}\mathrm{P}_{\mathrm{dte}}(\sigma_1,\sigma_2|\ell_1,\ell_2) &= \frac{1}{2}\Big(\mathrm{P}_{\mathrm{dte}}^{(+)}(\sigma_1,\sigma_2|\ell_1,\ell_2)+\mathrm{P}_{\mathrm{dte}}^{(-)}(\sigma_1,\sigma_2|\ell_1,\ell_2)\Big)\\ &= \mathrm{P}_{\mathrm{dte}}^{(+)}(\sigma_1,\sigma_2|\ell_1,\ell_2). \qquad (3.18)\end{aligned}$$

Hence, the results obtained for the directed DTE state $|\Psi_{\mathrm{dte}}^{(+)}\rangle$ apply just as well to the experimentally realized DTE state $|\Psi_{\mathrm{dte}}\rangle$.

3.3.3 Gaussian evaluation

In order to be able to relate the joint detection probability (3.17) to the spin-based joint probability (2.7) and to get a qualitative and quantitative understanding of the resulting fringe pattern, we evaluate Eq. (3.17) in closed form for the case that the early and the late wave packet components are each described by Gaussian center of mass and relative states. This is reasonable, since even for non-Gaussian wave packet components with a more complicated momentum distribution, an appropriate Gaussian fit should allow us to derive at least a lower bound to the quality of the fringe pattern. The evaluation of (3.17) for an actual Feshbach dissociation state will be done in Chapter 7.

We consider a Gaussian momentum distribution,

$$\mathrm{pr}(p_1,p_2) = \frac{1}{2\pi\sigma_{p,\mathrm{cm}}\sigma_{p,\mathrm{rel}}}\exp\left(-\frac{(p_1+p_2)^2}{2\sigma_{p,\mathrm{cm}}^2}-\frac{(p_1-p_2-mv_{\mathrm{rel}})^2}{8\sigma_{p,\mathrm{rel}}^2}\right), \qquad (3.19)$$

where $\sigma_{p,\mathrm{rel}}$ and $\sigma_{p,\mathrm{cm}}$ denote the variances of the relative and the center-of-mass mo-

mentum, respectively. This yields

$$\begin{aligned} \mathrm{P}^{(+)}_{\mathrm{dte}}(\sigma_1,\sigma_2|\ell_1,\ell_2) = \frac{1}{4}\Bigg\{ 1 + \sigma_1\sigma_2 \left(1+\frac{\tau^2}{T_{\mathrm{cm}}^2}\right)^{-1/4} \left(1+\frac{\tau^2}{T_{\mathrm{rel}}^2}\right)^{-1/4} \\ \times \exp\left[-\frac{T_{\mathrm{rel}}}{T_{\mathrm{rel}}^2+\tau^2}\frac{(\ell_1-\ell_2-\tau v_{\mathrm{rel}})^2}{2v_{\mathrm{rel}}\lambda\!\!\!^{-}_{\mathrm{rel}}} - \frac{T_{\mathrm{cm}}}{T_{\mathrm{cm}}^2+\tau^2}\frac{(\ell_1+\ell_2)^2}{2v_{\mathrm{rel}}\lambda\!\!\!^{-}_{\mathrm{rel}}} \right] \\ \times \cos\left[\frac{\ell_1-\ell_2}{\lambda\!\!\!^{-}_{\mathrm{rel}}} + \frac{\tau}{T_{\mathrm{rel}}^2+\tau^2}\frac{(\ell_1-\ell_2-\tau v_{\mathrm{rel}})^2}{2v_{\mathrm{rel}}\lambda\!\!\!^{-}_{\mathrm{rel}}} + \frac{\tau}{T_{\mathrm{cm}}^2+\tau^2}\frac{(\ell_1+\ell_2)^2}{2v_{\mathrm{rel}}\lambda\!\!\!^{-}_{\mathrm{rel}}} - \frac{\varphi_0}{2} \right] \Bigg\}, \end{aligned} \tag{3.20}$$

with $\varphi_0 = \tau v_{\mathrm{rel}}/\lambda\!\!\!^{-}_{\mathrm{rel}} + \arctan(\tau/T_{\mathrm{cm}}) + \arctan(\tau/T_{\mathrm{rel}}) + 2\phi_\tau$. The variances $\sigma_{p,\mathrm{rel}}$ and $\sigma_{p,\mathrm{cm}}$ determine characteristic dispersion times, $T_{\mathrm{cm}} = 2m\hbar/\sigma^2_{p,\mathrm{cm}}$ and $T_{\mathrm{rel}} = m\hbar/2\sigma^2_{p,\mathrm{rel}}$. The latter indicate the time scale of transition to a dispersion-dominated spatial extension of the wave packets. The expectation value of the relative momentum $p_{0,\mathrm{rel}} = mv_{\mathrm{rel}}/2$ defines the reduced wave length $\lambda\!\!\!^{-}_{\mathrm{rel}} = \hbar/p_{0,\mathrm{rel}}$, which sets the scale for the nonlocal interference fringes. This can be traced back to the fact that we implement the phase shift by displacing the early and late wave packets with respect to each other, whose phase variation, in turn, is set by their de Broglie wave length.

3.3.4 The possibility of a Bell violation

The DTE joint detection probability (3.20) clearly inherits from the TBE Bell test the aspired structural correspondence to the Bell state correlation function (2.7). This implies that one can observe nonlocal interference effects based on DTE states: By varying either ℓ_1 or ℓ_2 the probability to detect the particle pair in a particular output port combination exhibits a periodic variation, while there are of course no single-particle interference effects when one ignores the measurement outcomes of one of the particles.

However, the dispersion-induced distortion between the early and the late wave packet components leaves its marks in those terms in (3.20) which depend on the characteristic dispersion times T_{cm} and T_{rel}. In particular, it is responsible for the overall suppression of the fringe pattern as described by the Lorentzian reduction factors in the first line. Further, it causes a quadratic compression of the fringe pattern, as can be deduced from the quadratic terms in the argument of the cosine. The additional Gaussian suppression in the second line, on the other hand, is due to the unavoidable envelope mismatch that follows from the variation of the arm lengths. One expects no interference if there is no overlap in the beam splitter output ports, which results in the uncorrelated probability distribution of 0.25 per output port combination. The envelope width of this Gaussian thus reflects approximately the size of the initial wave packets, with minor modifications due to the dispersion-induced distortion between them.

In Chapter 2 we found for the case of the imperfect Bell correlations (2.21) that the fringe visibility must exceed the threshold value $1/\sqrt{2}$ in order to achieve a Bell violation. This should last over at least a few fringes when varying either arm length by ℓ_i. An analysis of the joint detection probability (3.20) shows that a sufficient fringe pattern can be expected provided the following two conditions are met:

$$\lambda\!\!\!^{-}_{\mathrm{rel}}/(\tau v_{\mathrm{rel}}) \ll 1, \tag{3.21}$$

$$(1+\tau^2/T_{\mathrm{cm}}^2)(1+\tau^2/T_{\mathrm{rel}}^2) < 4. \tag{3.22}$$

While (3.21) guarantees a sufficiently wide envelope and negligible quadratic compression of the fringe pattern, (3.22) controls the Lorentzian reduction factor to comply with

the visibility threshold. In particular, the latter implies that τ must not greatly exceed the dispersion times T_{cm} and T_{rel}.

One can reformulate (3.22) in terms of conditions on the momentum distributions of the center of mass and the relative motion,

$$\left(\frac{\sigma_{p,\mathrm{cm}}}{p_{0,\mathrm{rel}}}\right)^2 \lesssim 2\frac{m\hbar}{\tau p_{0,\mathrm{rel}}^2} \quad \text{and} \quad \left(\frac{\sigma_{p,\mathrm{rel}}}{p_{0,\mathrm{rel}}}\right)^2 \lesssim \frac{1}{2}\frac{m\hbar}{\tau p_{0,\mathrm{rel}}^2}. \tag{3.23}$$

The proposal conceived in this thesis considers lithium atoms with relative velocities on the order of $v_{\mathrm{rel}} = 1\mathrm{cm/s}$ and time separations of $\tau = 1\,\mathrm{s}$. For these parameters one finds $m\hbar/\tau p_{0,\mathrm{rel}}^2 \approx 5\times 10^{-4}$, which implies that the momentum distributions of both the center of mass and the relative motion must be sharply peaked. The resulting reduced wave length $\lambda\!\!\!^{-}_{\mathrm{rel}} \approx 2\,\mu\mathrm{m}$, on the other hand, easily meets the condition (3.21).

3.3.5 Summary

The DTE scenario uses the two-time dissociation of a molecule in order to split the wave function of the atoms into consecutive propagating wave packets. In combination with interferometric spin measurement analogues based on single-particle matter wave optics and simple position measurements, this admits the desired one-to-one correspondence to the spin-based Bell experiment. The interferometric phase shift and the beam splitting ratio then take the role of the control parameters in this motional Bell test. The resulting nonlocal correlations would manifest both the coherence between the macroscopically distinct early and late wave packet components and their entanglement.

The violation of a Bell inequality is affected by dispersion, though, and it therefore requires sharply peaked momentum distributions. In Chapter 7 I will demonstrate that Feshbach dissociation states can indeed meet the conditions (3.21) and (3.22) [35], and hence pave the way for demonstrating nonclassicality in the motion of material particles. The proposal involves time separations between the two dissociation pulses on the order of seconds, which would result in a spatial separation between the early and late wave packets on the order of centimeters, rendering the DTE state truly macroscopic.

It is remarkable that the DTE scenario does not require interferometric stability between the two interferometers, which makes it experimentally easy to put them at large distances. Moreover, the restriction to the coherence properties between the early and late wave packets as a whole means that only integral measurements behind the ports are needed, requiring neither prominent spatial nor temporal resolution. This renders the nonclassical correlations largely independent of the shape of the wave packets and of the particular implementation of the position measurement. Finally, let me note that the photonic experiments performed to date have been done without switch using instead a post-selection procedure [78]. This has been shown to allow for a local hidden variable model [88, 89], a drawback that is avoided if the switching can be easily implemented, as is the case with slow material particles.

Chapter 4

Hedgehog-rabbit entanglement

In the dissociation-time entanglement (DTE) scenario the approach to end up with Bell state correlations consisted of finding a motional one-to-one correspondence to the spin-based Bell test, both on the state level and on the measurement level. This could be achieved by spatial binning in a two-time dissociation process and by a subsequent interferometric transformation mimicking a spin measurement. The phase shift and the beam splitting ratio in the interferometers took the role of the Bell control parameters, the output ports provided dichotomic measurement outcomes.

In this chapter, I present a motionally entangled state, which follows from a generation protocol almost identical to that of the DTE state. While this allows us to embed it into the same dissociation scenario, it differs completely in its potential to reveal its nonclassical correlations. Instead of applying a sequence of two identical dissociation pulses, let us now choose the late dissociation pulse to be stronger, hence supplying the late wave packets with a larger (mean) kinetic energy. We can then dispense with the interferometers in order to have the early and late wave packets overlap, since we just have to wait for the fast late wave packets to catch up with the slow early ones. Position measurements in the overlap regions on both sides and their suitable dichotomization then reveal correlations similar to the Bell state correlations. Here the freely selectable measurement times take the role of the control parameters. The violation of a Bell inequality requires the formal post-selection of the measurement results in this setting. However in principle the full sample of atom pairs is detected and hence available. In contrast to the DTE setting, the "hedgehog-rabbit" state considered in this chapter does not admit a photonic analogue and thus represents a genuine entangled matter wave state.

4.1 Bichromatic entanglement from unbalanced two-time dissociation

Like with the DTE state presented in the previous chapter, I sketch the basic idea of the generation procedure only briefly, since a detailed description within the Feshbach dissociation scenario will be given in Chapter 8. In fact, the generation protocol for the state considered in this chapter is almost identical to that of the DTE state. We start again from a diatomic molecule and apply a sequence of two dissociation pulses separated by a time period τ ("early" and "late"), only this time the pulses are not equal, but the late pulse is slightly stronger than the early pulse. This way they generate a superposition of wave packets with different velocities, see Figure 4.1(a). More precisely, the wave packets that emerged at the late dissociation pulse are the faster ones, allowing them to

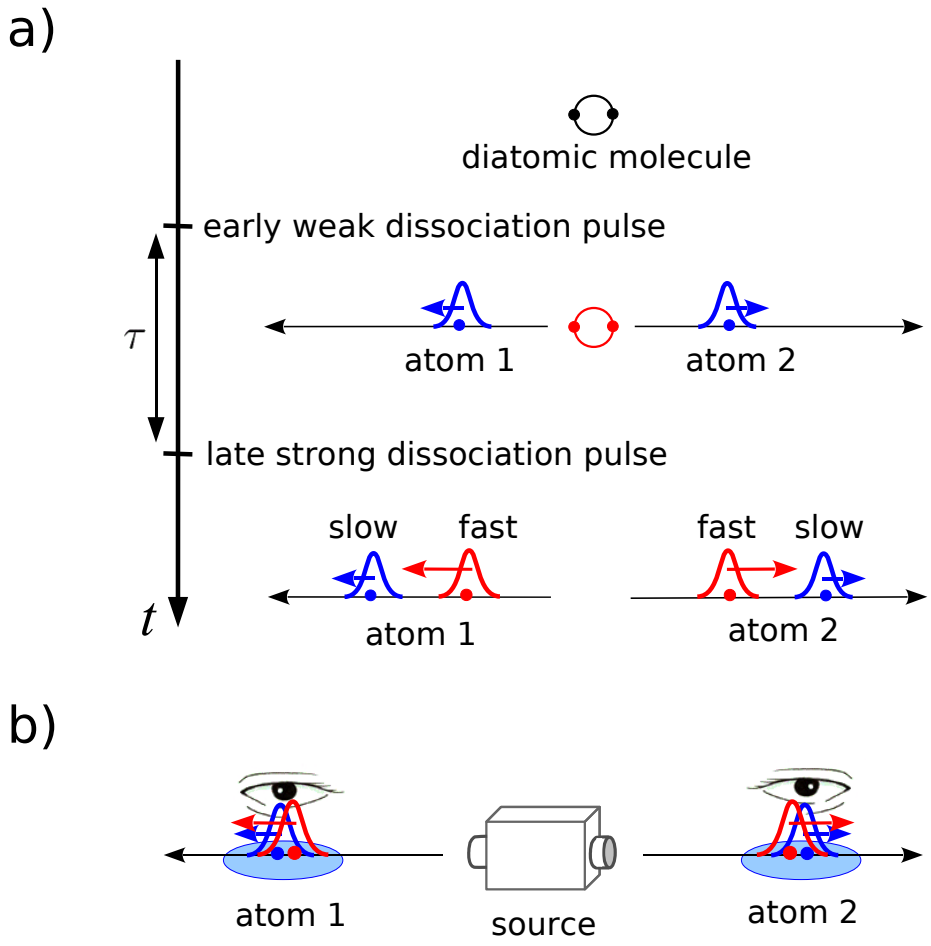

Figure 4.1: (a) Generation of a hedgehog-rabbit entangled pair of atoms. A diatomic molecule is exposed to a sequence of two unbalanced dissociation pulses separated by a time period τ. The late dissociation pulse is stronger and hence endows the corresponding wave packets with a higher kinetic energy. The resulting two-particle state constitutes the superposition of the two dissociation outcomes, with each atom described by an early slow and a late fast wave packet. (b) The time separation τ and the different (mean) velocities v_{s} and v_{f} of the slow and the fast wave packets, respectively, determine their meeting point x_{m} and their meeting time t_{m}, where they come to overlap and interfere. Although the reduced single-particle states do not show an interference pattern, position measurements in the overlap region on both sides then reveal nonlocal correlations that can be subjected to suitable dichotomization and post-selection procedures, yielding Bell state correlations.

catch up with the preceding slower wave packets. Metaphorically, one might thus call the slow wave packets "hedgehogs" and the fast ones "rabbits", and the state correspondingly hedgehog-rabbit entangled (HRE). The generic structure of a HRE state takes the form

$$|\Psi_{\rm hre}\rangle = \frac{1}{\sqrt{2}}\left(\widehat{\rm U}_0^{(1)}(\tau)\otimes\widehat{\rm U}_0^{(2)}(\tau)|{\rm S}\rangle + {\rm e}^{{\rm i}\phi}|{\rm F}\rangle\right), \tag{4.1}$$

with the free single-particle time evolution operator[1] $\widehat{\rm U}_0^{(i)}(t) = \exp(-{\rm i}t\hat{p}_i^2/2m\hbar)$. $|{\rm F}\rangle$ and $|{\rm S}\rangle$ denote the early and the late two-particle dissociation state components, respectively.

Gaussian HRE state

The dissociation states emerging from our Feshbach scenario will turn out to be rather involved, suggesting to find as general a treatment of the situation as possible. For the sake of clarity, however, it is helpful to evaluate the main steps in addition in terms of a Gaussian HRE state. To this end, we take the initial early and late state components to separate into single-particle states, $|{\rm S}\rangle = |{\rm s}\rangle_1|{\rm s}\rangle_2$ and $|{\rm F}\rangle = |{\rm f}\rangle_1|{\rm f}\rangle_2$, where

$$\begin{aligned}\langle x_1|{\rm s}\rangle_1 &= \frac{1}{(2\pi)^{1/4}\sqrt{\sigma}}\exp\left(-\frac{x_1^2}{4\sigma^2}+{\rm i}\frac{p_{\rm s}x_1}{\hbar}\right),\\ \langle x_2|{\rm s}\rangle_2 &= \frac{1}{(2\pi)^{1/4}\sqrt{\sigma}}\exp\left(-\frac{x_2^2}{4\sigma^2}-{\rm i}\frac{p_{\rm s}x_2}{\hbar}\right),\end{aligned} \tag{4.2}$$

and similar for the fast wave packets, with $p_{\rm s}$ replaced by $p_{\rm f}$. The single-particle position uncertainty σ is taken to be the same for all wave packets. According to this state, Particle 1 propagates (exclusively) into positive and Particle 2 (exclusively) into negative direction, the early wave packets with velocity $v_{\rm s} = p_{\rm s}/m$ and the late ones with $v_{\rm s} = p_{\rm s}/m$.

4.2 Temporal correlations with position measurements

The HRE state comes with the benefit not to require interferometers in order to have the early and the late wave packets interfere, since they naturally come to overlap when the late fast wave packets catch up with the early slow ones. The time separation τ between the two dissociation pulses and the particle velocities $v_{\rm s}$ and $v_{\rm f}$ of the slow and the fast state components schedule the meeting point $x_{\rm m}$ and the meeting time $t_{\rm m}$ of the wave packets on each side (note that $v_{\rm s}$ and $v_{\rm f}$ denote single-particle velocities, not relative velocities) according to

$$x_{\rm m} = \pm\frac{v_{\rm f}\tau}{v_{\rm f}/v_{\rm s}-1} \quad \text{and} \quad t_{\rm m} = \frac{\tau}{v_{\rm f}/v_{\rm s}-1}, \tag{4.3}$$

where the plus (minus) sign is assigned to Particle 1 (2). We expect that the HRE state shows nonclassical correlations in the vicinity of this overlap region, since there the early and the late wave packets are not distinguishable and may therefore interfere.

We thus perform position measurements in the vicinity of the meeting points on each side. The measurement times are the control parameters in this scenario and are chosen to lie in the time interval when the wave packets overlap. Note that position operators

[1] In this chapter we slightly change the notation of the free time evolution operator as compared to Chapter 3. The notation in this chapter is more convenient for the situation when different evolution times for the two particles have to be taken into account. The notation in Chapter 3 was adopted from [35].

do not commute at different times (when considered in the Heisenberg picture), as it is required to achieve correlations that are stronger than classically allowed [90]. Position measurements are comparatively easy to implement for material particles, in the case of atoms, e.g., by laser illumination [91]. Moreover, we only have to probe the extent of the overlap region, since the early and late wave packets are assumed to be sufficiently localized.

Joint detection probability

In the end we want to determine the joint probability to detect particle 1 at position x_1 when measuring at time t_1 and particle 2 at position x_2 when measuring at time t_2,

$$\mathrm{P}(x_1,x_2|t_1,t_2) = \left|\langle x_1,x_2|\widehat{\mathrm{U}}_0^{(1)}(t_1)\otimes\widehat{\mathrm{U}}_0^{(2)}(t_2)|\Psi_{\mathrm{hre}}\rangle\right|^2. \tag{4.4}$$

Elaborating (4.4) for the HRE state (4.1), one gets

$$\begin{aligned}\mathrm{P}(x_1,x_2|t_1,t_2) = {}& \frac{1}{2}\left|\langle x_1,x_2|\widehat{\mathrm{U}}_0^{(1)}(t_1+\tau)\otimes\widehat{\mathrm{U}}_0^{(2)}(t_2+\tau)|\mathrm{S}\rangle\right|^2 \\ &+\frac{1}{2}\left|\langle x_1,x_2|\widehat{\mathrm{U}}_0^{(1)}(t_1)\otimes\widehat{\mathrm{U}}_0^{(2)}(t_2)|\mathrm{F}\rangle\right|^2 \\ &+\mathrm{Re}\Big[\mathrm{e}^{-\mathrm{i}\phi}\langle x_1,x_2|\widehat{\mathrm{U}}_0^{(1)}(t_1+\tau)\otimes\widehat{\mathrm{U}}_0^{(2)}(t_2+\tau)|\mathrm{S}\rangle\langle\mathrm{F}|\widehat{\mathrm{U}}_0^{(1)\dagger}(t_1)\otimes\widehat{\mathrm{U}}_0^{(2)\dagger}(t_2)|x_1,x_2\rangle\Big].\end{aligned} \tag{4.5}$$

4.2.1 Dispersion-dominated limit

We now make use of the fact that the wave packets experience considerable dispersive spreading before meeting at the meeting point x_m at the meeting time t_m[2]. This implies that the shape of the wave packets is determined by their momentum distributions, independently of their initial shapes. In this dispersion-dominated limit, $t \gg m\sigma_x^2/\hbar$, the time evolution of an arbitrary (single-particle) wave packet with initial position uncertainty σ_x can hence be written as

$$\langle x|\psi(t)\rangle \simeq \sqrt{\frac{m}{\mathrm{i}t}}\exp\left(\mathrm{i}\frac{m(x^2-\bar{x}^2)}{2\hbar t}\right)\tilde{\psi}\left(\frac{m(x-\bar{x})}{t}\right), \tag{4.6}$$

where $\bar{x} = \langle\psi(t)|\hat{x}|\psi(t)\rangle|_{t=0}$ denotes the mean initial position and $\tilde{\psi}(p) = \langle p|\psi(0)\rangle$ the momentum representation of the initial state. A derivation of (4.6) in terms of the free propagator is given in Appendix A.1, and the generalization of (4.6) to the case of two particles is straightforward. Concerning the HRE state, we require that the meeting time t_m fulfills

$$t_\mathrm{m} \gg m\sigma_{x,\mathrm{s}}^2/\hbar \quad \text{and} \quad t_\mathrm{m} \gg m\sigma_{x,\mathrm{f}}^2/\hbar, \tag{4.7}$$

[2] In principle, this might also hold for the DTE scenario. However there we found that the overall time evolution does not affect the correlation function, but only the dispersive distortion due to the time interval τ between the early and the late dissociation pulse, which we had to require, on the contrary, to be in the regime of negligible dispersion. Hence the asymptotic approximation (4.6) was of no use there.

where $\sigma_{x,\mathrm{s}}$ and $\sigma_{x,\mathrm{f}}$ characterize the position uncertainty of the slow and fast single particle states, respectively[3]. Applying (4.6) to (4.5) then yields

$$\begin{aligned}\mathrm{P}(x_1,x_2|t_1,t_2) &= \frac{1}{2}\frac{m^2}{(t_1+\tau)(t_2+\tau)}|\tilde{\Psi}_\mathrm{S}\left(\frac{mx_1}{t_1+\tau},\frac{mx_2}{t_2+\tau}\right)|^2+\frac{1}{2}\frac{m^2}{t_1t_2}|\tilde{\Psi}_\mathrm{F}\left(\frac{mx_1}{t_1},\frac{mx_2}{t_2}\right)|^2\\ &+\frac{m^2}{\sqrt{t_1(t_1+\tau)t_2(t_2+\tau)}}\tilde{\Psi}_\mathrm{S}\left(\frac{mx_1}{t_1+\tau},\frac{mx_2}{t_2+\tau}\right)\tilde{\Psi}_\mathrm{F}\left(\frac{mx_1}{t_1},\frac{mx_2}{t_2}\right)\\ &\times\cos\left[\frac{m}{2\hbar}\left(\frac{1}{t_1+\tau}-\frac{1}{t_1}\right)x_1^2+\frac{m}{2\hbar}\left(\frac{1}{t_2+\tau}-\frac{1}{t_2}\right)x_2^2-\phi\right],\end{aligned}\tag{4.8}$$

where we assumed that the Fourier transforms $\tilde{\Psi}_\mathrm{S}(p_1,p_2)$ and $\tilde{\Psi}_\mathrm{F}(p_1,p_2)$ are real, which indeed is the case for the Feshbach dissociation states and the Gaussian states (4.2). We find that the joint probability splits into the two classical terms describing the probability distributions as given by the early slow and the late fast wave packet, respectively, and into a quantum term capturing their interference in the overlap region. Albeit we have not yet established the full correspondence to the Bell state correlations, we can already see at this stage that the interference term in the third line of (4.8) describes nonlocal correlations between the measured positions, which can be probed by varying the measurement times t_1 and t_2. Note that the phase in the interference term does not depend on the details of the setting, allowing us to analyze the nonlocal correlations without having to be specific about the early and late wave packets.

Gaussian evaluation

Evaluating (4.8) for the Gaussian ansatz (4.2), we get

$$\begin{aligned}\mathrm{P}(x_1,x_2|t_1,t_2) &= \frac{1}{2}\frac{m^2}{t_1t_2}\frac{2\sigma^2}{\pi\hbar^2}\exp\left[-\frac{2\sigma^2}{\hbar^2}\left(\frac{mx_1}{t_1}-p_\mathrm{f}\right)^2-\frac{2\sigma^2}{\hbar^2}\left(\frac{mx_2}{t_2}+p_\mathrm{f}\right)^2\right]\\ &+\frac{1}{2}\frac{m^2}{(t_1+\tau)(t_2+\tau)}\frac{2\sigma^2}{\pi\hbar^2}\exp\left[-\frac{2\sigma^2}{\hbar^2}\left(\frac{mx_1}{t_1+\tau}-p_\mathrm{s}\right)^2-\frac{2\sigma^2}{\hbar^2}\left(\frac{mx_2}{t_2+\tau}+p_\mathrm{s}\right)^2\right]\\ &+\frac{m^2}{\sqrt{t_1(t_1+\tau)t_2(t_2+\tau)}}\frac{2\sigma^2}{\pi\hbar^2}\exp\left[-\frac{\sigma^2}{\hbar^2}\left(\frac{mx_1}{t_1+\tau}-p_\mathrm{s}\right)^2-\frac{\sigma^2}{\hbar^2}\left(\frac{mx_1}{t_1}-p_\mathrm{f}\right)^2\right]\\ &\times\exp\left[-\frac{\sigma^2}{\hbar^2}\left(\frac{mx_2}{t_2+\tau}+p_\mathrm{s}\right)^2-\frac{\sigma^2}{\hbar^2}\left(\frac{mx_2}{t_2}+p_\mathrm{f}\right)^2\right]\\ &\times\cos\left[\frac{m}{2\hbar}\left(\frac{1}{t_1+\tau}-\frac{1}{t_1}\right)x_1^2+\frac{m}{2\hbar}\left(\frac{1}{t_2+\tau}-\frac{1}{t_2}\right)x_2^2-\phi\right].\end{aligned}\tag{4.9}$$

We can see that the envelope of the interference term is given by the overlap of the early and the late wave packets on each side. The Gaussian ansatz (4.2) has the additional benefit that it permits us to determine the joint probability (4.5) exactly, without having to employ the dispersion-dominance approximation (4.6). The exact expression is too complicated to be reproduced here, but it allows us in the following to confirm the validity of the dispersion-dominance approximation.

[3]Even when considering measurement times $t<t_\mathrm{m}$, the approximation still remains valid given the maximum offset Δt_max defined by the wave packet overlap is small compared to t_m. Indeed this will be the case for all scenarios we are interested in. However, one could restrict the discussion to measurement times $t>t_\mathrm{m}$ without loss of generality.

In Chapter 8 we will evaluate (4.8) for a Feshbach dissociation state of Lithium atoms that can be characterized by the parameters

$$\begin{aligned} \tau &= 1\,\mathrm{s}, \qquad \sigma = 50\,\mu\mathrm{m}, \\ v_\mathrm{f} &= 0.5\,\mathrm{cm/s}, \qquad v_\mathrm{s} = 0.45\,\mathrm{cm/s}, \end{aligned} \tag{4.10}$$

corresponding to $x_\mathrm{m} = 4.5\,\mathrm{cm}$ and $t_\mathrm{m} = 9\,\mathrm{s}$. A plot of the Gaussian fringe pattern (4.9) for the parameters (4.10) is given in Figure 4.2. The dispersion-dominance condition (4.7) evaluates to $m\sigma^2/\hbar t_\mathrm{m} = 0.025 \ll 1$ for these parameters, and comparing (4.9) numerically with the exact Gaussian result verifies that the asymptotic expression (4.8) indeed yields a valid approximation to the exact probability density. We consider this the justification of applying (4.8) to the Feshbach dissociation state characterized by the same frame parameters in Chapter 8.

4.2.2 Phase Linearization

We get a deeper insight into the parameter dependence of the fringe pattern (4.8) by linearizing in the vicinity of the meeting point and time. Such an approximation should yield a valid description over the extent of the overlap region given that the spatial and temporal widths of the envelope, Δx_max and Δt_max, are small compared to the meeting point x_m and the meeting time t_m, respectively,

$$\Delta x_\mathrm{max} \ll x_\mathrm{m} \quad \text{and} \quad \Delta t_\mathrm{max} \ll t_\mathrm{m}. \tag{4.11}$$

This is fairly well the case for our set of parameters (4.10), however, let me emphasize that the linearizability is not a necessary requirement for the success of the Bell test. Let us introduce the spatial and temporal deviations from the meeting point and time by

$$\begin{aligned} x_1 &= x_\mathrm{m} + \Delta x_1, \qquad t_1 = t_\mathrm{m} + \Delta t_1 \\ x_2 &= -x_\mathrm{m} + \Delta x_2, \qquad t_2 = t_\mathrm{m} + \Delta t_2. \end{aligned} \tag{4.12}$$

By expanding the arguments of the cosine and of the Fourier transforms $\tilde{\Psi}_\mathrm{S}$ and $\tilde{\Psi}_\mathrm{F}$ in the interference term in (4.8) to first order in Δx_i and Δt_i, and using $p_\mathrm{s} = m x_\mathrm{m}/(t_\mathrm{m}+\tau)$ and $p_\mathrm{f} = m x_\mathrm{m}/t_\mathrm{m}$, one obtains

$$\begin{aligned} &\mathrm{P}(x_1,x_2|t_1,t_2) \\ &\quad = \frac{1}{2}\frac{m^2}{(t_1+\tau)(t_2+\tau)} |\tilde{\Psi}_\mathrm{S}\left(\frac{m x_1}{t_1+\tau}, \frac{m x_2}{t_2+\tau}\right)|^2 + \frac{1}{2}\frac{m^2}{t_1 t_2} |\tilde{\Psi}_\mathrm{F}\left(\frac{m x_1}{t_1}, \frac{m x_2}{t_2}\right)|^2 \\ &\qquad + \frac{m^2}{t_\mathrm{m}(t_\mathrm{m}+\tau)} \tilde{\Psi}_\mathrm{S}\left(p_\mathrm{s}\left[1 - \frac{\Delta t_1}{t_\mathrm{m}+\tau} + \frac{\Delta x_1}{x_\mathrm{m}}\right], p_\mathrm{s}\left[-1 + \frac{\Delta t_2}{t_\mathrm{m}+\tau} + \frac{\Delta x_2}{x_\mathrm{m}}\right]\right) \\ &\qquad \times \tilde{\Psi}_\mathrm{F}\left(p_\mathrm{f}\left[1 - \frac{\Delta t_1}{t_\mathrm{m}} + \frac{\Delta x_1}{x_\mathrm{m}}\right], p_\mathrm{f}\left[-1 + \frac{\Delta t_2}{t_\mathrm{m}} + \frac{\Delta x_2}{x_\mathrm{m}}\right]\right) \\ &\qquad \times \cos\left[\frac{(p_\mathrm{f}-p_\mathrm{s})(\Delta x_1 - \Delta x_2)}{\hbar} - \frac{(E_\mathrm{kin,f} - E_\mathrm{kin,s})(\Delta t_1 + \Delta t_2)}{\hbar} + \frac{\tau p_\mathrm{f} p_\mathrm{s}}{\hbar m} + \phi\right], \end{aligned} \tag{4.13}$$

where we introduced the (mean) kinetic energies $E_\mathrm{kin,s} = p_\mathrm{s}^2/2m$ and $E_\mathrm{kin,f} = p_\mathrm{f}^2/2m$. We thus find that the spatial scale of the fringe pattern λ_hre is determined by the relative momentum between the early slow and the late fast wave packet,

$$\lambda_\mathrm{hre} = \frac{h}{p_\mathrm{f} - p_\mathrm{s}}, \tag{4.14}$$

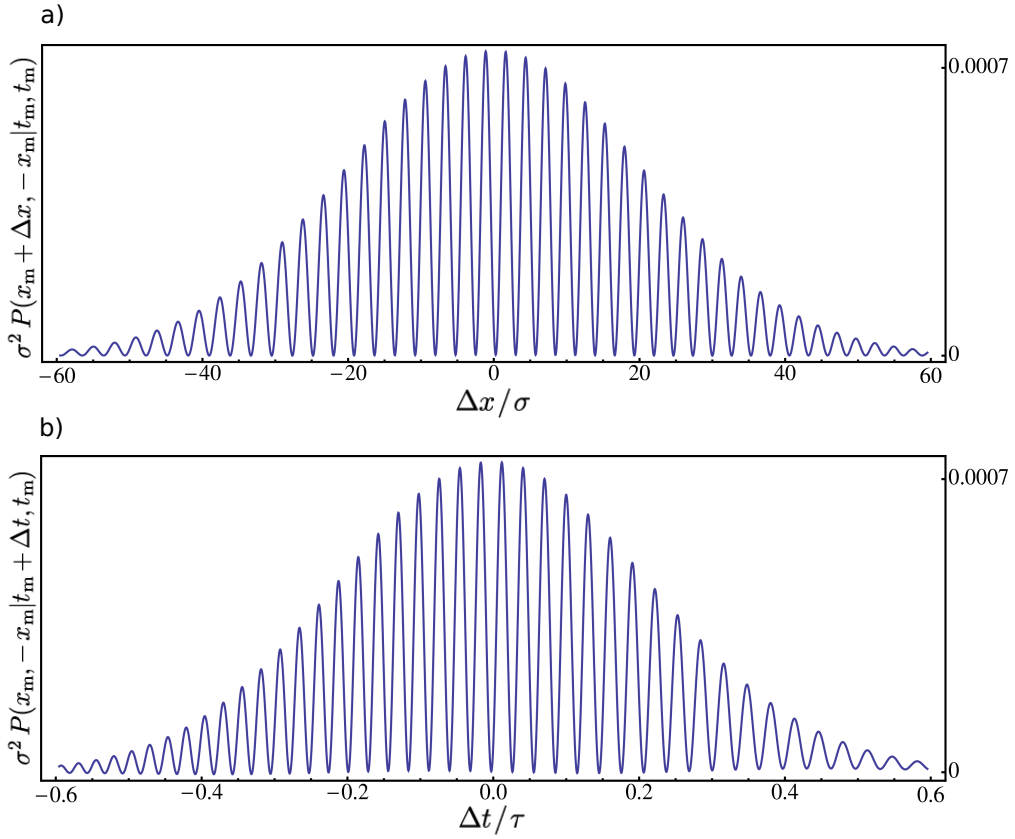

Figure 4.2: Joint probability $\mathrm{P}(x_1,x_2|t_1,t_2)$ for the Gaussian wave packets (4.2), as evaluated in (4.9), for the parameters (4.10). (a) Spatial fringe pattern as a function of the measured position x_1 in the vicinity of the meeting point x_m, conditioned on $x_2 = x_\mathrm{m}$, $t_1 = t_\mathrm{m}$ and $t_2 = t_\mathrm{m}$. The period $\lambda_\mathrm{hre} = 137\,\mu\mathrm{m}$ is sufficiently large to be resolvable with present day technology [91]. On the other hand, it is small compared to the spatial width Δx_max of the envelope, such that the envelope can be considered to be constant over the extent of a single period. This will allow us to make a crucial simplification when it comes to the dichotomization of the spatial fringe pattern. (b) Temporal fringe pattern as a function of the measurement time t_1 in the vicinity of the meeting time t_m, conditioned on $x_1 = x_\mathrm{m}$, $x_2 = x_\mathrm{m}$ and $t_2 = t_\mathrm{m}$. The period $T_\mathrm{hre} = 29\,\mathrm{ms}$ of the fringe pattern is sufficiently small as compared to the temporal width Δt_max of the envelope such that the experimenter can sweep the measurement time–which is under her control–over several periods without leaving the regime of optimum overlap. On the other hand, T_hre is comfortably large for being under experimental control.

and the temporal scale T_{hre} by the relative kinetic energy,

$$T_{\mathrm{hre}} = \frac{h}{E_{\mathrm{kin,f}} - E_{\mathrm{kin,s}}}. \tag{4.15}$$

For the parameters (4.10), they read $\lambda_{\mathrm{hre}} = 137\,\mu\mathrm{m}$ and $T_{\mathrm{hre}} = 29\,\mathrm{ms}$. The arguments of the Fourier transforms $\tilde{\Psi}_{\mathrm{S}}(p_1,p_2)$ and $\tilde{\Psi}_{\mathrm{F}}(p_1,p_2)$, on the other hand, make it manifest that the conditions (4.11) are equivalent to the requirement of sharply peaked momentum distributions,

$$\sigma_{p,\mathrm{s}} \ll p_{\mathrm{s}} \quad \text{and} \quad \sigma_{p,\mathrm{f}} \ll p_{\mathrm{f}}, \tag{4.16}$$

since the envelope widths $\Delta x_{\max}$ and $\Delta t_{\max}$ are determined by the momentum uncertainties $\sigma_{p,\mathrm{s}}$ and $\sigma_{p,\mathrm{f}}$[4]. In Chapter 6 I will demonstrate the feasibility of generating such states within the Feshbach dissociation scenario.

4.3 Chessboard dichotomization

Up to now, we have seen that the HRE state (4.1) indeed gives rise to nonlocal correlations. But to perform a Bell test we still have to find a prescription for the dichotomization of the position measurement outcomes, replacing the output ports of the interferometers in the DTE scenario. Instead of employing an active experimental element to be in charge of the dichotomization, we shall stick with the elementary position measurements and rather postprocess the gained data by assigning dichotomic values to the continuous position measurement outcomes.

More precisely, we are looking for dichotomization functions $\chi_{\sigma=\pm}(x)$, which are defined by assigning to each measurement outcome x either $\sigma = +1$ or $\sigma = -1$,

$$\chi_\sigma(x) = \begin{cases} 1 \text{ if } x \text{ has been assigned to dichotomic outcome } \sigma \\ 0 \text{ otherwise} \end{cases}, \tag{4.17}$$

such that they satisfy $\chi_+ + \chi_- = 1$ for all x. The resulting dichotomic joint probability then reads

$$\mathrm{P}(\sigma_1,\sigma_2|t_1,t_2) = \int \mathrm{d}x_1 \int \mathrm{d}x_2 \chi_{\sigma_1}(x_1)\chi_{\sigma_2}(x_2)\mathrm{P}(x_1,x_2|t_1,t_2). \tag{4.18}$$

It gives the probability to detect Particle 1 at a position that has been assigned to the dichotomic outcome σ_1 and to detect Particle 2 at a position that has been assigned to the dichotomic outcome σ_2.

In principle, the dichotomization functions may be arbitrary binary functions, and they might even depend on the setting of the corresponding side, i.e. $\chi_{\sigma_i}(x_i;t_i)$, since such a dependence can be understood as a local manipulation. However, such a conditioning on the setting is not necessary in the following.

Phase-adapted assignment

We want to accumulate positions that contribute with the same phase to the interference term in (4.8),

$$\Phi = \frac{m}{2\hbar}\left(\frac{1}{t_1+\tau} - \frac{1}{t_1}\right)x_1^2 + \frac{m}{2\hbar}\left(\frac{1}{t_2+\tau} - \frac{1}{t_2}\right)x_2^2 - \phi. \tag{4.19}$$

[4]Note that $\sigma_{p,\mathrm{s}}$ and $\sigma_{p,\mathrm{f}}$ characterize the two-particle momentum uncertainties of the corresponding HRE state components. In the case of unbalanced momentum uncertainties between the two particles, we take σ_p to be the larger one.

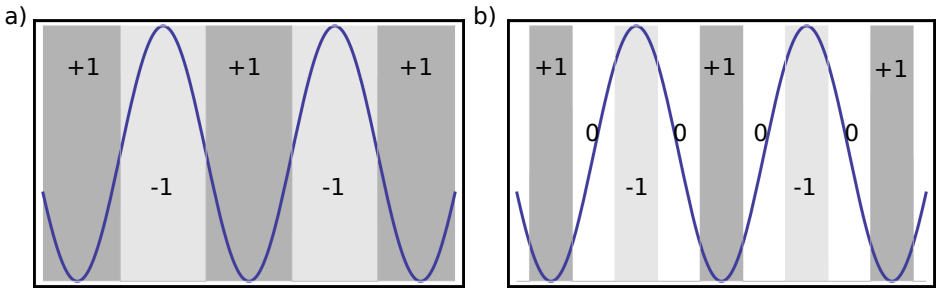

Figure 4.3: (a) A possible dichotomization of the position measurements bisects each period of the fringe pattern, into a half assigned to "+1" and a half assigned to "−1". (b) By including a third measurement outcome, "0", that is discarded, one can increase the fringe contrast of the resulting dichotomic correlation function (as a function of the measurement time), since then the maxima and minima of the "+1' and "−1" bins are more distinct.

An appropriate choice for the dichotomization functions adopts the periodicity of $\cos(\Phi)$, bisecting each period into a half assigned to "+1" and a half assigned to "−1", see Figure 4.3 (a). In this sense one may speak of (1D) "chessboard dichotomization". This can formally be described by the dichotomization functions

$$\begin{aligned} \chi_+(x) &= \frac{1}{2}\left(1+\operatorname{sgn}\left\{\cos\left[\frac{m}{2\hbar}\left(\frac{1}{t_\mathrm{m}+\tau}-\frac{1}{t_\mathrm{m}}\right)x^2\right]\right\}\right), \\ \chi_-(x) &= \frac{1}{2}\left(1-\operatorname{sgn}\left\{\cos\left[\frac{m}{2\hbar}\left(\frac{1}{t_\mathrm{m}+\tau}-\frac{1}{t_\mathrm{m}}\right)x^2\right]\right\}\right). \end{aligned} \tag{4.20}$$

Note that the times are kept fixed at t_m as compared to (4.19). This is important, since we want to capture the shift of the fringe pattern with respect to the chessboard pattern when varying the measurement times. In principle, the spatial period of $\cos(\Phi)$ is time dependent, but the resulting shift is of second order in Δx and Δt and hence negligible.

Equidistant assignment

From (4.18) we know that the dichotomization function is only relevant in the overlap region. Accounting for the generically good applicability of the linearized interference term in (4.13), one might then suggest to settle for the more transparent linear dichotomization functions

$$\chi_\pm(x) = \frac{1}{2}\left(1 \pm \operatorname{sgn}\{\cos[kx]\}\right), \tag{4.21}$$

with $k = (p_\mathrm{f} - p_\mathrm{s})/\hbar$. However, this turns out not to be an alternative, since even small quadratic corrections to the linear fringe pattern in (4.13) effect an increasing detuning between the fringe pattern and the chessboard pattern towards the outer ends of the envelope and hence spoil the phase correlation required over the entire extent of the envelope. Nevertheless, it remains valid to assume that the dichotomization function (4.20) can be linearized over the extent of each single period. This is used below for an analytic treatment of (4.18). Let me stress once more that the structure of the dichotomization function has no consequences for the experimental procedure in the laboratory, but only

affects the interpretation of the gained data. The appropriate choice of the dichotomization function, though, might decide whether it is possible to violate a Bell inequality or not!

4.3.1 Scale separation and local linearizability

In principle, we could determine the dichotomic joint probability (4.18) numerically, using the joint probability density (4.8) and either the quadratic dichotomization functions (4.20) or the linear ones (4.21). The visibility of the fringe pattern evaluated with the linear dichotomization functions would be reduced as compared to the former ones, which is due to the detuning of the "wrong" chessboard pattern towards the outer ends of the envelope. However, we can get a deeper insight into the structure of the correlations, if we make use of the fact that the phase of the fringe pattern is linearizable at least over the range of a single period ("local linearizability"), meaning that we can assign a specific wave length to each period of the spatial fringe pattern. If we further assume that the envelope of the fringe pattern varies slowly over the extent of a single period ("scale separation"), we can take each period to yield the same contribution to (4.18), weighted by the corresponding magnitude of the envelope. More precisely, let $\chi(x)$ be an oscillating function with a (constant) period λ, and $E(x)$ an envelope function that varies slowly on the scale λ. We can then write to good approximation

$$\int_{-\infty}^{\infty} \mathrm{d}x \chi(x) E(x) \approx \int_{-\infty}^{\infty} \mathrm{d}x E(x) \frac{1}{\lambda} \int_{0}^{\lambda} \mathrm{d}x' \chi(x'). \tag{4.22}$$

A derivation of (4.22) under the assumption of scale separation can be found in Appendix A.2. It is clear that it is not necessary to require that all periods share the same wave length (corresponding to "global linearizability"). In fact, in the case of varying wave lengths (local linearizability), the right-hand side of (4.22) takes exactly the same form, only that this time we have to pick an exemplary period for the second integral. That both assumptions, local linearizability and scale separation, are justified for the parameters (4.10) can be seen from Figure 4.2.

Applying (4.22) to (4.18) using (4.8), one obtains

$$\begin{aligned}
&\mathrm{P}(\sigma_1,\sigma_2|t_1,t_2) \\
&\quad = \left\{ \int_{-\infty}^{\infty} \mathrm{d}x_1 \int_{-\infty}^{\infty} \mathrm{d}x_2 \frac{1}{2} \frac{m^2}{(t_1+\tau)(t_2+\tau)} \left| \tilde{\Psi}_{\mathrm{S}} \left(\frac{m x_1}{t_1+\tau}, \frac{m x_2}{t_2+\tau} \right) \right|^2 \right. \\
&\qquad \left. + \int_{-\infty}^{\infty} \mathrm{d}x_1 \int_{-\infty}^{\infty} \mathrm{d}x_2 \frac{1}{2} \frac{m^2}{t_1 t_2} \left| \tilde{\Psi}_{\mathrm{F}} \left(\frac{m x_1}{t_1}, \frac{m x_2}{t_2} \right) \right|^2 \right\} \\
&\qquad \times \frac{1}{\lambda^2} \int_{x_{\mathrm{m}}-\lambda/2}^{x_{\mathrm{m}}+\lambda/2} \mathrm{d}x_1' \int_{-x_{\mathrm{m}}-\lambda/2}^{-x_{\mathrm{m}}+\lambda/2} \mathrm{d}x_2' \chi_{\sigma_1}(x_1') \chi_{\sigma_2}(x_2') \\
&\qquad + \int_{-\infty}^{\infty} \mathrm{d}x_1 \int_{-\infty}^{\infty} \mathrm{d}x_2 \frac{m^2}{\sqrt{t_1(t_1+\tau)t_2(t_2+\tau)}} \tilde{\Psi}_{\mathrm{S}} \left(\frac{m x_1}{t_1+\tau}, \frac{m x_2}{t_2+\tau} \right) \tilde{\Psi}_{\mathrm{F}} \left(\frac{m x_1}{t_1}, \frac{m x_2}{t_2} \right) \\
&\qquad \times \frac{1}{\lambda^2} \int_{x_{\mathrm{m}}-\lambda/2}^{x_{\mathrm{m}}+\lambda/2} \mathrm{d}x_1' \int_{-x_{\mathrm{m}}-\lambda/2}^{-x_{\mathrm{m}}+\lambda/2} \mathrm{d}x_2' \chi_{\sigma_1}(x_1') \chi_{\sigma_2}(x_2') \\
&\qquad \times \cos \left[\frac{m}{2\hbar} \left(\frac{1}{t_1+\tau} - \frac{1}{t_1} \right) x_1'^2 + \frac{m}{2\hbar} \left(\frac{1}{t_2+\tau} - \frac{1}{t_2} \right) x_2'^2 - \phi \right].
\end{aligned} \tag{4.23}$$

For the evaluation of the periodic integrals we choose the periods enclosing the meeting points, which are characterized by the wave length $\lambda = \lambda_{\mathrm{hre}} = h/(p_{\mathrm{f}} - p_{\mathrm{s}})$. The inten-

sity terms of (4.23) are evaluated straightforwardly using the normalization of the wave functions,

$$\int_{-\infty}^{\infty} \mathrm{d}x_1 \int_{-\infty}^{\infty} \mathrm{d}x_2 \frac{m^2}{t_1 t_2} \left| \tilde{\Psi}_{\mathrm{F/S}} \left(\frac{m x_1}{t_1}, \frac{m x_2}{t_2} \right) \right|^2 = 1, \tag{4.24}$$

and

$$\frac{1}{\lambda} \int_{x_\mathrm{m}-\lambda/2}^{x_\mathrm{m}+\lambda/2} \mathrm{d}x' \chi_\sigma(x') = \frac{1}{2}. \tag{4.25}$$

Concerning the interference term, we exploit that in the direct vicinity of the meeting points (at least within the first few periods) the linearizations (4.13) and (4.21) yield excellent approximations[5]. The periodic integrals thus reduce to integrals of the form

$$\begin{aligned} &\frac{1}{\lambda^2} \int_{\sigma_1\lambda/4-\lambda/4}^{\sigma_1\lambda/4+\lambda/4} \mathrm{d}\Delta x_1 \int_{\sigma_2\lambda/4-\lambda/4}^{\sigma_2\lambda/4+\lambda/4} \mathrm{d}\Delta x_2 \cos\left[\frac{2\pi}{\lambda} (\Delta x_1 - \Delta x_2) + \varphi \right] \\ &= \frac{1}{\pi^2} \sin^2\left[\frac{\pi}{2}\right] \cos\left[\sigma_1 \frac{\pi}{2} - \sigma_2 \frac{\pi}{2} + \varphi \right] \\ &= \frac{1}{4} \mathrm{sinc}^2\left[\frac{\pi}{2}\right] \sigma_1 \sigma_2 \cos[\varphi]. \end{aligned} \tag{4.26}$$

Here we chose the "$\sigma = +1$"-domain to lie in the interval $[x_\mathrm{m}, x_\mathrm{m} + \lambda/2]$, and the "$\sigma = -1$"-domain in the interval $[x_\mathrm{m} - \lambda/2, x_\mathrm{m}]$. This is done for convenience, utilizing that the dichotomization functions can always be redefined by adding arbitrary constant phases. In the last line we used that there is no phase shift for σ_1 and σ_2 having equal sign, but that there is a phase shift of π for opposite signs, which corresponds to a sign change of the cosine.

4.3.2 Dichotomic correlation function

Putting all together, one ends up with

$$P(\sigma_1, \sigma_2 | t_1, t_2) = \frac{1}{4} \left\{ 1 + \sigma_1 \sigma_2 E(t_1, t_2) \mathrm{sinc}^2\left[\frac{\pi}{2}\right] \cos\left[\omega(\Delta t_1 + \Delta t_2) - \phi' \right] \right\}, \tag{4.27}$$

where we have defined the envelope function

$$E(t_1, t_2) = \int \mathrm{d}x_1 \int \mathrm{d}x_2 \frac{m^2}{\sqrt{t_1(t_1+\tau) t_2 (t_2+\tau)}} \tilde{\Psi}_\mathrm{S} \left(\frac{m x_1}{t_1 + \tau}, \frac{m x_2}{t_2 + \tau} \right) \tilde{\Psi}_\mathrm{F} \left(\frac{m x_1}{t_1}, \frac{m x_2}{t_2} \right), \tag{4.28}$$

the frequency $\omega = (p_\mathrm{f}^2 - p_\mathrm{s}^2)/2m\hbar$, and the phase $\phi' = \tau p_\mathrm{s} p_\mathrm{f}/\hbar m + \phi$. As desired, we find that the dichotomic joint probability (4.27) takes a similar structure as the Bell state correlation function (2.7), or more precisely (2.21). This time, the freely choosable measurement times t_1, t_2 take the role of the control parameters. Note that the time dependence was linearized in (4.27), which is legitimate since it is sufficient to sweep over a few periods within the vicinity of the meeting times. In contrast to the DTE scenario, we do not have an analogue for "out of plane"-measurements, there implemented by the beam splitting ratios. This is irrelevant for the possibility of a Bell violation, though. More incisive with this respect is the inherent visibility reduction as represented by the factor $\mathrm{sinc}^2[\pi/2] = 0.41$, which rules out the possibility of a Bell violation even in the case of optimum overlap, $E(t_\mathrm{m}, t_\mathrm{m}) \approx 1$. This reduction is an inevitable consequence of

[5] For (4.21) this is true up to an irrelevant constant phase. Anyway, the dichotomization functions can be redefined freely by adding arbitrary phases.

the dichotomization of the fringe pattern. I will show below how post-selection can be used to overcome this constraint.

The envelope function (4.28) captures the overlap of the early slow and late fast wave packets. Evaluated at the meeting times, it corresponds to $E(t_\mathrm{m},t_\mathrm{m}) = \langle \mathrm{S}|\mathrm{F}\rangle$. Since the envelope function directly influences the visibility of the fringe pattern, we should strive for parameters that optimize the overlap $\langle \mathrm{S}|\mathrm{F}\rangle$, which is mainly determined by an interplay of the velocity difference $v_\mathrm{f} - v_\mathrm{s}$ and the momentum widths $\sigma_{p,\mathrm{s}}$ and $\sigma_{p,\mathrm{f}}$. In particular, the momentum uncertainties should not be smaller than the momentum difference.

For the Gaussian wave packets (4.2), the envelope function (4.28) can be evaluated analytically, yielding

$$E(t_\mathrm{m}+\Delta t_1, t_\mathrm{m}+\Delta t_2) = \frac{2p_\mathrm{f}p_\mathrm{s}}{p_\mathrm{f}^2+p_\mathrm{s}^2} \exp\left[-\frac{\sigma^2}{\tau^2\hbar^2}\frac{(p_\mathrm{f}-p_\mathrm{s})^4}{p_\mathrm{f}^2+p_\mathrm{s}^2}(\Delta t_1^2+\Delta t_2^2)\right]. \tag{4.29}$$

This can be used to compare the analytic result (4.27) with the numerical evaluation of (4.18) for the parameters (4.10) and using (4.2) and (4.20), which reveals excellent agreement and thus verifies the validity of the approximations. Note that for the parameters (4.10), the envelope function (4.29) takes the value $E(t_\mathrm{m},t_\mathrm{m}) = 0.99$, demonstrating optimum overlap.

4.4 Post-selection

By investigating the dichotomic joint probability (4.27) we found that, in spite of the structural similarity with Bell correlations, the inherent visibility reduction due to the factor $\mathrm{sinc}^2[\pi/2]$ spoils its ability to violate a Bell inequality. The reason for this factor can be traced back to the fact that, no matter what is the phase relation between the chessboard pattern and the fringe pattern, there is always a finite probability to detect each dichotomic outcome at a given pair of measurement times, which can be seen by inspecting Figure 4.3 (a). We can mitigate this and increase the visibility by narrowing the "$+1$" and "-1" bins, as shown in Figure 4.3(b). This implies the introduction of a third measurement outcome, "0", which is disregarded in the correlation analysis. Formally, this corresponds to a post-selection procedure, which means that we have to rely on the fair sampling assumption in order to validate the violation of a Bell inequality. Let me emphasize, though, that we have the complete sampling at hand, the post-selection being only a matter of the interpretation of the gained data. Moreover, we can reinterpret the same data according to different, phase shifted dichotomization functions. Then each position measurement contributes to the correlation for appropriate phase choices. In this sense, the fair sampling requirement can be considered to be weakened.[6]

[6] Since we have the complete sampling at hand, it should in principle be possible to prove the validity of the fair sampling assumption; this would be a desirable goal for a future investigation, and it would quash the suspicion that the Bell violation is based on post-selecting a biased sample [92–94]. At this point, the transparency of the applied post-selection prescription may suffice as a justification.

4.4.1 Post-selected correlation function

The post-selection can be taken into account by choosing the dichotomization functions according to

$$\begin{aligned}\chi_+(x) &= \frac{1}{2}\left(1+\operatorname{sgn}\left\{\cos\left[\frac{m}{2\hbar}\left(\frac{1}{t_\mathrm{m}+\tau}-\frac{1}{t_\mathrm{m}}\right)x^2\right]-\cos\left[p\frac{\pi}{2}\right]\right\}\right),\\ \chi_-(x) &= \frac{1}{2}\left(1-\operatorname{sgn}\left\{\cos\left[\frac{m}{2\hbar}\left(\frac{1}{t_\mathrm{m}+\tau}-\frac{1}{t_\mathrm{m}}\right)x^2\right]+\cos\left[p\frac{\pi}{2}\right]\right\}\right). \quad (4.30)\end{aligned}$$

The parameter $p\in[0,1]$ denotes the post-selected fraction, hence $p=1$ corresponds to including all measurement outcomes, as was the case above. We can repeat the steps leading from (4.18) to (4.27) using (4.30), the validity of all assumptions is untouched by the exchange of the dichotomization functions. The only modification takes place when determining the periodic integrals in the interference term of (4.23), which now read

$$\begin{aligned}&\frac{1}{\lambda^2}\int_{\sigma_1\lambda/4-p\lambda/4}^{\sigma_1\lambda/4+p\lambda/4}\mathrm{d}\Delta x_1\int_{\sigma_2\lambda/4-p\lambda/4}^{\sigma_2\lambda/4+p\lambda/4}\mathrm{d}\Delta x_2\cos\left[\frac{2\pi}{\lambda}(\Delta x_1-\Delta x_2)+\varphi\right]\\ &=\frac{1}{\pi^2}\sin^2\left[\frac{\pi}{2}p\right]\cos\left[\sigma_1\frac{\pi}{2}-\sigma_2\frac{\pi}{2}+\varphi\right] \quad (4.31)\\ &=\frac{1}{4}\mathrm{sinc}^2\left[\frac{\pi}{2}p\right]\sigma_1\sigma_2\cos[\varphi].\end{aligned}$$

With this, the joint probability to detect Particle 1 at a position that has been assigned to the outcome σ_1 and to detect Particle 2 at a position that has been assigned to the outcome σ_2 reads

$$P(\sigma_1,\sigma_2|t_1,t_2)=\frac{1}{4}p^2\left\{1+\sigma_1\sigma_2E(t_1,t_2)\mathrm{sinc}^2\left[\frac{\pi}{2}p\right]\cos\left[\omega(\Delta t_1+\Delta t_2)-\phi'\right]\right\}. \quad (4.32)$$

By choosing $p<1$, we can increase the fringe contrast which is still limited by the envelope function. Assuming $E(t_\mathrm{m},t_\mathrm{m})\approx 1$ (as it was the case for the Gaussian envelope (4.29) when evaluated with the parameters (4.10)), a choice of $p<0.63$ supports the violation of a Bell inequality. Note that (4.32) is not normalized for $p<1$,

$$\sum_{\sigma_1,\sigma_2=\pm1}P(\sigma_1,\sigma_2|t_1,t_2)=p^2<1.$$

Normalizing to post-selected events, we get

$$P^{(\mathrm{ps})}(\sigma_1,\sigma_2|t_1,t_2)=\frac{1}{4}\left\{1+\sigma_1\sigma_2E(t_1,t_2)\mathrm{sinc}^2\left[\frac{\pi}{2}p\right]\cos\left[\omega(\Delta t_1+\Delta t_2)-\phi'\right]\right\}. \quad (4.33)$$

This is our final result, showing that it is possible to regain Bell correlations in the HRE scenario that are strong enough to violate a Bell inequality, given the parameters are chosen appropriately (and accepting post-selection). In Chapter 8 I will demonstrate that the Feshbach dissociation scenario permits to generate HRE states that fulfill these requirements.

4.4.2 Summary

To conclude this part, the HRE scenario establishes an alternative for the demonstration of nonclassical correlations in the motion. In contrast to the DTE scenario, the correspondence to the spin-based Bell test is only revealed on the level of correlations. The

measurement times take the role of the "in plane" Bell control parameters, whereas there is no obvious analogue for "out of plane"-measurements. A post-selection procedure ensures sufficient fringe contrast as required for the violation of a Bell inequality. This takes the fair-sampling assumption as a basis, however, by redefining the dichotomization prescription all measurements can contribute to a Bell violation.

The idea of abandoning the interferometers simplifies the experimental setup considerably, but this comes at the cost of a required phase stability over the whole extent of the experiment and a high spatial and temporal measurement accuracy. In Chapter 8 I will argue that laser illumination of the dissociated atoms in the overlap regions indeed provides the required resolution [91]. This way, the HRE state represents a complementary approach, interesting on its own, based on a genuine matter wave state with no photonic analogue.

Chapter 5

A proposed experiment based on ultracold atoms

In the previous chapters I introduced two classes of dissociation states and exposed their potential to cause nonlocal correlations. Both the DTE and the HRE states share a very similar, simple generation protocol within the conceived dissociation scheme: a sequence of two dissociation pulses delocalizes each atom into a superposition of consecutive wave packets, such that the wave packets are entangled in the dissociation times. Hence, choosing similar parameters, both states are amenable to the same experimental setup, which permits us to treat them at the same time.

In the following chapters I will argue that it is possible to realize these states within a scenario based on the dissociation of ultracold Feshbach molecules is possible and indeed seems to be favorable. The advantages are obvious: A Bose-Einstein condensate (BEC) as a source provides initial states of excellent reproducibility, and atoms propagating at velocities of cm/s can be optically guided and suitably detected by laser illumination. The resolution of the corresponding de Broglie wave lengths, which are on the order of micrometers, does not pose outstanding experimental challenges. And a time separation τ on the order of seconds results in spatial separations between the early and late wave packets on the order of centimeters, rendering their delocalization truly macroscopic. Apart from its fundamental relevance, such a centimeter-scale delocalization is also important for practical reasons in the DTE scenario, since the separation between the early and the late wave packets determines the size of the interferometers and should thus not be too small.

In this chapter, I work out a concrete experimental setup that provides the frame for the DTE and the HRE Bell test, respectively. The analysis of the Feshbach dissociation dynamics, which will be given in the following chapter, then enables us to investigate their viability in detail in the Chapters 7 and 8, respectively.

5.1 Experimental setup: overview

Molecular Bose-Einstein condensate

We consider a BEC of Feshbach molecules in an optical dipole trap, which can be established by two perpendicularly crossing laser beams, see Figure 5.1 a). Producing molecular BECs (mBEC) and tuning the interactions via Feshbach resonances is nowadays routine [23–31, 34], and the use of their controlled dissociation for spectroscopic purposes has been demonstrated experimentally [32, 33], as well.

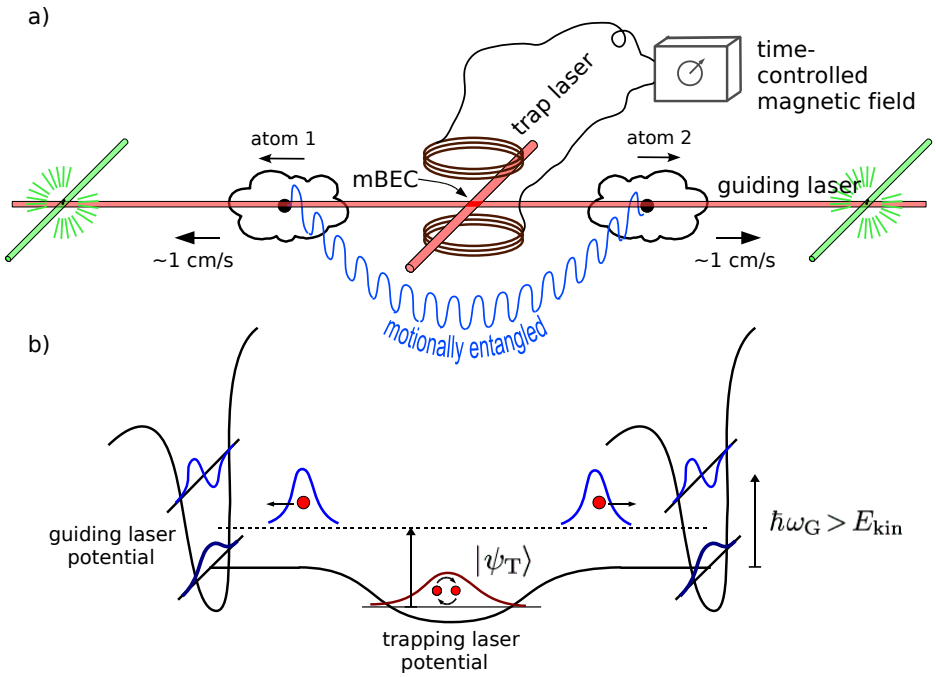

Figure 5.1: a) Setup for generating pairs of motionally entangled pairs of atoms by dissociation of Feshbach molecules. Initially a BEC of approximately 10^2 Feshbach molecules resides in a trap constituted by two crossing laser beams. An externally controlled magnetic field induces dissociation of on average one molecule per trial and thus generates a pair of entangled atoms counter-propagating along the laser guide at a velocity on the order of $1\,\mathrm{cm/s}$. The asymptotic two-atom state in the laser guide is determined by the trap and guide geometry and by the shape of the dissociation pulse, see Chapter 6. When desired, the atoms can be detected conveniently by laser illumination; in the HRE scenario this would be in the overlap region, in the DTE scenario after the passage of Mach-Zehnder interferometers (not shown). b) The dissociation pulse promotes the initially trapped molecules to a pair of counter-propagating atoms. The lasers are chosen such that the trap laser potential can be overcome easily with the energy supply from the magnetic field sweep, whereas the atoms are transversally frozen in the ground state due to $\hbar\omega_G > E_{kin}$.

To be specific, I suggest to use a BEC produced from a 50:50 spin mixture of fermionic ^{6}Li. Such a fermionic mixture is favorable compared to bosonic ingredients, since huge lifetimes of more than 10s can be achieved due to the Pauli blocking of detrimental 3-body collisions [25]. This makes truly macroscopic time separations τ between the two dissociation pulses conceivable, and we may choose $\tau = 1\text{s}$ from now on. It has been demonstrated that the molecular ^{6}Li BEC can be prepared efficiently and with near-perfect purity [25], and the comparatively small mass of lithium reconciles reasonable propagation velocities, on the order of $1\text{cm}/\text{s}$, with resolvable de Broglie wave lengths, on the order of $10\mu\text{m}$.

Extraction of an atom pair

The weak trap laser creates an elongated longitudinal trap within the wave guide produced by the strong guiding laser. The preparation is arranged such that only a small number of molecules, on the order of 10^2, remains in the BEC at the end, such that one may neglect interactions between different molecules. The molecules can then be considered to be in a product state with the center of mass motion given by the ground state of the trap, whereas the relative motion describes a bound molecular state. The latter can be turned into a Feshbach resonance by varying the external magnetic field, which allows one to dissociate the atoms in a controlled way. By applying one or several appropriately chosen dissociation pulses, a single molecule dissociates into two counter-propagating atoms on average, and we post-select the single-dissociation events.

The pulses are chosen to provide the atoms with a kinetic energy sufficiently large to overcome the trap potential in longitudinal direction, but still below the threshold to get beyond the ground state transversally, see Figure 5.1 b). This way we may end up with two dissociated atoms, counter-propagating with a relative velocity of $1\text{cm}/\text{s}$ along the guiding laser axis, whose two-particle state is determined by the initial state of the molecule and the dissociation pulse shape, as I will demonstrate in the next chapter. In particular, by applying a sequence of two appropriate dissociation pulses, one then can generate DTE and HRE states, respectively. Their detailed elaboration will be given in Chapters 6, 7 and 8.

DTE and HRE states

After the completion of the dissociation sequence, and for our chosen time separation of $\tau = 1\,\text{s}$ between the early and the late dissociation pulse, the corresponding early and late wave packets of each particle are envisaged to propagate at a velocity of $5\,\text{mm}/\text{s}$ (in the case of the HRE scenario, the early wave packets are slightly slower), separated by a distance of 5 mm on each side. This constitutes a truly macroscopic delocalization of each atom. Immediately after the dissociation process, the widths of the early and late single-particle wave packets turn out to be on the order of about $100\,\mu\text{m}$, as we will see in the Chapters 7 and 8. Their narrow momentum distributions guarantee that these wave packet extensions are not appreciably modified during the propagation to the measurement sites if the propagation time does not exceed about 10 s, which corresponds to the aspired distance on the order of 10 cm between the measurement sites. The early and late wave packets are thus spatially still sufficiently distinct when arriving at the interferometers for the switches to be applicable in the DTE scenario.

Detection

The final detection of the atoms can be achieved with laser illumination. In the HRE scenario this would be in the overlap region of the fast and the slow wave packet, in the DTE scenario the measurement would be done after passing the Mach-Zehnder interferometers, whose implementation will be discussed in Chapter 7. Such a fluorescence detection of the slow, strongly confined atoms can be done with single particle resolution [91], such that it is easy to disregard the cases of too many atom pairs in the process. For a start, we stick to the simple post-selection procedure; in a more refined setup it is conceivable to use a specially prepared optical lattice where each site is occupied by at most one molecule [95].

5.2 Trap and guide parameters

I now show that the above described laser setting is experimentally viable for an aspired relative velocity between the counter-propagating atoms of $v_{\mathrm{rel}} = 1\,\mathrm{cm/s}$ and an overall extension of the setup on the order of $10\,\mathrm{cm}$.[1] The corresponding de Broglie wave length $\lambda_{\mathrm{rel}} = 12.4\mu\mathrm{m}$, which sets the scale for the fringe patterns, is in compliance with viable stability requirements for the setup.

5.2.1 Gaussian laser beams

We assume that both lasers can be described by Gaussian beams, then the field intensity as a function of the distance z from the beam center and of the radial distance from the beam axis r is given by [96]

$$I(r,z) = \frac{2P}{\pi w(z)^2} \exp\left(-2\frac{r^2}{w(z)^2}\right), \tag{5.1}$$

where P denotes the laser power. The beam width or spot size $w(z)$ follows from $w(z) = w_0\sqrt{1+(z/z_0)^2}$ and takes its minimum, the beam waist w_0, at the beam center $z = 0$. The Rayleigh length $z_0 = \pi w_0^2/\lambda$ describes the characteristic curvature scale of the beam. Mediated by their polarizability α_{Li} the lithium atoms encounter the potential [97]

$$U(r,z) = -\frac{2\pi\alpha_{\mathrm{Li}}}{c} I(r,z). \tag{5.2}$$

We take the potential, or more precisely the atomic polarizability, to be independent of the distance between the atoms. This corresponds to assigning to the molecules the doubled polarizability, $\alpha_{\mathrm{Li}_2} = 2\alpha_{\mathrm{Li}}$, which is justified for the weakly bound Feshbach molecules. For lithium atoms the static polarizability reads $\alpha_{\mathrm{Li},0} = 24.33\mathrm{\AA}^3$, where static means that the laser frequency is far off any atomic transition. In fact, tuning the laser frequency ν close to such a transition enhances the polarizability according to

$$\alpha_{\mathrm{Li}} = \alpha_{\mathrm{Li},0}\frac{E_r^2}{E_r^2 - (h\nu)^2}, \tag{5.3}$$

where E_r denotes the corresponding resonance energy [98]. On the one hand, a large polarizability reduces the required laser power, on the other hand, it enhances the detrimental scattering of photons, as we will see below. We choose a wave length of $\lambda = 1\mu\mathrm{m}$

[1] In the HRE scenario the mentioned relative velocity may be assigned to the fast wave packets. However, the slow wave packets are taken to be only marginally smaller, such that all results are applicable to them, too.

for both lasers, which lies in the vicinity of the lithium resonance $E_r = 1.848\,\mathrm{eV}$ and thus results in a polarizability of $\alpha_{\mathrm{Li}} = 44.25\text{Å}^3$.

We arrange the two perpendicular lasers such that they cross at their waists, hence locating the BEC in the region of highest intensity. Evaluated at the beam center and using the Gaussian intensity profile (5.1), the potential (5.2) reads

$$U(r,0) = -\frac{4P\alpha_{\mathrm{Li}}}{cw_0^2}\exp\left(-2\frac{r^2}{w_0^2}\right), \tag{5.4}$$

yielding the trap depth $U_0 = 4P\alpha_{\mathrm{Li}}/cw_0^2$. The harmonic approximation of the potential, $U(r,0) \approx -U_0 + (m/2)\omega^2 r^2$, provides the trap frequency

$$\omega = \frac{4}{w_0^2}\sqrt{\frac{P\alpha_{\mathrm{Li}}}{cm}}. \tag{5.5}$$

This frequency applies also to the molecules, since the factor 2 in mass is compensated by the same factor in polarization. The consistency of the approximation requires that $\sigma_{x,\mathrm{G}}/w_{0,\mathrm{G}} \ll 1$ and $\sigma_{x,\mathrm{T}}/w_{0,\mathrm{T}} \ll 1$, where $\sigma_{x,\mathrm{G}} = \sqrt{\hbar/2\omega_{\mathrm{G}}m}$ and $\sigma_{x,\mathrm{T}} = \sqrt{\hbar/4\omega_{\mathrm{T}}m}$ describe the position uncertainties of the (Gaussian) ground states of the harmonic potentials. In the case of the trap laser the relevant position uncertainty is set by the center of mass state with $M = 2m$.

So far we have constrained us to radially symmetric beams. In case of the trap laser it turns out to be preferable to choose an elliptic beam in order to keep the required laser power low. Generalizing the potential (5.4) to the elliptic case,

$$U(x,y,0) = -\frac{4P\alpha_{\mathrm{Li}}}{c\,w_{0,x}w_{0,y}}\exp\left(-2\frac{x^2}{w_{0,x}^2} - 2\frac{y^2}{w_{0,y}^2}\right), \tag{5.6}$$

we can infer the trap depth $U_0 = 4P\alpha_{\mathrm{Li}}/cw_{0,x}w_{0,y}$, and the resulting trap frequencies read $\omega_x = (4/w_{0,x}^2)\sqrt{P\alpha_{\mathrm{Li}}w_{0,x}/cm\,w_{0,y}}$ and $\omega_y = (4/w_{0,y}^2)\sqrt{P\alpha_{\mathrm{Li}}w_{0,y}/cm\,w_{0,x}}$.

5.2.2 The guiding laser

In the following a viable set of parameters will be specified that admits the aspired experimental implementation. With respect to the guiding laser, we have to keep in mind that it connects the two detection regions, thus serving as an atom guide which must compensate the gravitational force. Moreover, it should be chosen sufficiently strong that the transverse motion of the atoms remains frozen in the ground state, since only then an effectively one-dimensional description of the atomic motion can be used.

To this end, we take the guiding laser to be operated at a power of $P_{\mathrm{G}} = 32.85\,\mathrm{W}$ with a waist of $w_{0,\mathrm{G}} = 216\,\mu\mathrm{m}$, such that the resulting potential has the trap depth $U_{0,\mathrm{G}}/k_{\mathrm{B}} = 30\,\mu\mathrm{K}$. It thus is strong enough to compensate gravitation, which can be seen by comparing the force exerted by the laser, $F(r) = -U'(r,0)$, to the gravitational force, mg. Evaluated at its maximum, the optical force reads $F_{max} = 2U_0\exp(-1/2)/w_0$, which compares to the gravitational force as $F_{max}/mg \approx 24$. An estimate of the number of bound states, on the other hand, follows from the classical phase space volume Φ for the Hamiltonian $H(x,p) = p^2/2m - U_{0,\mathrm{G}}\exp(-2x^2/w_{0,\mathrm{G}}^2)$, whose bound regime $H < 0$ is limited by

$$\Phi = \iint_{H<0}\mathrm{d}x\,\mathrm{d}p = \int_{-\infty}^{\infty}\mathrm{d}x\int_{-p_{\max}(x)}^{p_{\max}(x)}\mathrm{d}p = 4w_0\sqrt{\pi m U_{0,\mathrm{G}}/2}, \tag{5.7}$$

where $p_{\max}(x) = \sqrt{2mU_{0,\mathrm{G}}}\exp(-x^2/w_{0,\mathrm{G}}^2)$. The number of bound states can then be estimated as $N_{\mathrm{b,G}} = \Phi/2\pi\hbar = 3325$, showing that the ground state indeed is deeply bound. The implied transverse trap frequency of $\omega_{\mathrm{G}}/2\pi = 300\,\mathrm{Hz}$, on the other hand, guarantees that the desired dissociation velocity of $v_{\mathrm{rel}} = 1\mathrm{cm/s}$ does not lead to transversal excitations, since the corresponding single-particle kinetic energy E_{kin} remains below the required excitation energy, $\hbar\omega_{\mathrm{G}}/E_{\mathrm{kin}} = 1.4$. The use of the harmonic approximation is justified by the smallness of the ratio $\sigma_{x,\mathrm{G}}/w_{0,\mathrm{G}} = 0.008 \ll 1$.

The resulting Rayleigh length of about $z_{0,\mathrm{G}} = 15\,\mathrm{cm}$ sets the scale for the maximum extension of the whole setup. The required 15 s to traverse this distance are not at risk due to photon scattering, since the scattering rate $R = I_0\sigma/h\nu$ following from the laser intensity $I_0 = 2P/\pi w_0^2$ and the Rayleigh cross section $\sigma(\nu) = (8\pi/3)(2\pi\nu/c)^4\alpha_{\mathrm{Li}}^2(\nu)$ evaluates for the guiding laser as $R_{\mathrm{G}} = 0.05\,\mathrm{s}^{-1}$, which permits the overall duration of a single experiment to reach 20 s.

5.2.3 The trap laser

The second laser beam intersects the guiding laser perpendicularly, creating an elongated dipole trap for the BEC within the laser guide. The trap must be sufficiently shallow to be overcome with reasonable magnetic field pulses. Moreover, the resulting longitudinal ground state $|\psi_{\mathrm{T}}\rangle$, which is supposed to determine the center of mass state of the trapped molecules, should correspond to a sufficiently narrow momentum distribution, guaranteeing that dispersion-induced distortion between the early and late wave packets still admits the feasibility of the Bell tests. This demands a comparatively small trap frequency. Specifically, for an atomic propagation velocity of $5\,\mathrm{mm/s}$, the trap frequency should not greatly exceed $\omega_{\mathrm{T}}/2\pi = 0.25\,\mathrm{Hz}$, corresponding to a ground state size of $\sigma_{x,\mathrm{T}} \approx 40\,\mu\mathrm{m}$.

We thus combine a reasonable trap depth of $U_{0,\mathrm{T}}/k_{\mathrm{B}} = 50\,\mathrm{nK}$ (this corresponds to a molecular trap depth of 100 nK) with the required trap frequency of $\omega_{\mathrm{T}}/2\pi = 0.25\,\mathrm{Hz}$. The trap depth sets the scale for the temperature of the BEC and is on the order of the kinetic energy, $U_{0,\mathrm{T}}/E_{\mathrm{kin}} = 2.5$. By employing an elliptic laser beam with waist ratio $w_{x,\mathrm{T}}/w_{y,\mathrm{T}} = 10$, the required laser power can be kept reasonably low, at $P_{\mathrm{T}} = 13.1\mathrm{W}$, implying a longitudinal beam waist of $w_{0,\mathrm{T}} = 1.1\mathrm{cm}$. The corresponding photon scattering rate of $R_{\mathrm{T}} = 10^{-4}\mathrm{s}^{-1}$ does not impose any limitations, and the estimated number of bound states, $N_{\mathrm{b,T}} = 6650$, together with the validity of the harmonic approximation, $\sigma_{x,\mathrm{T}}/w_{0,\mathrm{T}} = 0.004 \ll 1$, justifies the existence of the Gaussian ground state $|\psi_{\mathrm{T}}\rangle$.

Summary Concluding, we have seen that an optical setup with ultracold atoms can provide the experimental frame for the conceived DTE and HRE scenarios. The possibility to extract usable DTE and HRE states with the desired relative velocity of $v_{\mathrm{rel}} = 1\mathrm{cm/s}$ will be shown in the Chapters 7 and 8.

Chapter 6

Feshbach dissociation dynamics

We know from Chapters 3 and 4 that appropriate descriptions of the DTE and HRE scenarios require a detailed knowledge of the underlying two-atom states. Let me remind the reader that the question whether the DTE or HRE Bell test is successful or not depends crucially on the ability to provide dissociation states with sufficiently peaked momentum distributions, since only then the resulting fringe patterns are usable. At this point, it is not yet clear whether the conceived Feshbach dissociation scheme can provide such states at all, or how one should choose the shape of the dissociation pulses in order to optimize the resulting momentum distributions. I therefore proceed to discuss in some detail the dissociation of a Feshbach molecule exposed to an externally controlled, time-varying magnetic field in the trap and guide setting presented in the last chapter.

More precisely, I develop the coupled-channel formalism required to determine the asymptotic (i.e. for large interatomic distances and times long after the dissociation process) dissociation state under these general conditions. Based on the then established relation between the applied magnetic field pulse and the resulting momentum distribution, we find that square-shaped magnetic field pulses optimize the spectrum with respect to its sharpness. The employment of sequences of such pulses to generate viable DTE and HRE states will be examined in the subsequent chapters.

So far, the theory of Feshbach molecules has mainly been concerned with an accurate description of the molecules in the bound regime and its vicinity, where the atoms interact strongly. For instance, the universal properties of the molecular state at constant magnetic field in the vicinity of a Feshbach resonance were investigated in great detail, as well as the association and dissociation behavior under a linear magnetic field sweep, with emphasis on the converted fraction (see [99–101] and Refs. therein). However, we are interested in the Feshbach dissociation state for a more general time behavior of the magnetic field. While in the interaction regime of the atoms one is then left with numerical methods [102], the restriction to the asymptotic situation comes with significant simplifications that permit us to evaluate the generated dissociation state analytically.

6.1 Coupled-channel formulation

The dynamics of Feshbach molecules are appropriately described by the coupled-channel approach. After a short introduction to Feshbach resonances, I formulate the time-dependent coupled-channel equations and reduce them to an integro-differential equation for the closed-channel amplitude and an associated equation for the background channel state. In the relevant case of the dissociation of a single molecule out of a dilute

mBEC, where interactions between the molecules and statistical effects do not play a role, these single molecule dynamics yield an adequate description of the experimental situation.

6.1.1 Feshbach resonances

Let us consider a system that consists of several degrees of freedom, say, its motional degree(s) of freedom and (discrete) internal degree(s) of freedom, such as spin. One speaks of a Feshbach resonance, when the bound motion of a given internal configuration decays by coupling to the unbound motion of another internal configuration into the continuum. This situation is appropriately formalized in a coupled-channel approach, where each internal configuration is assigned to a channel, and transitions between the different configurations are described by the coupling of the channels. The closed channel describes the bound configuration, and the background (open) channel the unbound one. The state $|\psi\rangle$ of the system can then be decomposed according to $|\psi\rangle = |\phi_{\rm cl}\rangle|{\rm cl}\rangle + |\phi_{\rm bg}\rangle|{\rm bg}\rangle$, and the Hamiltonian reads:

$$\begin{aligned} H_{\rm tot} &= H_{\rm cl}|{\rm cl}\rangle\langle{\rm cl}| + H_{\rm bg}|{\rm bg}\rangle\langle{\rm bg}| \\ &\quad + W|{\rm bg}\rangle\langle{\rm cl}| + W^\dagger|{\rm cl}\rangle\langle{\rm bg}|, \end{aligned} \tag{6.1}$$

where W denotes the coupling between the channels. A Feshbach resonance occurs, when the bare bound state $|\phi_{\rm res}\rangle$ of the closed channel, $H_{\rm cl}|\phi_{\rm res}\rangle = E_{\rm res}|\phi_{\rm res}\rangle$, is (nearly) degenerate with the continuum states of the background channel, see Fig. 6.1a). In general, there a more than two channels and several bound states in each channel, giving rise to a multitude of Feshbach resonances. However, we are only interested in a narrow energy range in the vicinity of the background channel dissociation threshold. It is then legitimate to restrict us to two channels, if the resonances are sufficiently well isolated.

In our case, the system consists of two alkali atoms, where the relevant players are the two nuclei (with nonvanishing spins) and the two valence electrons. Ultimately, we are interested in the motion of the nuclei, reflecting the dissociation of the atoms. The separation of the time scales of the electronic and the nuclear motion, which guarantees that the electrons adjust instantaneously to any change of the nuclear alignment, makes it possible to apply the Born-Oppenheimer approximation. There, the state of the two electrons is determined for given positions of the nuclei, which are considered as mere parameters. The resulting electronic energy (as a function of the positions of the nuclei) gives rise to an effective Schrödinger equation for the nuclei, where they move in an effective potential that is composed of the inter-nuclear interaction and the electronic energy.

Typically, the combined Coulomb interaction of the nuclei and the electrons yields a binding potential at small interatomic distances, its bound states corresponding to vibrations. For this, it is important to realize that the spatial wave function of the electrons is intimately correlated to their spin configuration, which is at small interatomic distances, where the spins interact strongly, given either by the singlet or a triplet state. In a triplet state, the spatial state component of the electrons has to be antisymmetric to guarantee an overall antisymmetric two-particle wave function, say, in first approximation $\left(|1s\rangle_A^1|1s\rangle_B^2 - |1s\rangle_B^1|1s\rangle_A^2\right)/\sqrt{2}$, which means that they avoid each other, thereby reducing their Coulomb repulsion. Here, $|1s\rangle_X^j$ denotes the the electronic ground state of the jth electron at the atom X. In contrast, if the spins form a singlet, the electrons do not avoid each other in the correspondingly symmetric spatial state $\left(|1s\rangle_A^1|1s\rangle_B^2 + |1s\rangle_B^1|1s\rangle_A^2\right)/\sqrt{2}$,

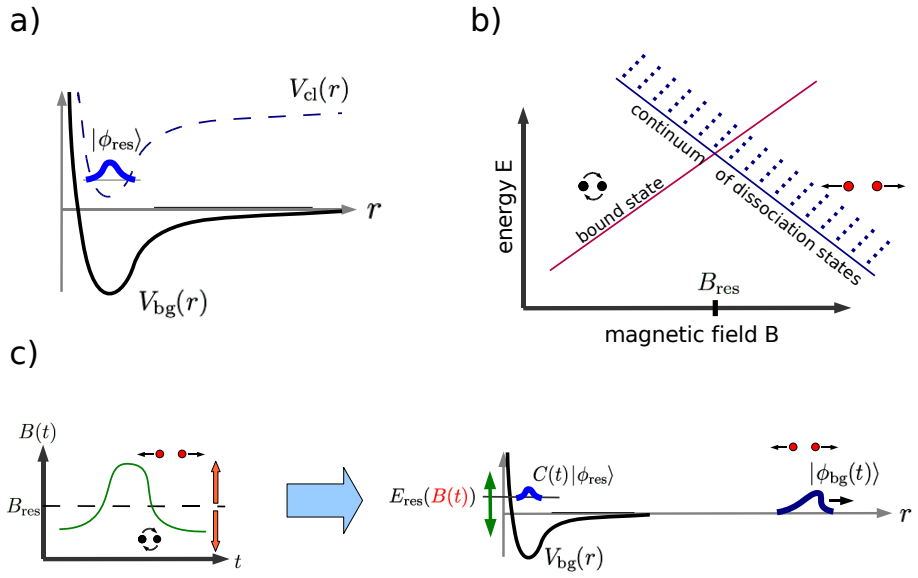

Figure 6.1: a) A Feshbach resonance emerges when a bound state of the (bare) closed-channel configuration, suitably labeled $|\phi_{\rm res}\rangle$, couples to the continuum of the background channel. b) By applying an external magnetic field, different Zeeman levels of two alkali atoms can be tuned such that a bound state of one configuration crosses the dissociation threshold of a second one, giving rise to a Feshbach resonance. c) A time-varying magnetic field $B(t)$ can be used to trigger the controlled dissociation of the closed-channel bound state $C(t)|\phi_{\rm res}\rangle$ into the background channel continuum. The resulting dissociation state $|\phi_{\rm bg}\rangle$ is then determined by the magnetic field pulse shape.

and the Coulomb repulsion generally reduces the depth of the inter-atomic potential as compared to the triplet potential.

In order to understand the occurrence of a Feshbach resonance, we must have a closer look at the spins of the valence electrons and the nuclei. When the atoms are far apart, they do not interact and the single-atom Hamiltonians include [103]

$$\frac{a_{\rm hf}}{\hbar^2}\vec{s}\cdot\vec{i}+\vec{B}\cdot\frac{2\mu_e\vec{s}-\mu_N\vec{i}}{\hbar}, \tag{6.2}$$

entailing the hyperfine interaction of the nuclear spin i and the electronic spin s and their coupling to an external magnetic field. In absence of the magnetic field, they couple to produce the hyperfine levels of total angular momentum $\vec{f}=\vec{s}+\vec{i}$, yielding the total angular momentum quantum number to be either $f=i-1/2$ or $i+1/2$. We take the quantum numbers $\{f_1,m_{f_1},f_2,m_{f_2}\}$ to specify the channels of the two-atom system.

When the atoms are nearby, the electron spins become uncoupled from the nuclear spin and couple strongly to one another. The corresponding interaction term $H_{ss}\propto\vec{s}_1\cdot\vec{s}_2$, which is diagonalized by the singlet and triplet states of the total electronic spin $S=s_1+s_2$, does not commute with the hyperfine interaction, hence giving rise to the coupling of different channels at small interatomic distances. Physically, the transition between the channels corresponds to spin flips of the nuclear and electronic spins of one

of the atoms. The dominance of H_{ss} in this region renders the singlet and triplet states valid approximations of the energy eigenstates there, coming with the above mentioned channel-dependent Born-Oppenheimer potentials.

Switching on a homogeneous magnetic field results in the Zeeman splitting of the levels corresponding to different m_f. This can be used to tune the energetic gap of different levels such that a bound motional state of one spin configuration, then referred to as closed channel, coincides with the dissociation threshold of a second configuration, the background channel, see Fig. 6.1b). The interchannel coupling at small distances then gives rise to a Feshbach resonance. Even more, the tunability of the resonance position gives us a handle to trigger the controlled dissociation of the bound state into the continuum. As depicted in Fig. 6.1c), depending on whether we tune the resonance below or above the background channel dissociation threshold, we can decide whether we wish the molecules to remain bound or to dissociate at a given energy. Note that in general the "closed channel" supporting the bound state does not coincide with a single channel according to our channel definition, but rather is represented by a superposition of several of them, which lie energetically close and all couple strongly to the background channel.

6.1.2 Stationary Feshbach scattering theory

Usually, when one talks about a Feshbach resonance, one has a (stationary) scattering situation in mind, where the existence of a quasibound state is reflected, e.g., in a resonance-enhanced scattering phase in the asymptotic wave function of the two colliding atoms. Let us assume that the magnetic field B is fixed at an appropriate value supporting a Feshbach resonance in the continuum of the background channel. The coupled-channel equations describing the stationary scattering states can be written as

$$(E - H_{\mathrm{bg}})|\phi_{\mathrm{bg}}\rangle = W|\phi_{\mathrm{cl}}\rangle \tag{6.3}$$

$$(E - H_{\mathrm{cl}})|\phi_{\mathrm{cl}}\rangle = W^{\dagger}|\phi_{\mathrm{bg}}\rangle. \tag{6.4}$$

For the moment, let us neglect the confining lasers. The center of mass motion and the relative motion then decouple and we can focus on the relative motion. In this case, the closed channel and the background channel Hamiltonian read

$$H_{\mathrm{cl}}(B) = -\frac{\hbar^2}{m}\vec{\nabla}^2_{\mathrm{rel}} + V_{\mathrm{cl}}(|\vec{x}_{\mathrm{rel}}|, B), \tag{6.5}$$

and

$$H_{\mathrm{bg}} = -\frac{\hbar^2}{m}\vec{\nabla}^2_{\mathrm{rel}} + V_{\mathrm{bg}}(|\vec{x}_{\mathrm{rel}}|), \tag{6.6}$$

respectively, where m denotes the atomic mass. The channel potentials $V_{\mathrm{cl}}(|\vec{x}_{\mathrm{rel}}|, B)$ and $V_{\mathrm{bg}}(|\vec{x}_{\mathrm{rel}}|)$ differ in general, reflecting the above mentioned dependence on the spin configuration. In compliance with [100], the background channel dissociation threshold defines the zero of energy, $E = 0$. Then only the closed-channel potential $V_{\mathrm{cl}}(|\vec{x}_{\mathrm{rel}}|, B)$ depends on the external magnetic field B, such that at $B = B_{\mathrm{res}}$ the closed-channel bound state $|\phi_{\mathrm{res}}\rangle$, $H_{\mathrm{cl}}(B)|\phi_{\mathrm{res}}\rangle = E_{\mathrm{res}}(B)|\phi_{\mathrm{res}}\rangle$, which gives rise to the resonance, coincides with the background channel dissociation threshold. The off-diagonal elements W denote the energies associated with the spin exchange interaction and provide the interchannel coupling. As usual, we assume W to be diagonal in position (i.e. independent of momentum) and to depend only on the interatomic distance $|\vec{x}_{\mathrm{rel}}|$ from now on, $W^*(|\vec{x}_{\mathrm{rel}}|) = W(|\vec{x}_{\mathrm{rel}}|)$ [100].

The coupled-channel equation (6.3) can formally be solved in terms of the background channel Green's function, which is defined according to $G_{\rm bg}(z) = (z - H_{\rm bg})^{-1}$. We choose the bare energy eigenstate $|\phi_{\vec{p}}^{(+)}\rangle$ with incoming plane wave boundary conditions as a homogeneous solution,

$$\langle \vec{x}_{\rm rel}|\phi_{\vec{p}}^{(+)}\rangle \underset{|\vec{x}_{\rm rel}|\to\infty}{\sim} \frac{1}{(2\pi\hbar)^{3/2}}\left[{\rm e}^{i\vec{p}\cdot\vec{x}_{\rm rel}/\hbar} + f_{\rm bg}(\vartheta,p)\frac{{\rm e}^{ip|\vec{x}_{\rm rel}|/\hbar}}{|\vec{x}_{\rm rel}|}\right], \tag{6.7}$$

where $(E - H_{\rm bg})|\phi_{\vec{p}}^{(+)}\rangle = 0$ and $E = \vec{p}^{\,2}/m$. The scattering amplitude $f_{\rm bg}(\vartheta,p)$ comprises the scattering at the background channel potential $V_{\rm bg}(|\vec{x}_{\rm rel}|)$ and depends on the scattering angle, which is determined by $\cos\vartheta = \vec{p}\cdot\vec{x}_{\rm rel}/(p|\vec{x}_{\rm rel}|)$. For the dressed background channel scattering state we then get

$$|\phi_{\rm bg}\rangle = |\phi_{\vec{p}}^{(+)}\rangle + G_{\rm bg}(E+i0)W|\phi_{\rm cl}\rangle, \tag{6.8}$$

where the infinitesimal positive imaginary part of the argument of the Green's function ensures that the scattered part is described by outgoing waves. Using this to replace $|\phi_{\rm bg}\rangle$ in (6.4) and noting $W = W^\dagger$, one obtains for the closed channel

$$|\phi_{\rm cl}\rangle = \frac{1}{E - H_{\rm cl} - WG_{\rm bg}(E+i0)W}W|\phi_{\vec{p}}^{(+)}\rangle. \tag{6.9}$$

This, in turn, can be substituted back into (6.8), yielding

$$|\phi_{\rm bg}\rangle = |\phi_{\vec{p}}^{(+)}\rangle + G_{\rm bg}(E+i0)W\frac{1}{E - H_{\rm cl} - WG_{\rm bg}(E+i0)W}W|\phi_{\vec{p}}^{(+)}\rangle. \tag{6.10}$$

We can already see at this stage that there should occur a resonance in the scattering. In order to make this transparent, one applies the single-resonance approximation, which replaces the inverse operator on the right-hand side by its dominant matrix element as given by the resonance state $|\phi_{\rm res}\rangle$,

$$\frac{1}{E - H_{\rm cl}(B) - WG_{\rm bg}(E+i0)W} \to |\phi_{\rm res}\rangle\frac{1}{E - E_{\rm res}(B) - \Delta E(E) + i\Gamma(E)/2}\langle\phi_{\rm res}|, \tag{6.11}$$

with the resonance width

$$\Gamma(E)/2 = -{\rm Im}\langle\phi_{\rm res}|WG_{\rm bg}(E+i0)W|\phi_{\rm res}\rangle \tag{6.12}$$

and the energy shift

$$\Delta E(E) = {\rm Re}\langle\phi_{\rm res}|WG_{\rm bg}(E+i0)W|\phi_{\rm res}\rangle. \tag{6.13}$$

This is possible, since we restrict us to energies in the vicinity of the background channel dissociation threshold, where $|\phi_{\rm res}\rangle$ is by assumption the only closed-channel eigenstate that is energetically close. The resonance width can be determined in terms of background channel energy eigenfunctions, $H_{\rm bg}|\varepsilon\rangle_{\rm bg} = \varepsilon|\varepsilon\rangle_{\rm bg}$,

$$\begin{aligned}\Gamma(E)/2 &= -{\rm Im}\sum_\varepsilon \frac{|\langle\phi_{\rm res}|W|\varepsilon\rangle|^2}{E - \varepsilon + i0} \\ &= \pi\sum_\varepsilon \delta(E-\varepsilon)|\langle\phi_{\rm res}|W|\varepsilon\rangle_{\rm bg}|^2.\end{aligned} \tag{6.14}$$

Specializing to the scattering states $|\phi_{\vec{p}}^{(+)}\rangle$, one obtains

$$\begin{aligned}\Gamma(E)/2 &= \pi \int \mathrm{d}^3p' \delta(E-p'^2/m)|\langle\phi_{\mathrm{res}}|W|\phi_{\vec{p}'}^{(+)}\rangle|^2 \\ &= 4\pi^2 mp|\langle\phi_{\mathrm{res}}|W|\phi_{\vec{p}}^{(+)}\rangle|^2 \\ &= \gamma(E)p/\hbar,\end{aligned}$$

where we used the rotational symmetry of the matrix element and introduced the reduced width

$$\gamma(E) = 4\pi^2 m\hbar|\langle\phi_{\mathrm{res}}|W|\phi_{\vec{p}}^{(+)}\rangle_{\mathrm{bg}}|^2. \tag{6.15}$$

Note that $\Gamma(E)$ vanishes at zero momentum. With (6.11), one obtains for the dressed background channel scattering state

$$|\phi_{\mathrm{bg}}\rangle = |\phi_{\vec{p}}^{(+)}\rangle + \frac{\langle\phi_{\mathrm{res}}|W|\phi_{\vec{p}}^{(+)}\rangle}{E-E_{\mathrm{res}}(B)-\Delta E(E)+i\Gamma(E)/2} G_{\mathrm{bg}}(E+i0)W|\phi_{\mathrm{res}}\rangle. \tag{6.16}$$

Similarly to (6.7), (6.16) can be written asymptotically as

$$\langle\vec{x}_{\mathrm{rel}}|\phi_{\mathrm{bg}}\rangle \underset{|\vec{x}_{\mathrm{rel}}|\to\infty}{\sim} \frac{1}{(2\pi\hbar)^{3/2}}\left[\mathrm{e}^{i\vec{p}\cdot\vec{x}_{\mathrm{rel}}/\hbar} + f(\vartheta,p)\frac{\mathrm{e}^{ip|\vec{x}_{\mathrm{rel}}|/\hbar}}{|\vec{x}_{\mathrm{rel}}|}\right]. \tag{6.17}$$

This time the scattering amplitude gets an additional contribution due to the coupling of the channels. From the asymptotic behavior of the Green's function,

$$\langle\vec{x}_{\mathrm{rel}}|G_{\mathrm{bg}}(z)|\vec{x}'_{\mathrm{rel}}\rangle \underset{|\vec{x}_{\mathrm{rel}}|\to\infty}{\sim} -\frac{m(2\pi\hbar)^3}{4\pi\hbar^2}\frac{\mathrm{e}^{ip|\vec{x}_{\mathrm{rel}}|/\hbar}}{|\vec{x}_{\mathrm{rel}}|}\left[\phi_{\vec{p}}^{(-)}(\vec{x}'_{\mathrm{rel}})\right]^*, \tag{6.18}$$

where $\phi_{\vec{p}}^{(-)}(\vec{x}'_{\mathrm{rel}}) = [\phi_{-\vec{p}}^{(+)}(\vec{x}'_{\mathrm{rel}})]^*$ is the background channel continuum energy state with incoming spherical wave boundary conditions [87], one derives [100]

$$\begin{aligned}f(\vartheta,p) &= f_{\mathrm{bg}}(\vartheta,p) - \frac{m(2\pi\hbar)^3}{4\pi\hbar^2}\frac{\langle\phi_{\mathrm{res}}|W|\phi_{\vec{p}}^{(+)}\rangle\langle\phi_{\vec{p}}^{(-)}|W|\phi_{\mathrm{res}}\rangle}{E-E_{\mathrm{res}}(B)-\Delta E(E)+i\Gamma(E)/2} \\ &= f_{\mathrm{bg}}(\vartheta,p) - \frac{\hbar}{2p}\frac{\Gamma(E)/2}{E-E_{\mathrm{res}}(B)-\Delta E(E)+i\Gamma(E)/2}.\end{aligned} \tag{6.19}$$

We find that the coupling between the channels gives rise to a Breit-Wigner resonance in the scattering characterized by its position at $E_{\mathrm{R}}(B) = E_{\mathrm{res}}(B) + \Delta E(E_{\mathrm{R}})$ and the resonance width $\Gamma(E_{\mathrm{R}})$. $\Gamma/\hbar$, in turn, describes the decay rate of the resonance state into the background channel continuum. In the limit of vanishing momentum the scattering amplitude reduces to the s-wave scattering length [87],

$$f(\vartheta,p) \underset{p\to0}{\sim} -a, \tag{6.20}$$

which yields in our case

$$a(B) = a_{\mathrm{bg}} - \frac{\gamma(0)/2}{E_{\mathrm{res}}(B)+\Delta E(0)}. \tag{6.21}$$

The degeneracy of a bound vibrational level with the scattering threshold is thus accompanied by a singularity of the s-wave scattering length. The scattering length describes the spatial displacement of a scattered wave packet due to the scattering source as compared to the free case.

6.1.3 Time-dependent coupled-channel equations

A proper treatment of the DTE and HRE scenarios must consider the time-dependent coupled-channel equations, which are now formulated. In doing so, I also account for the laser potentials, which is required for a complete and coherent description of the dissociation setting. As a novelty, I must therefore include the center of mass motion of the two atoms. Apart from that, the notation and the conventions from [100] are adopted as far as possible. Like in the previous section, we assume that the magnetic field remains always in the vicinity of a single Feshbach resonance, allowing us to restrict the description to two channels: the closed channel of the energetically more favorable spin configuration supporting the molecular bound state, and the background channel, where the dissociated atoms are asymptotically free.

Based on (6.1), the channel Hamiltonians now read as

$$\begin{aligned} H_{\mathrm{cl}} &= -\frac{\hbar^2}{2m}\vec{\nabla}_1^2 - \frac{\hbar^2}{2m}\vec{\nabla}_2^2 + V_{\mathrm{cl}}(|\vec{x}_1-\vec{x}_2|,B(t)) \\ &\quad + V_{\mathrm{T}}(\vec{x}_1) + V_{\mathrm{T}}(\vec{x}_2) + V_{\mathrm{G}}(\vec{x}_1) + V_{\mathrm{G}}(\vec{x}_2), \end{aligned} \tag{6.22}$$

and

$$\begin{aligned} H_{\mathrm{bg}} &= -\frac{\hbar^2}{2m}\vec{\nabla}_1^2 - \frac{\hbar^2}{2m}\vec{\nabla}_2^2 + V_{\mathrm{bg}}(|\vec{x}_1-\vec{x}_2|) \\ &\quad + V_{\mathrm{T}}(\vec{x}_1) + V_{\mathrm{T}}(\vec{x}_2) + V_{\mathrm{G}}(\vec{x}_1) + V_{\mathrm{G}}(\vec{x}_2). \end{aligned} \tag{6.23}$$

Here $V_{\mathrm{T}}(\vec{x}_i)$ and $V_{\mathrm{G}}(\vec{x}_i)$ denote the trapping and guiding laser potential, respectively (V_{G} may contain a linear shift due to the gravitational potential, as well). We keep the convention to define the zero of total energy in absence of the laser potentials by the background channel dissociation threshold, fixing the center of mass to be at rest. As before, then only the closed-channel potential $V_{\mathrm{cl}}(|\vec{x}_1-\vec{x}_2|,B(t))$ depends on the external magnetic field $B(t)$, describing an overall shift with respect to the background channel dissociation threshold. The off-diagonal elements W only affect the relative motion and thus remain unchanged.

For the following it is useful to reformulate the Hamiltonian in center of mass (cm) and relative (rel) coordinates, $\vec{x}_{\mathrm{cm}} = (\vec{x}_1+\vec{x}_2)/2$ and $\vec{x}_{\mathrm{rel}} = \vec{x}_1-\vec{x}_2$, respectively, with total mass $M = 2m$ and reduced mass $\mu = m/2$. The closed-channel Hamiltonian then reads as

$$\begin{aligned} H_{\mathrm{cl}} &= -\frac{\hbar^2}{2M}\vec{\nabla}_{\mathrm{cm}}^2 - \frac{\hbar^2}{2\mu}\vec{\nabla}_{\mathrm{rel}}^2 + V_{\mathrm{cl}}(|\vec{x}_{\mathrm{rel}}|,B(t)) \\ &\quad + V_{\mathrm{T}}(\vec{x}_{\mathrm{cm}}+\vec{x}_{\mathrm{rel}}/2) + V_{\mathrm{T}}(\vec{x}_{\mathrm{cm}}-\vec{x}_{\mathrm{rel}}/2) \\ &\quad + V_{\mathrm{G}}(\vec{x}_{\mathrm{cm}}+\vec{x}_{\mathrm{rel}}/2) + V_{\mathrm{G}}(\vec{x}_{\mathrm{cm}}-\vec{x}_{\mathrm{rel}}/2), \end{aligned} \tag{6.24}$$

and similar for H_{bg} with $V_{\mathrm{cl}}(|\vec{x}_{\mathrm{rel}}|,B(t))$ replaced by $V_{\mathrm{bg}}(|\vec{x}_{\mathrm{rel}}|)$. Note that the center of mass motion is only indirectly affected by changes in the homogeneous external magnetic field B, due to the presence of the trapping potentials. Writing

$$|\Psi_{\mathrm{tot}}(t)\rangle = \Phi_{\mathrm{cl}}(\vec{x}_{\mathrm{cm}},\vec{x}_{\mathrm{rel}},t)|\mathrm{cl}\rangle + \Phi_{\mathrm{bg}}(\vec{x}_{\mathrm{cm}},\vec{x}_{\mathrm{rel}},t)|\mathrm{bg}\rangle,$$

we can infer from the time-dependent Schrödinger equation the coupled channel equations

$$\begin{aligned} i\hbar\partial_t|\Phi_{\mathrm{cl}}(t)\rangle &= H_{\mathrm{cl}}(B(t))|\Phi_{\mathrm{cl}}(t)\rangle + W|\Phi_{\mathrm{bg}}(t)\rangle \\ i\hbar\partial_t|\Phi_{\mathrm{bg}}(t)\rangle &= H_{\mathrm{bg}}|\Phi_{\mathrm{bg}}(t)\rangle + W|\Phi_{\mathrm{cl}}(t)\rangle. \end{aligned} \tag{6.25}$$

It is reasonable to assume the transverse motion of the atoms to be constrained to the region of validity of the harmonic approximation of the guiding laser potential, and the harmonic approximation to be applicable also for the trap laser potential in the closed channel. We then can write (adopting cylindrical coordinates)

$$\begin{aligned} V_{\mathrm{G}}(\vec{x}_1)+V_{\mathrm{G}}(\vec{x}_2) &= -U_{0,\mathrm{G}}+\frac{m}{2}\omega_{\mathrm{G}}^2\rho_1^2-U_{0,\mathrm{G}}+\frac{m}{2}\omega_{\mathrm{G}}^2\rho_2^2 \\ V_{\mathrm{T}}(\vec{x}_1)+V_{\mathrm{T}}(\vec{x}_2) &= -U_{0,\mathrm{T}}+\frac{m}{2}\omega_{\mathrm{T}}^2 z_1^2-U_{0,\mathrm{T}}+\frac{m}{2}\omega_{\mathrm{T}}^2 z_2^2. \end{aligned} \tag{6.26}$$

The harmonic approximation comes with the virtue not to couple the center of mass and relative motion,

$$\begin{aligned} V_{\mathrm{G}}(\vec{x}_1)+V_{\mathrm{G}}(\vec{x}_2) &= -2U_{0,\mathrm{G}}+\frac{M}{2}\omega_{\mathrm{G}}^2\rho_{\mathrm{cm}}^2+\frac{\mu}{2}\omega_{\mathrm{G}}^2\rho_{\mathrm{rel}}^2 \\ V_{\mathrm{T}}(\vec{x}_1)+V_{\mathrm{T}}(\vec{x}_2) &= -2U_{0,\mathrm{T}}+\frac{M}{2}\omega_{\mathrm{T}}^2 z_{\mathrm{cm}}^2+\frac{\mu}{2}\omega_{\mathrm{T}}^2 z_{\mathrm{rel}}^2. \end{aligned} \tag{6.27}$$

The initial bound state can therefore be taken to be separable with respect to its center of mass and relative motion. Of course, the harmonic approximation for the trap laser potential breaks down when the dissociated atoms leave the trap. Then, the center of mass motion ceases to be bound by the trap potential but rather undergoes a free propagation resulting in a dispersive broadening on the spot. So, even though initially only the relative motion is affected by changes in the external magnetic field, its effective coupling in the background channel to the center of mass also couples the motion of the latter indirectly to the external magnetic field.

6.1.4 Single-resonance approximation

As in the stationary case, it is legitimate [100] to take the relative motion of the closed-channel state component to be proportional to the underlying bare resonance state $|\phi_{\mathrm{res}}\rangle$, which is defined by

$$\left[-\frac{\hbar^2}{2\mu}\vec{\nabla}_{\mathrm{rel}}^2+V_{\mathrm{cl}}(|\vec{x}_{\mathrm{rel}}|,B(t))\right]\phi_{\mathrm{res}}(\vec{x}_{\mathrm{rel}})=E_{\mathrm{res}}(B(t))\phi_{\mathrm{res}}(\vec{x}_{\mathrm{rel}}). \tag{6.28}$$

Note that the time-dependent external magnetic field affects only its energy, which is taken to vanish at the resonance, $E_{\mathrm{res}}(B_{\mathrm{res}})=0$, such that E_{res} describes the energetic offset of $|\phi_{\mathrm{res}}\rangle$ from the background channel dissociation threshold.

Since the laser potentials vary weakly over the extent of $|\phi_{\mathrm{res}}\rangle$, this resonance state remains a valid approximation even in the presence of the trap. We assume that $|\phi_{\mathrm{res}}\rangle$ is spherically symmetric and thus supports an s-wave resonance. If we further take into account that the center of mass motion of the closed channel is completely determined by the longitudinal and transversal trap ground states $|\psi_{\mathrm{T}}\rangle$ and $|\varphi_{0,0}^{\mathrm{cm}}\rangle$, respectively, we can write

$$\Phi_{\mathrm{cl}}(\vec{x}_{\mathrm{cm}},\vec{x}_{\mathrm{rel}},t)=C(t)\psi_{\mathrm{T}}(z_{\mathrm{cm}})\varphi_{0,0}^{\mathrm{cm}}(\rho_{\mathrm{cm}})\phi_{\mathrm{res}}(\vec{x}_{\mathrm{rel}}), \tag{6.29}$$

where

$$\begin{aligned} &[-\frac{\hbar^2}{2M}\vec{\nabla}_{\mathrm{cm}}^2+2V_{\mathrm{T}}(z_{\mathrm{cm}})+2V_{\mathrm{G}}(\rho_{\mathrm{cm}})]\psi_{\mathrm{T}}(z_{\mathrm{cm}})\varphi_{0,0}^{\mathrm{cm}}(\rho_{\mathrm{cm}}) \\ &\qquad =[-2U_{0,\mathrm{T}}+\hbar\omega_{\mathrm{T}}/2-2U_{0,\mathrm{G}}+\hbar\omega_{\mathrm{G}}]\psi_{\mathrm{T}}(z_{\mathrm{cm}})\varphi_{0,0}^{\mathrm{cm}}(\rho_{\mathrm{cm}}). \end{aligned} \tag{6.30}$$

In the single-resonance approximation (extended by the trapped center of mass motion) (6.29), the spatial shape of the closed channel state component is not affected by the external magnetic field and therefore time independent. The closed-channel amplitude $C(t)$ therefore captures the complete effect of the time-varying magnetic field. Using the single-resonance approximation (6.29) and introducing the abbreviation $U_{\mathrm{cl}} = -2U_{0,\mathrm{T}} + \hbar\omega_{\mathrm{T}}/2 - 2U_{0,\mathrm{G}} + \hbar\omega_{\mathrm{G}}$, we can thus rewrite the coupled-channel equations (6.25) as

$$i\hbar\partial_t C(t) = [E_{\mathrm{res}}(B(t)) + U_{\mathrm{cl}}]C(t) + \langle\psi_{\mathrm{T}}|\langle\varphi^{\mathrm{cm}}_{0,0}|\langle\phi_{\mathrm{res}}|W|\Phi_{\mathrm{bg}}(t)\rangle \tag{6.31}$$

$$(i\hbar\partial_t - H_{\mathrm{bg}})|\Phi_{\mathrm{bg}}(t)\rangle = C(t)W|\psi_{\mathrm{T}}\rangle|\varphi^{\mathrm{cm}}_{0,0}\rangle|\phi_{\mathrm{res}}\rangle. \tag{6.32}$$

6.1.5 Formal Green's solution

Mimicking the stationary approach, we interpret the right-hand side of (6.32) as a source term for the background channel state component $|\Phi_{\mathrm{bg}}(t)\rangle$. This time we must use the time-dependent Green's function of the background channel $G_{\mathrm{bg}}(t,t')$, which satisfies

$$(i\hbar\partial_t - H_{\mathrm{bg}})G_{\mathrm{bg}}(t,t') = \delta(t-t').$$

If we further make use of the connection between the (retarded) Green's function and the time evolution operator U_{bg},

$$G_{\mathrm{bg}}(t,t') = \frac{1}{i\hbar}U_{\mathrm{bg}}(t,t')\Theta(t-t'),$$

we can write the background channel state component as

$$|\Phi_{\mathrm{bg}}(t)\rangle = \frac{1}{i\hbar}\int_{-\infty}^{t} \mathrm{d}t' C(t')U_{\mathrm{bg}}(t,t')W|\psi_{\mathrm{T}}\rangle|\varphi^{\mathrm{cm}}_{0,0}\rangle|\phi_{\mathrm{res}}\rangle. \tag{6.33}$$

In our scenario, the boundary conditions prohibit a homogeneous solution. Physically, this reflects the fact that the closed channel is the only source for the background channel, in particular there are no further sources at infinity (e.g. incoming and scattered particles). A closed equation for the closed-channel amplitude $C(t)$ arises from inserting the formal solution (6.33) into (6.31), which yields

$$\begin{aligned}&[i\hbar\partial_t - E_{\mathrm{res}}(B(t)) - U_{\mathrm{cl}}]C(t) \\ &\quad= \frac{1}{i\hbar}\int_{-\infty}^{t}\mathrm{d}t' C(t')\langle\psi_{\mathrm{T}}|\langle\varphi^{\mathrm{cm}}_{0,0}|\langle\phi_{\mathrm{res}}|WU_{\mathrm{bg}}(t,t')W|\psi_{\mathrm{T}}\rangle|\varphi^{\mathrm{cm}}_{0,0}\rangle|\phi_{\mathrm{res}}\rangle.\end{aligned} \tag{6.34}$$

With (6.33) and (6.34) we arrived at a decoupled set of equations that divides the determination of the background channel dissociation state into two parts, first solving (6.34) for $C(t)$, and then using the solution in (6.33) for the calculation of $|\Phi_{\mathrm{bg}}\rangle$. The dynamics of the closed-channel amplitude $C(t)$ is explicitly driven by the external magnetic field $B(t)$, reflected in the left-hand side of (6.34). The bare background channel Hamiltonian H_{bg}, on the other hand, does not depend on the external magnetic field, which will allow us in Section 6.2 to expand the right-hand side of (6.33) in terms of its (time- and coupling-independent) energy eigenfunctions. The right hand side of (6.34) describes the back action of the background channel state component on the dynamics of $C(t)$ due to the coupling W. A solution to (6.34) will be given in Section 6.3.

As a last remark, I note that it might seem suggestive to first solve the time-independent coupled-channel equations for a stationary magnetic field B, and then to take the corresponding static decay rate to describe the dissociation in the time-dependent case $B(t)$, as it was done in [32]. However, we will see below that this quasi-stationary approach is not sufficient for our purposes.

6.2 Asymptotic dissociation state

The formal expression (6.33) describes the background channel state component in full generality. In the DTE and HRE scenarios, however, we only need to know the dissociation state for large interatomic distances and for times long after the dissociation process. Moreover, the relevant dissociation states are sharply peaked in the ultracold regime, in the sense that the width of the momentum distribution is much smaller than its average momentum, because only then are they useful with respect to further interferometric processing. The above restrictions admit significant simplifications that permit us to provide an analytic expression for the dissociation state in the asymptotic regime.

6.2.1 Large time limit

As a first step, we expand the background channel time evolution operator $U_{\mathrm{bg}}(t,t')$ in an appropriate energy eigenbasis of the background channel Hamiltonian.

$$U_{\mathrm{bg}}(t,t') = \mathrm{e}^{-iH_{\mathrm{bg}}(t-t')} = \sum_E \mathrm{e}^{-iE(t-t')/\hbar}|E\rangle_{\mathrm{bg}}\langle E|_{\mathrm{bg}}, \tag{6.35}$$

where $H_{\mathrm{bg}}|E\rangle_{\mathrm{bg}} = E|E\rangle_{\mathrm{bg}}$; adequate quantum numbers for our setup will be specified below. Note that the involved vectors are two-particle states. As mentioned above, this representation is only possible for the bare background Hamiltonian, which does not depend on the external magnetic field. Since at large interatomic distances only the continuum states survive, we can drop the bound states in (6.33) for large $|\vec{x}_{\mathrm{rel}}|$ and get

$$\begin{aligned}\langle \vec{x}_{\mathrm{cm}}, \vec{x}_{\mathrm{rel}}|\Phi_{\mathrm{bg}}(t)\rangle \quad \underset{|\vec{x}_{\mathrm{rel}}|\to\infty}{\sim} \quad & \frac{1}{i\hbar}\sum_{E>U_{\mathrm{bg}}}\int_{-\infty}^{t}\mathrm{d}t' C(t')\mathrm{e}^{-iE(t-t')/\hbar}\langle E|_{\mathrm{bg}}W|\psi_{\mathrm{T}}\rangle|\varphi_{0,0}^{\mathrm{cm}}\rangle|\phi_{\mathrm{res}}\rangle \\ & \times\langle \vec{x}_{\mathrm{cm}}, \vec{x}_{\mathrm{rel}}|E\rangle_{\mathrm{bg}}.\end{aligned} \tag{6.36}$$

The sum over the energy eigenstates takes into account that the zero of energy is defined in absence of the confining lasers, whose presence shifts the (longitudinal) continuum threshold by an offset $U_{\mathrm{bg}} = -2U_{0,\mathrm{G}} + 2\hbar\omega_{\mathrm{G}}$. We arrange the dissociation such that after its completion the magnetic field persists at a base value B_0 below the dissociation threshold. The closed-channel amplitude then shows a simple time dependence in the large time regime, $C(t) = C_0\exp(-iE_0t/\hbar)$, such that for times long after the completion we can replace the upper integration boundary by infinity without modifying the value of the integral for energies above the dissociation threshold. This allows us to interpret the integration over t' as the Fourier transform $\tilde{C}(\omega) = \int_{-\infty}^{\infty}\mathrm{d}t\exp(i\omega t)C(t)$ of the closed-channel amplitude $C(t)$, yielding

$$\begin{aligned}\langle \vec{x}_{\mathrm{cm}}, \vec{x}_{\mathrm{rel}}|\Phi_{\mathrm{bg}}(t)\rangle \quad \underset{\substack{|\vec{x}_{\mathrm{rel}}|\to\infty \\ t\to\infty}}{\approx} \quad & \frac{1}{i\hbar}\sum_{E>U_{\mathrm{bg}}}\mathrm{e}^{-iEt/\hbar}\tilde{C}(E/\hbar)\langle E|_{\mathrm{bg}}W|\psi_{\mathrm{T}}\rangle|\varphi_{0,0}^{\mathrm{cm}}\rangle|\phi_{\mathrm{res}}\rangle \\ & \times\langle \vec{x}_{\mathrm{cm}}, \vec{x}_{\mathrm{rel}}|E\rangle_{\mathrm{bg}}.\end{aligned} \tag{6.37}$$

We thus find that the asymptotic dissociation state can be interpreted as evolving in the background channel with the initial state in energy representation given by $\tilde{C}(E/\hbar)\times\langle E|_{\mathrm{bg}}W|\psi_{\mathrm{T}}\rangle|\varphi_{0,0}^{\mathrm{cm}}\rangle|\phi_{\mathrm{res}}\rangle$. We will see that this expression describes two counter-propagating atoms with well-defined momenta if $\tilde{C}(\omega)$ is peaked at an energy in the ultracold regime. The corresponding wave functions then have de Broglie wavelengths and spatial extensions on the order of micro- to millimeters, all being features desired for applications such as the DTE and HRE Bell tests.

6.2.2 Quantum numbers

Note that the energy eigenvalues in (6.35) are highly degenerate; in order to single out a unique energy basis, we choose as asymptotically well-defined, commuting observables the complete set $\hat{p}_{\rm cm}$, $\hat{p}_{\rm rel}$ and $H_\perp$, where $H_\perp$ denotes the transversal Hamiltonian. Assuming harmonic transversal confinement, we can write

$$\begin{aligned}\sum_{E>U_{\rm bg}} |E\rangle_{\rm bg}\langle E|_{\rm bg} \quad &= \quad \sum_{\substack{n_{\rm G}^{\rm cm},m_{\rm G}^{\rm cm}\\ n_{\rm G}^{\rm rel},m_{\rm G}^{\rm rel}}} \int_{-\infty}^{\infty} {\rm d}p_{\rm cm} \int_{-\infty}^{\infty} {\rm d}p_{\rm rel} |p_{\rm cm},n_{\rm G}^{\rm cm},m_{\rm G}^{\rm cm},p_{\rm rel},n_{\rm G}^{\rm rel},m_{\rm G}^{\rm rel}\rangle_{\rm bg} \\ &\quad \times \langle p_{\rm cm},n_{\rm G}^{\rm cm},m_{\rm G}^{\rm cm},p_{\rm rel},n_{\rm G}^{\rm rel},m_{\rm G}^{\rm rel}|_{\rm bg}. \end{aligned} \tag{6.38}$$

Here $n_{\rm G} = 0,1,\ldots$ denotes the radial occupation number and $m_{\rm G} = -n_{\rm G},\ldots,n_{\rm G}$ the corresponding angular momentum quantum number. Since we assume that $W|\phi_{\rm res}\rangle$ is spherically symmetric (s-wave resonance), $W|\psi_{\rm T}\rangle|\varphi_{0,0}^{\rm cm}\rangle|\phi_{\rm res}\rangle$ is both cylindrically symmetric and symmetric under exchange of the two particles, hence only the states $|p_{\rm cm},n,0,p_{\rm rel},n,0\rangle$ sharing these symmetries can be occupied.

If we take $\tilde{C}(E/\hbar)$ to be peaked at a sufficently low energy and if the laser guide is chosen appropriately, we can ensure that only the transversal ground state is energetically accessible. In this single-mode regime we have

$$\begin{aligned}&\langle \vec{x}_{\rm cm},\vec{x}_{\rm rel}|\Phi_{\rm bg}(t)\rangle \\ &\underset{\substack{|\vec{x}_{\rm rel}|\to\infty\\ t\to\infty}}{\approx} \frac{1}{i\hbar}\int_{-\infty}^{\infty}{\rm d}p_{\rm cm}\int_{-\infty}^{\infty}{\rm d}p_{\rm rel}\,{\rm e}^{-i(U_{\rm bg}+p_{\rm cm}^2/2M+p_{\rm rel}^2/2\mu)t/\hbar}\,\tilde{C}\left(\frac{U_{\rm bg}+p_{\rm cm}^2/2M+p_{\rm rel}^2/2\mu}{\hbar}\right) \\ &\qquad \times \langle p_{\rm cm},0,0,p_{\rm rel},0,0|_{\rm bg} W|\psi_{\rm T}\rangle|\varphi_{0,0}^{\rm cm}\rangle|\phi_{\rm res}\rangle\langle \vec{x}_{\rm cm},\vec{x}_{\rm rel}|p_{\rm cm},0,0,p_{\rm rel},0,0\rangle_{\rm bg}. \end{aligned} \tag{6.39}$$

Even if taking $\tilde{C}(E/\hbar)$ to be sharply peaked in energy, it still admits the whole class of degenerate eigenstates that fall into that energetic region. As I show next, the matrix element $\langle p_{\rm cm},0,0,p_{\rm rel},0,0|_{\rm bg} W|\psi_{\rm T}\rangle|\varphi_{0,0}^{\rm cm}\rangle|\phi_{\rm res}\rangle$ effects a further restriction of the accessible eigenstates, yielding the physically appropriate description of the situation.

6.2.3 Asymptotic center of mass motion

The main effect of the longitudinal trap is to correlate the motion of the interatomic distance with the center of mass, since the center of mass evolution is confined for small interatomic distances, while it is free for distances beyond the size of the trap. For a sufficiently peaked energy distribution this merely results in a global time delay for the start of the free center of mass propagation, which may be neglected at the time scales of the asymptotic regime. The longitudinal center of mass motion can thus be described by the momentum eigenstates $|p_{\rm cm}\rangle$, that is by

$$|p_{\rm cm},0,0,p_{\rm rel},0,0\rangle_{\rm bg} \approx |p_{\rm cm}\rangle|\varphi_{0,0}^{\rm cm}\rangle|p_{\rm rel},0,0\rangle_{\rm bg}.$$

Here $|p_{\rm rel},0,0\rangle_{\rm bg}$ denotes the eigenstates of the Hamiltonian for the relative motion, which still contains the traps and the interatomic potential $V_{\rm bg}$. The dissociation state

then reads

$$\begin{aligned}
&\langle \vec{x}_{\rm cm}, \vec{x}_{\rm rel}|\Phi_{\rm bg}(t)\rangle \\
&\underset{\substack{|\vec{x}_{\rm rel}|\to\infty \\ t\to\infty}}{\approx} \frac{1}{i\hbar}\int_{-\infty}^{\infty}{\rm d}p_{\rm cm}\int_{-\infty}^{\infty}{\rm d}p_{\rm rel}{\rm e}^{-i(U_{\rm bg}+p_{\rm cm}^2/2M+p_{\rm rel}^2/2\mu)t/\hbar}\tilde{C}\left(\frac{U_{\rm bg}+p_{\rm cm}^2/2M+p_{\rm rel}^2/2\mu}{\hbar}\right) \\
&\qquad\times\langle p_{\rm cm}|\psi_{\rm T}\rangle\langle p_{\rm rel},0,0|_{\rm bg}W|\phi_{\rm res}\rangle\langle z_{\rm cm}|p_{\rm cm}\rangle\langle\rho_{\rm cm}|\varphi_{0,0}^{\rm cm}\rangle\langle\vec{x}_{\rm rel}|p_{\rm rel},0,0\rangle_{\rm bg}. \qquad (6.40)
\end{aligned}$$

The matrix element $\langle p_{\rm cm}|\psi_{\rm T}\rangle$, given by the longitudinal harmonic trap ground state of the center of mass motion in momentum representation, guarantees that the center of mass motion remains centered at vanishing momentum, as required by momentum conservation in the dissociation process. Since we take the energy to be in the ultracold regime of the background channel potential $V_{\rm bg}$, the matrix element $\langle p_{\rm rel},0,0|_{\rm bg}W|\phi_{\rm res}\rangle$ is practically constant and does not impose any further structure on the momentum distribution of the dissociation state.

6.2.4 Connection to spectroscopy

I now give an estimate of the matrix element $\langle p_{\rm rel},0,0|_{\rm bg}W|\phi_{\rm res}\rangle$ in terms of spectroscopically available quantities such as the width of the Feshbach resonance and the background channel scattering length. A natural basis of energy eigenstates is provided by the scattering states $|\phi_{\vec{p}}^{(+)}\rangle$, where $[\hat{p}_{\rm rel}^2/2\mu+V_{\rm bg}(r)]|\phi_{\vec{p}}^{(+)}\rangle = p^2/(2\mu)|\phi_{\vec{p}}^{(+)}\rangle$ [100]. It describes the scattering in the relative motion *in absence* of the confining laser potentials, with an incoming plane wave with momentum $\vec{p}$ as boundary condition.

In order to relate $\langle p_{\rm rel},0,0|W|\phi_{\rm res}\rangle$ to the spectroscopically available matrix element $\langle\phi_{\vec{p}}^{(+)}|W|\phi_{\rm res}\rangle$, we note that the spatial extension of the longitudinal trap is much larger than the support of the channel coupling $W|\phi_{\rm res}\rangle$. This scale separation permits one to approximate the effect of the longitudinal trap by a mere energy shift,

$$\langle p_{\rm rel},0,0|_{\rm bg}W|\phi_{\rm res}\rangle \approx \langle p_{\rm rel}+p_{\rm T},0,0|_{\rm w/oT}W|\phi_{\rm res}\rangle, \qquad (6.41)$$

where $|p_{\rm rel},0,0\rangle_{\rm w/oT}$ denotes the background channel energy eigenstates of the relative motion *without* the trap potential (without loss of generality $p_{\rm rel}>0$). The momentum shift $p_{\rm T}$ is related to the trap depth by $U_{0,\rm T}=p_{\rm T}^2/2\mu$. Inserting the identity in terms of the basis $|\phi_{\vec{p}}^{(+)}\rangle$, we can rewrite the matrix element as

$$\langle p_{\rm rel}+p_{\rm T},0,0|_{\rm w/oT}W|\phi_{\rm res}\rangle = \int{\rm d}^3p\langle p_{\rm rel}+p_{\rm T},0,0|_{\rm w/oT}\phi_{\vec{p}}^{(+)}\rangle\langle\phi_{\vec{p}}^{(+)}|W|\phi_{\rm res}\rangle. \qquad (6.42)$$

The matrix element $\langle p_{\rm rel}+p_{\rm T},0,0|_{\rm w/oT}\phi_{\vec{p}}^{(+)}\rangle$ can be evaluated for a vanishing background channel potential, $V_{\rm bg}(r)\equiv 0$, since the scattering due to $V_{\rm bg}$ should not result in a substantial modification of the overlap. We thus have

$$\begin{aligned}
\langle p_{\rm rel}+p_{\rm T},0,0|_{\rm w/oT}\phi_{\vec{p}}^{(+)}\rangle &\approx \langle p_{\rm rel}+p_{\rm T}|p_z\rangle\langle\varphi_{0,0}^{\rm rel}|p_x\rangle|p_y\rangle \qquad (6.43)\\
&= \delta(p_{\rm rel}+p_{\rm T}-p_z)\frac{1}{\sqrt{\hbar\omega_{\rm G}\mu\pi}}{\rm e}^{-(p_x^2+p_y^2)/2\mu\hbar\omega_{\rm G}}.
\end{aligned}$$

Insertion into (6.42) yields $\langle p_{\rm rel}+p_{\rm T},0,0|_{\rm w/oT}W|\phi_{\rm res}\rangle \approx \sqrt{4\pi\mu\hbar\omega_{\rm G}}\langle\phi_0^{(+)}|W|\phi_{\rm res}\rangle$, where we use that $p_{\rm rel}+p_{\rm T}$ still lies in the ultracold regime such that $W|\phi_{\rm res}\rangle$ cannot be resolved

and hence $\langle\phi_{\vec{p}}^{(+)}|W|\phi_{\rm res}\rangle \cong \langle\phi_0^{(+)}|W|\phi_{\rm res}\rangle$. This is justified given that $p_{\rm rel}$ is mainly determined by $\tilde{C}$. With (6.41) we thus obtain the desired connection to the spectroscopically availabe quantity $\langle\phi_0^{(+)}|W|\phi_{\rm res}\rangle$,

$$\langle p_{\rm rel},0,0|_{\rm bg} W|\phi_{\rm res}\rangle \approx \sqrt{4\pi\mu\hbar\omega_{\rm G}}\langle\phi_0^{(+)}|W|\phi_{\rm res}\rangle. \tag{6.44}$$

According to stationary Feshbach scattering theory [100]

$$|\langle\phi_0^{(+)}|W|\phi_{\rm res}\rangle|^2 = \frac{4\pi\hbar^2}{m(2\pi\hbar)^3}\, a_{\rm bg}\,\mu_{\rm res}\,\Delta B_{\rm res}, \tag{6.45}$$

with $a_{\rm bg}$ being the background channel scattering length, $\Delta B_{\rm res}$ the resonance width, and $\mu_{\rm res}$ the difference between the magnetic moments of the Feshbach resonance state and a pair of asymptotically separated noninteracting atoms. (6.45) follows directly from (6.15) and (6.21) if one identifies the resonance width with $\Delta B_{\rm res} = \gamma(0)/(2\,a_{\rm bg}\mu_{\rm res})$.

6.2.5 Asymptotic relative motion

Finally, let us approximate the basis states $|p_{\rm rel},0,0\rangle_{\rm bg}$ in the asymptotic regime $z_{\rm rel}\to\infty$, where the scattering states differ from the longitudinally free energy eigenstates only in a scattering phase $\varphi_{\rm sc}(p_{\rm rel})$,

$$\langle\vec{x}_{\rm rel}|p_{\rm rel},0,0\rangle_{\rm bg} \underset{z_{\rm rel}\to\infty}{\sim} \mathrm{e}^{i\varphi_{\rm sc}(p_{\rm rel})}\langle z_{\rm rel}|p_{\rm rel}\rangle\langle\rho_{\rm rel}|\varphi_{0,0}^{\rm rel}\rangle. \tag{6.46}$$

The phase $\varphi_{\rm sc}(p_{\rm rel})$ has two contributions, stemming from $V_{\rm bg}$ and $V_{\rm T}$. Since we are in the ultracold regime of $V_{\rm bg}$, its contribution is a linear shift given by the background channel scattering length $a_{\rm bg}$. The contribution from $V_{\rm T}$, on the other hand, can be linearized due to our requirement that the energy be sharply peaked, because the width of the energy distribution is then small compared to the characteristic energy scale of the trap potential. The latter is determined by the trap depth $U_{0,\rm T}$ and is thus on the same order of magnitude as the kinetic energy after dissociation. This situation is similar to the scattering of a narrow wave packet with spread ΔE at a broad resonance with width Γ, $\Delta E \ll \Gamma$ [87]. Confinement-induced resonances [104] due to the guide potential are negligible provided the ground state size $a_\perp = (\hbar/m\omega_{\rm G})^{1/2}$ greatly exceeds the background channel scattering lenght, $a_\perp \gg a_{\rm bg}$.

As described by a linear scattering phase, the potentials thus merely effect an overall spatial displacement of the generated dissociation state. Physically, this shift stems from the faster propagation of the particles in the trap region. Since we are mainly interested in the structure of the generated dissociation state, we can safely neglect this displacement and approximate

$$\langle\vec{x}_{\rm rel}|p_{\rm rel},0,0\rangle_{\rm bg} \underset{z_{\rm rel}\to\infty}{\approx} \langle z_{\rm rel}|p_{\rm rel}\rangle\langle\rho_{\rm rel}|\varphi_{0,0}^{\rm rel}\rangle. \tag{6.47}$$

6.2.6 Canonical dissociation state

Putting this all together, the asymptotic dissociation state reads as

$$\begin{aligned}\langle\vec{x}_{\rm cm},\vec{x}_{\rm rel}|\Phi_{\rm bg}(t)\rangle \underset{\substack{|\vec{x}_{\rm rel}|\to\infty\\ t\to\infty}}{\approx} & \frac{1}{i\hbar}\sqrt{4\pi\mu\hbar\omega_{\rm G}}\langle\phi_0^{(+)}|W|\phi_{\rm res}\rangle\int_{-\infty}^{\infty}\mathrm{d}p_{\rm cm}\int_{-\infty}^{\infty}\mathrm{d}p_{\rm rel} \\ & \times \mathrm{e}^{-i(U_{\rm bg}+p_{\rm cm}^2/2M+p_{\rm rel}^2/2\mu)t/\hbar}\tilde{C}\left(\frac{U_{\rm bg}+p_{\rm cm}^2/2M+p_{\rm rel}^2/2\mu}{\hbar}\right)\langle p_{\rm cm}|\psi_{\rm T}\rangle \\ & \times \langle z_{\rm cm}|p_{\rm cm}\rangle\langle\rho_{\rm cm}|\varphi_{0,0}^{\rm cm}\rangle\langle z_{\rm rel}|p_{\rm rel}\rangle\langle\rho_{\rm rel}|\varphi_{0,0}^{\rm rel}\rangle.\end{aligned} \tag{6.48}$$

Normalizing the spectrum with

$$\|\tilde{C}\|^2 = \int_{-\infty}^{\infty} \mathrm{d}p_{\mathrm{cm}} \int_{-\infty}^{\infty} \mathrm{d}p_{\mathrm{rel}} |\tilde{C}\left(U_{\mathrm{bg}}/\hbar + p_{\mathrm{cm}}^2/2M\hbar + p_{\mathrm{rel}}^2/2\mu\hbar\right)|^2 |\langle p_{\mathrm{cm}}|\psi_{\mathrm{T}}\rangle|^2 \quad (6.49)$$

and introducing the abbreviation

$$C_{\mathrm{bg}} = \frac{1}{i\hbar}\sqrt{4\pi\mu\hbar\omega_{\mathrm{G}}}\langle\phi_0^{(+)}|W|\phi_{\mathrm{res}}\rangle\|\tilde{C}\|, \quad (6.50)$$

we can express the dissociation state in canonical form,

$$|\Phi_{\mathrm{bg}}(t)\rangle \underset{\substack{|\vec{x}_{\mathrm{rel}}|\to\infty \\ t\to\infty}}{\approx} C_{\mathrm{bg}} U_{z,t}^{(0)} |\Psi_z\rangle |\varphi_{0,0}^{\mathrm{cm}}\rangle |\varphi_{0,0}^{\mathrm{rel}}\rangle. \quad (6.51)$$

Here $U_{z,t}^{(0)} = \exp[-i(\hat{p}_{\mathrm{cm}}^2/2M + \hat{p}_{\mathrm{rel}}^2/2\mu + U_{\mathrm{bg}})t/\hbar]$ is the free longitudinal time evolution operator, and the longitudinal state component $|\psi_z\rangle$ is defined by the momentum representation

$$\langle p_{\mathrm{cm}}|\langle p_{\mathrm{rel}}|\Psi_z\rangle = \frac{\tilde{C}\left(U_{\mathrm{bg}}/\hbar + p_{\mathrm{cm}}^2/2M\hbar + p_{\mathrm{rel}}^2/2\mu\hbar\right)}{\|\tilde{C}\|}\langle p_{\mathrm{cm}}|\psi_{\mathrm{T}}\rangle. \quad (6.52)$$

The dissociation probability is given by $|C_{\mathrm{bg}}|^2$, which can be expressed in terms of the above mentioned spectroscopic quantities using (6.45),

$$|C_{\mathrm{bg}}|^2 = \frac{\omega_{\mathrm{G}} a_{\mathrm{bg}} \mu_{\mathrm{res}} \Delta B_{\mathrm{res}}}{\pi\hbar^2}\|\tilde{C}\|^2. \quad (6.53)$$

It is mainly controlled by the applied magnetic field pulse which determines $\|\tilde{C}\|^2$. We now focus on choices of the resonance width ΔB_{res} and the magnetic field pulse such that the dissociation probability is on the order of a few percent.

Taking Eqs. (6.51), (6.52) and (6.53) together, we have found the desired expression for the asymptotic dissociation state. It is characterized by the trap geometry and, most importantly, by the Fourier transform of the closed-channel amplitude $\tilde{C}(\omega)$, which is in turn determined by the applied magnetic field pulse sequence. In order to answer what kind of states can be generated, we thus have to determine the dynamics of the closed channel amplitude $C(t)$.

6.3 Closed-channel amplitude dynamics

In the previous section we found that the momentum representation (6.52) of the asymptotic dissociation state is mainly determined by the Fourier transform $\tilde{C}(\omega)$ of the closed-channel amplitude. In order to determine the generated state for a given magnetic field pulse sequence, we thus have to determine the dynamics of the closed-channel amplitude $C(t)$ as determined by equation (6.34).

6.3.1 Separation of decay and driving dynamics

Let me rewrite the integral equation (6.34) as

$$[i\hbar\partial_t - E_{\mathrm{res}}(B(t)) - U_{\mathrm{cl}}]\,C(t) = \int_{-\infty}^{t} \mathrm{d}t' f(t-t')C(t'), \quad (6.54)$$

with the kernel

$$\begin{aligned} f(\tau) &= \frac{1}{i\hbar}\langle\psi_{\mathrm{T}}|\langle\varphi_{0,0}^{\mathrm{cm}}|\langle\phi_{\mathrm{res}}|WU_{\mathrm{bg}}(\tau)W|\psi_{\mathrm{T}}\rangle|\varphi_{0,0}^{\mathrm{cm}}\rangle|\phi_{\mathrm{res}}\rangle \\ &= \frac{1}{i\hbar}\sum_E \mathrm{e}^{-iE\tau/\hbar}|\langle E|_{\mathrm{bg}}W|\psi_{\mathrm{T}}\rangle|\varphi_{0,0}^{\mathrm{cm}}\rangle|\phi_{\mathrm{res}}\rangle|^2, \end{aligned} \tag{6.55}$$

where we used the decomposition of the background channel time evolution operator (6.35). The right-hand side of Eq. (6.54) describes the effect of the coupling between the channels on the closed-channel amplitude. It is quadratic in the interchannel coupling W and hence, for a weak coupling and sufficiently short dissociation windows, its effect is expected to yield a small correction to the unperturbed dynamics given by the left-hand side. Physically, we expect it to describe the decay of the closed-channel amplitude due to the escaping wave packet in the background channel. The kernel (6.55) may be viewed as the time-dependent overlap between the "initial state" $W|\psi_{\mathrm{T}}\rangle|\varphi_{0,0}^{\mathrm{cm}}\rangle|\phi_{\mathrm{res}}\rangle$ and its evolved version $U_{\mathrm{bg}}(\tau)W|\psi_{\mathrm{T}}\rangle|\varphi_{0,0}^{\mathrm{cm}}\rangle|\phi_{\mathrm{res}}\rangle$, which vanishes at large times due to the propagation in the background channel. It does not depend on the external magnetic field $B(t)$.

The kernel (6.55) is expected to drop off on a microscopic ("memory") time scale t_{m}, which can be roughly estimated from the spatial width Δx of the closed-channel bound state $|\phi_{\mathrm{res}}\rangle$. Denoting the corresponding momentum uncertainty by Δp, one obtains the drop-off time scale $t_{\mathrm{m}} = m\Delta x^2/\hbar$ from $\Delta p\, t_{\mathrm{m}}/m = \Delta x$ and the uncertainty relation. The spatial width of the closed-channel bound state $|\phi_{\mathrm{res}}\rangle$ is on the order of the closed-channel scattering length, with typical values on the order of $\Delta x \approx 100\, a_0$. Taking the mass of lithium atoms (^{6}Li) one thus gets the estimate $t_{\mathrm{m}} \approx 10\,\mathrm{ns}$, which should be compared to the inverse decay rate of the resonance, which is much greater in our case. Given this shortness of t_{m}, one might consider taking the limit $t_{\mathrm{m}} \to 0$, which is equivalent to setting $f(\tau) \propto \delta(\tau)$, but it will become clear below that this approximation is too crude and cannot even qualitatively account for the correct decay behavior.

In order to separate the anticipated decay from the unitary dynamics due to the left-hand side, we switch over to a "comoving frame" defined by

$$C(t) = C_0(t)D(t), \tag{6.56}$$

where the uncoupled closed-channel amplitude $C_0(t)$ follows by definition from

$$[i\hbar\partial_t - E_{\mathrm{res}}(B(t)) - U_{\mathrm{cl}}]\,C_0(t) = 0, \tag{6.57}$$

which implies

$$C_0(t) = C_0(t_0)\exp\left(-i\int_{t_0}^{t} \mathrm{d}t'[E_{\mathrm{res}}(B(t')) + U_{\mathrm{cl}}]/\hbar\right). \tag{6.58}$$

Applying the ansatz (6.56) on (6.54) and using (6.57) and (6.58), one finds that the evolution of the coupling dynamics is governed by

$$i\hbar\partial_t D(t) = \int_{-\infty}^{t} \mathrm{d}t' D(t') f(t-t') \exp\left(i\int_{t'}^{t} \mathrm{d}t''[E_{\mathrm{res}}(B(t'')) + U_{\mathrm{cl}}]/\hbar\right). \tag{6.59}$$

Since $D(t)$ is driven only by the coupling between the two channels, we expect it to vary slowly for sufficiently small interchannel coupling W, such that it can be considered

constant to good approximation on the time scale t_m of nonvanishing kernel $f(t-t')$. This allows us to pull $D(t)$ out of the integral, leading to

$$\partial_t D(t) = \alpha(t) D(t),$$

with the (in general complex) coupling coefficient

$$\alpha(t) = \frac{1}{i\hbar}\int_{-\infty}^{t} \mathrm{d}t' f(t-t') \exp\left(i \int_{t'}^{t} \mathrm{d}t'' [E_\mathrm{res}(B(t'')) + U_\mathrm{cl}]/\hbar \right). \tag{6.60}$$

By writing

$$\alpha(t) = -\Gamma(t)/2 - i\Delta E(t)/\hbar, \tag{6.61}$$

we make explicit that the real and imaginary parts of $\alpha(t)$ describe the decay rate $\Gamma(t)$ and an energy shift $\Delta E(t)$, respectively, as induced by the coupling between the two channels. Below, we will see that they coincide with their stationary counterparts (6.13) and (6.14) in the appropriate limit.

6.3.2 Decay dynamics

One can evaluate the coupling coefficient (6.60) further in the case of sufficiently smooth steering of the magnetic field, such that the resonance energy varies slowly on the scale of the drop-off time t_m,

$$\frac{\mathrm{d}}{\mathrm{d}t} E_\mathrm{res}(t)\, t_\mathrm{m} \ll \frac{\hbar}{t_\mathrm{m}}. \tag{6.62}$$

In the vicinity of the resonance B_res one can linearize,

$$E_\mathrm{res}(t) = \mu_\mathrm{res}(B(t) - B_\mathrm{res}), \tag{6.63}$$

leading to

$$\frac{\mathrm{d}}{\mathrm{d}t} B(t) \ll \frac{\hbar}{t_\mathrm{m}^2 \mu_\mathrm{res}}. \tag{6.64}$$

This assumption allows one to approximate the integral in the exponent of (6.60) as

$$\int_{t'}^{t} \mathrm{d}t'' [E_\mathrm{res}(B(t'')) + U_\mathrm{cl}]/\hbar \approx [E_\mathrm{res}(B(t)) + U_\mathrm{cl}](t-t')/\hbar. \tag{6.65}$$

Using (6.65) we can rewrite the coupling coefficient (6.60) as

$$\alpha(t) = \frac{1}{i\hbar}\int_{-\infty}^{\infty} \mathrm{d}t' \Theta(t-t') f(t-t')\, \mathrm{e}^{i[E_\mathrm{res}(B(t)) + U_\mathrm{cl}](t-t')/\hbar}. \tag{6.66}$$

This can be read as the Fourier transform of the product of $f(\tau)$ and the Heaviside step function $\Theta(\tau)$, implying

$$\alpha(t) = -\frac{i}{2\hbar}\tilde{f}\left(\frac{E_\mathrm{res}(B(t)) + U_\mathrm{cl}}{\hbar}\right) + \frac{1}{2\pi\hbar}\mathscr{P}\int_{-\infty}^{\infty} \frac{\mathrm{d}\omega}{\omega}\, \tilde{f}\left(\frac{E_\mathrm{res}(B(t)) + U_\mathrm{cl}}{\hbar} - \omega\right), \tag{6.67}$$

where $\mathscr{P}$ denotes the Cauchy principal value. Making use of (6.55), the Fourier transform $\tilde{f}(\omega) = \int_{-\infty}^{\infty} \mathrm{d}t\, \mathrm{e}^{i\omega t} f(t)$ of the kernel reads

$$\tilde{f}(\omega) = \frac{2\pi}{i\hbar}\sum_E \delta(\omega - E/\hbar) |\langle E|_\mathrm{bg} W |\psi_\mathrm{T}\rangle |\varphi_{0,0}^\mathrm{cm}\rangle |\phi_\mathrm{res}\rangle|^2. \tag{6.68}$$

We thus find the decay rate according to (6.61) to be given by

$$\Gamma(t) = \frac{2\pi}{\hbar} \sum_E \delta\left(E_{\rm res}(B(t)) + U_{\rm cl} - E\right) |\langle E|_{\rm bg} W |\psi_{\rm T}\rangle |\varphi^{\rm cm}_{0,0}\rangle |\phi_{\rm res}\rangle|^2, \tag{6.69}$$

and the coupling-induced energy shift by

$$\Delta E(t) = \sum_E \mathscr{P}\left(\frac{1}{E_{\rm res}(B(t)) + U_{\rm cl} - E}\right) |\langle E|_{\rm bg} W |\psi_{\rm T}\rangle |\varphi^{\rm cm}_{0,0}\rangle |\phi_{\rm res}\rangle|^2. \tag{6.70}$$

Equation (6.69) shows that a nonvanishing decay rate is obtained only when $E_{\rm res}(t) + U_{\rm cl}$ matches a background channel energy eigenvalue. In particular, the gap in the spectrum between the dissociation threshold and the highest excited bound state explains why decay occurs only when the resonance energy lingers above the continuum threshold. (We always stay off-tuned from bound states of $V_{\rm bg}$.) This also explains why the naive approximation for the kernel, $f(\tau) \approx f_0\,\delta(\tau)$, is not applicable; since the Fourier transform of $\delta(\tau)$ is constant, it cannot distinguish energies above and below the continuum threshold and thus predicts an unphysical decay below the threshold.

Note that (6.69), which coincides with the decay rate (6.14) of the corresponding Feshbach resonance in the stationary scattering situation for constant magnetic field,[1] may also be viewed as a generalized version of Fermi's Golden rule, where the decay rate is determined by the *instantaneous* resonance energy $E_{\rm res}(B(t))$, which in turn is externally controlled via the magnetic field $B(t)$. This coincidence is not accidental, of course, since the limit of a slowly varying magnetic field (6.64) admits both interpretations. The condition (6.64) quantifies the applicability of this approximation.

Let me now use the results of the preceding section by specifying the energy eigenbasis according to (6.38). Assuming again that the resonance state energy $E_{\rm res}(B(t))$ only sweeps over energies in the vicinity of the background channel continuum threshold, remaining in the ultracold energy regime, below the first excited transversal state and off-tuned from the highest excited bound state of $V_{\rm bg}$, we can write

$$\begin{aligned} \Delta E(t) \;&=\; |\langle p_{\rm rel} = 0, n^{\rm rel}_{\rm G} = 0, m^{\rm rel}_{\rm G} = 0|_{\rm bg} W |\phi_{\rm res}\rangle|^2 \int_{-\infty}^{\infty} {\rm d}p_{\rm cm} \int_{-\infty}^{\infty} {\rm d}p_{\rm rel} \\ &\quad \times \mathscr{P}\left(\frac{1}{E_{\rm res}(B(t)) + U_{\rm cl} - U_{\rm bg} - p^2_{\rm cm}/2M - p^2_{\rm rel}/2\mu}\right) |\langle p_{\rm cm}|\psi_{\rm T}\rangle|^2 \end{aligned} \tag{6.71}$$

and

$$\begin{aligned} \Gamma(t) \;&=\; \frac{2\pi}{\hbar} |\langle p_{\rm rel} = 0, n^{\rm rel}_{\rm G} = 0, m^{\rm rel}_{\rm G} = 0|_{\rm bg} W |\phi_{\rm res}\rangle|^2 \int_{-\infty}^{\infty} {\rm d}p_{\rm cm} \int_{-\infty}^{\infty} {\rm d}p_{\rm rel} \\ &\quad \times \delta(E_{\rm res}(B(t)) + U_{\rm cl} - U_{\rm bg} - p^2_{\rm cm}/2M - p^2_{\rm rel}/2\mu) |\langle p_{\rm cm}|\psi_{\rm T}\rangle|^2. \end{aligned} \tag{6.72}$$

I have omitted transitions into bound states of the longitudinal trap; they are negligible given the pulse sweeps sufficiently fast over the corresponding energies. Moreover, one can arrange the dissociation pulse $B(t)$ such that the offset of the resonance state energy from the background channel continuum threshold greatly exceeds the trap state momentum uncertainty $\sigma_{p,\rm T}$ for most of the time, $E_{\rm res}(B(t)) + U_{\rm cl} - U_{\rm bg} \gg \sigma^2_{p,\rm T}/2M$. In that case the integrals are dominated by $p_{\rm rel} \gg p_{\rm cm}$, and we can evaluate them with the approximation

$$|\langle p_{\rm cm}|\psi_{\rm T}\rangle|^2 \approx \delta(p_{\rm cm}). \tag{6.73}$$

[1] Up to a factor $\hbar$, which translates between the decay width with dimension of an energy and the decay rate with dimension of a frequency.

This yields a vanishing energy shift, $\Delta E(t) = 0$, since the principal value integration cancels. For the decay rate, on the other hand, we find

$$\begin{aligned}\Gamma(t) &= \frac{2\omega_{\rm G} a_{\rm bg}\mu_{\rm res}\Delta B_{\rm res}}{\hbar}\sqrt{\frac{2\mu}{E_{\rm res}(B(t)) - 2U_{0,\rm T} + \hbar\omega_{\rm T}/2 - \hbar\omega_{\rm G}}} \\ &\quad \times\Theta(E_{\rm res}(B(t)) - 2U_{0,\rm T} + \hbar\omega_{\rm T}/2 - \hbar\omega_{\rm G}),\end{aligned} \tag{6.74}$$

where we substituted $|\langle p_{\rm rel} = 0, n_{\rm G}^{\rm rel} = 0, m_{\rm G}^{\rm rel} = 0|_{\rm bg} W|\phi_{\rm res}\rangle|^2 = \omega_{\rm G} a_{\rm bg}\mu_{\rm res}\Delta B_{\rm res}/\pi$, as well as $U_{\rm bg} = -2U_{0,\rm G} + 2\hbar\omega_{\rm G}$ and $U_{\rm cl} = -2U_{0,\rm T} + \hbar\omega_{\rm T}/2 - 2U_{0,\rm G} + \hbar\omega_{\rm G}$. As expected, we find that the decay rate (6.74) is nonvanishing only for magnetic field values that lift the resonance state above the (longitudinal) background channel continuum threshold. The offset $-2U_{0,\rm T} + \hbar\omega_{\rm T}/2 - \hbar\omega_{\rm G}$ in the step function gives the energy to be provided in addition to the free dissociation threshold. There, the trap depth to be overcome by both atoms is reduced by the closed-channel center of mass ground state energy $\hbar\omega_{\rm T}/2$, while the transversal relative motion, tightly bound in the closed channel, must make the transition to the transversal ground state of the guide. The square root pole stems from the one-dimensional density of state and does not lead to appreciable effects as long as the pulse sweeps sufficiently fast over it.

In summary, we find, under appropriate conditions concerning the dissociation pulse, that the decay dynamics of the closed-channel amplitude is described by

$$\partial_t D(t) = -\frac{\Gamma(t)}{2} D(t), \tag{6.75}$$

with the decay rate $\Gamma(t)$ given by (6.74). Noting the formal solution

$$D(t) = D(t_0)\exp\left(-\int_{t_0}^{t} {\rm d}t'\Gamma(t')/2\right), \tag{6.76}$$

the overall closed-channel amplitude $C(t)$ then follows from $C(t) = C_0(t)D(t)$, with the uncoupled closed-channel amplitude $C_0(t)$ given by (6.58). For the asymptotic dissociation state as described in Section 6.2 we ultimately need to know the Fourier transform of the closed-channel amplitude, which is given by the convolution of the Fourier transforms of $C_0(t)$ and $D(t)$,

$$\tilde{C}(\omega) = \frac{1}{2\pi}\int_{-\infty}^{\infty} {\rm d}\bar{\omega}\tilde{C}_0(\bar{\omega})\tilde{D}(\omega - \bar{\omega}). \tag{6.77}$$

In the limiting case of strong interchannel coupling or long-lasting, slowly varying dissociation pulses, the kinetic energy distribution of the dissociated atoms, denoted by $n(E)$, is determined by the decay dynamics $D(t)$ alone. In this quasi-stationary situation one may take the dissociation to occur monoenergetically, at the momentary resonance energy, by writing $n(E)\,{\rm d}E = \Gamma(t)\,|D(t)|^2\,{\rm d}t$. For a monotonically increasing pulse energy $E_{\rm res}(t)$ the inverse $t(E)$ exists (defining $\dot{E}_{\rm res}(E) = \partial_t E_{\rm res}(t(E))$), and also the decay rate (6.74) can be viewed as a function of energy. Since $D(t)$ decays exponentially it then follows that the energy distribution is given by

$$n(E) = -\frac{\rm d}{{\rm d}E}\exp\left(-\int_{E_0}^{E}\frac{\Gamma(E')}{\dot{E}_{\rm res}(E')}{\rm d}E'\right). \tag{6.78}$$

This kind of quasi-stationary approach was used in [32] for the case of a linear field sweep, $\dot{E}_{\rm res} = {\rm const}$, and the above formula is consistent with their treatment when evaluated in absence of confining lasers.

On the other hand, in the case of a sudden magnetic field jump to a constant value $B_0 + \Delta B$ above the threshold (which can be considered a square-shaped pulse in the limit of infinite pulse duration), the Fourier transform $\tilde{C}_0(\omega)$ gets sharply peaked at $E_{\rm res}(B_0 + \Delta B)$, as will be shown below. The function $\tilde{C}(\omega)$ then reduces to $\tilde{C}(\omega) \approx \tilde{D}(\omega - E_{\rm res}(B_0 + \Delta B)/\hbar)$, with $\tilde{D}(\omega)$ a Lorentzian according to $D(t) \propto \exp(-\Gamma(E_{\rm res}(B_0 + \Delta B))t/2)$, which recovers the corresponding situation in [99].

However, in the following we are interested in the case where a magnetic field pulse dissociates on average only a single molecule out of the BEC. This implies that the decay of $D(t)$ can be neglected compared to the dynamics of $C_0(t)$, such that the Fourier transform $\tilde{C}(\omega)$ is essentially given by $\tilde{C}_0(\omega)$. I will therefore focus on the uncoupled closed-channel amplitude $C_0(t)$, from now on, and in particular on magnetic field pulses that result in a sharply peaked momentum distribution, as required for interferometric purposes. The following section is devoted to magnetic field pulses that optimize $\tilde{C}_0(\omega)$ with that respect. Equation (6.77) shows that any non-negligible decay of the closed channel amplitude then merely results in an undesired smearing of the spectrum.

6.4 Optimal magnetic field pulse

Having established that the asymptotic dissociation state is essentially determined by the Fourier transform of the closed-channel amplitude $C(t)$, whose dynamics were analyzed in the previous section, we proceed to characterize the magnetic field pulse shape that is optimal in terms of providing wave packets with well-defined momentum. To this end, we can restrict to the case of a single dissociation pulse. The generalization to sequences of pulses is straightforward, essentially yielding their superpositions. A detailed elaboration of a sequence of two dissociation pulses will be given in the following chapter. In addition, as explained above, we may confine ourselves to the case of negligible depletion of the BEC, where the closed-channel amplitude $C(t)$ is well approximated by the uncoupled component $C_0(t)$, whose dynamics is given by (6.57) and (6.58).

6.4.1 Dimensionless formulation

We start by switching to a more convenient representation. Since the resonance state energy $E_{\rm res}(B(t))$ is proportional to the magnetic field $B(t)$ in the vicinity of the Feshbach resonance, see (6.63), it is sufficient to investigate the dependence on $E_{\rm res}(B(t))$. We rewrite the integrand in the exponent of (6.58) as

$$E_{\rm res}(B(t)) + U_{\rm cl} = E_0 + \Delta E P(t/T), \tag{6.79}$$

where $P(t/T)$ describes a pulse with unit height; E_0 denotes the base value, and ΔE and T characterize the height and the width of the pulse, respectively. Introducing the dimensionless energy $\varepsilon = \Delta E T/\hbar$ and the phase function

$$\phi(t/T) = \int_{t_0/T}^{t/T} \mathrm{d}\tilde{t} P(\tilde{t}) + \phi_0, \tag{6.80}$$

we can write the Fourier transform of $C_0(t)$ as

$$\frac{\mathrm{e}^{-iE_0 t_0/\hbar}}{C_0(t_0)} \tilde{C}_0(\omega + E_0/\hbar) = \int_{-\infty}^{\infty} \mathrm{d}t \mathrm{e}^{i\omega t} \mathrm{e}^{-i\varepsilon\phi(t/T)}. \tag{6.81}$$

Given the pulse function $P(\tilde{t})$ is positive and has a compact support, the phase function $\phi(t)$ undergoes a monotonic ascent interpolating between two constant levels. If the pulse is also symmetric, $P(-\tilde{t}) = P(\tilde{t})$, the constant of integration ϕ_0 can be chosen such that the phase function $\phi(t)$ is antisymmetric, $\phi(-t) = -\phi(t)$. The constant prefactor on the left-hand side of (6.81) is irrelevant and will be neglected from now on.

6.4.2 Gaussian magnetic field pulse

We now ask for phase functions $\phi(t)$ that yield a well-behaved spectrum $\tilde{C}_0(\omega)$. A natural starting point is to consider the spectrum resulting from a Gaussian-shaped pulse function $P(\tilde{t})$. In this case, as for most other pulses, the integral on the right-hand side of (6.81) cannot be calculated exactly. But asymptotic expansion techniques can be applied if we take the dimensionless energy ε to be large, $\varepsilon \gg 1$. This is a justified assumption in realistic scenarios. An estimate with $\mu_{\mathrm{res}} \approx 10^{-2}\mu_{\mathrm{B}}$, $\Delta B = 100\mathrm{mG}$ (where $B(t) = B_0 + \Delta B P(t/T)$) and $T = 100\mathrm{ms}$ yields $\varepsilon = 10^3$.

The Gaussian pulse leads to the error function,

$$\phi(\tilde{t}) = \mathrm{erf}(\tilde{t}),$$

whose analyticity admits a uniform asymptotic expansion [105], which is capable of handling stationary points both lying on the real axis and in the complex plane. Neglecting the irrelevant prefactor on the left hand side of (6.81), the result reads

$$\frac{\tilde{C}_0(\omega + E_0/\hbar)}{T} = 2\pi i \frac{a_0}{\varepsilon^{1/3}} \mathrm{Ai}(\varepsilon^{2/3}\gamma^2), \tag{6.82}$$

with the coefficients

$$\gamma = \begin{cases} i\left(\frac{3}{2}\left[\mathrm{erf}(\alpha) - \frac{\omega T}{\varepsilon}\alpha\right]\right)^{1/3} & , \frac{\omega T}{\varepsilon} < \frac{2}{\sqrt{\pi}} \\ -\left(\frac{3}{2}\left[\frac{\omega T}{\varepsilon}\alpha - \mathrm{erfi}(\alpha)\right]\right)^{1/3} & , \frac{\omega T}{\varepsilon} > \frac{2}{\sqrt{\pi}} \end{cases}, \tag{6.83}$$

and

$$a_0 = \begin{cases} -i\frac{\left(\frac{3}{2}[\mathrm{erf}(\alpha) - \omega T\alpha/\varepsilon]\right)^{1/6}}{(\omega T\alpha/\varepsilon)^{1/2}} & , \frac{\omega T}{\varepsilon} < \frac{2}{\sqrt{\pi}} \\ -i\frac{\left(\frac{3}{2}[\omega T\alpha/\varepsilon - \mathrm{erfi}(\alpha)]\right)^{1/6}}{(\omega T\alpha/\varepsilon)^{1/2}} & , \frac{\omega T}{\varepsilon} > \frac{2}{\sqrt{\pi}} \end{cases}, \tag{6.84}$$

where

$$\alpha = \begin{cases} \sqrt{-\ln\left(\frac{\sqrt{\pi}}{2}\frac{\omega T}{\varepsilon}\right)} & , \frac{\omega T}{\varepsilon} < \frac{2}{\sqrt{\pi}} \\ \sqrt{\ln\left(\frac{\sqrt{\pi}}{2}\frac{\omega T}{\varepsilon}\right)} & , \frac{\omega T}{\varepsilon} > \frac{2}{\sqrt{\pi}} \end{cases}. \tag{6.85}$$

A brief derivation of (6.82) is given in Appendix A.4. Numerical analysis verifies excellent agreement with the exact result for large ε. Figure 6.2 shows a plot of the corresponding spectrum for $\varepsilon = 100$. It clearly does not exhibit a well-behaved peak structure, but rather shows contributions from all energies covered by the pulse sweep. The oscillating structure can be understood as due to the interference between the contributions from the ascending and the descending slope of the pulse.

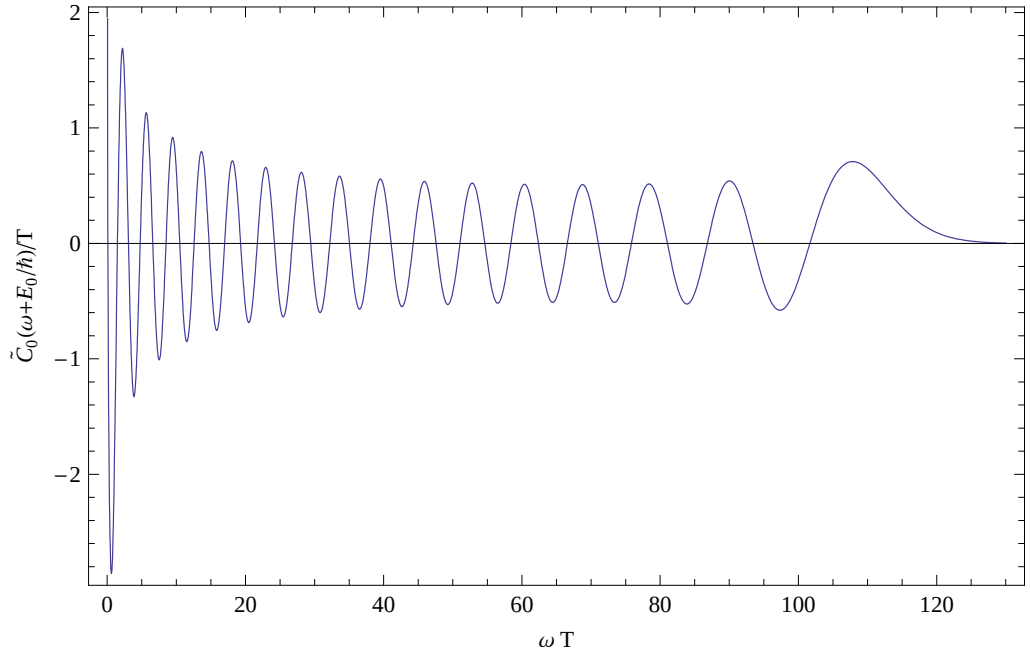

Figure 6.2: Fourier transform $\tilde{C}_0(\omega)$ of the uncoupled closed-channel amplitude, here evaluated for a Gaussian magnetic field pulse with the dimensionless energy $\varepsilon = 100$. In the plot the numerically exact result is indistinguishable from the asymptotic evaluation as given by Eq. (6.82). As described in Section 6.2, $\tilde{C}_0(\omega)$ essentially determines the momentum distribution of the asymptotic dissociation state, see Eq. (6.52). One observes that the spectrum does not exhibit a narrow peak-structure as one would require for atoms propagating with well-defined momenta. Rather, the spectrum exhibits contributions from all energies the pulse sweeps over. The oscillations stem from the interference between the contributions of the ascending and the descending slope of the pulse.

6.4.3 Square-shaped magnetic field pulse

A clearer and more general insight into the relation between the pulse and the corresponding spectrum can be obtained by retreating to the stationary phase approximation. This comes at the cost of losing the spectrum in the tail region where the stationary points of the exponent in (6.81) leave the real axis. On the other hand, also nonanalytic functions can now be treated. For the sake of simplicity, we consider symmetric pulses, $P(-\tilde{t}) = P(\tilde{t})$. In stationary phase approximation, we then get from (6.81)

$$\frac{\tilde{C}_0(\omega + E_0/\hbar)}{T} = \sqrt{\frac{8\pi}{\varepsilon |P'(\tilde{t}_\omega)|}} \cos\left[\omega T \tilde{t}_\omega - \varepsilon\phi(\tilde{t}_\omega) + \frac{\pi}{4}\right], \text{ for } \omega T/\varepsilon < \phi''_{\max}, \quad (6.86)$$

where $\tilde{t}_\omega$ denotes the positive (dimensionless) stationary point, which is implicitly defined by $\phi'(\tilde{t}_\omega) = \omega T/\varepsilon$. A brief derivation of (6.86) can be found in Appendix A.3. Since $\tilde{t}_\omega$ corresponds to the instant at which the pulse sweeps over the frequency ω, it is manifest from (6.86) that the corresponding contribution to the spectrum is the more suppressed the faster the pulse sweeps over the corresponding energy, as one expects physically.

Aiming at a spectrum that is well-peaked at a specific energy, we thus must strive for magnetic field pulses that sweep as fast as possible over the region of undesired energies

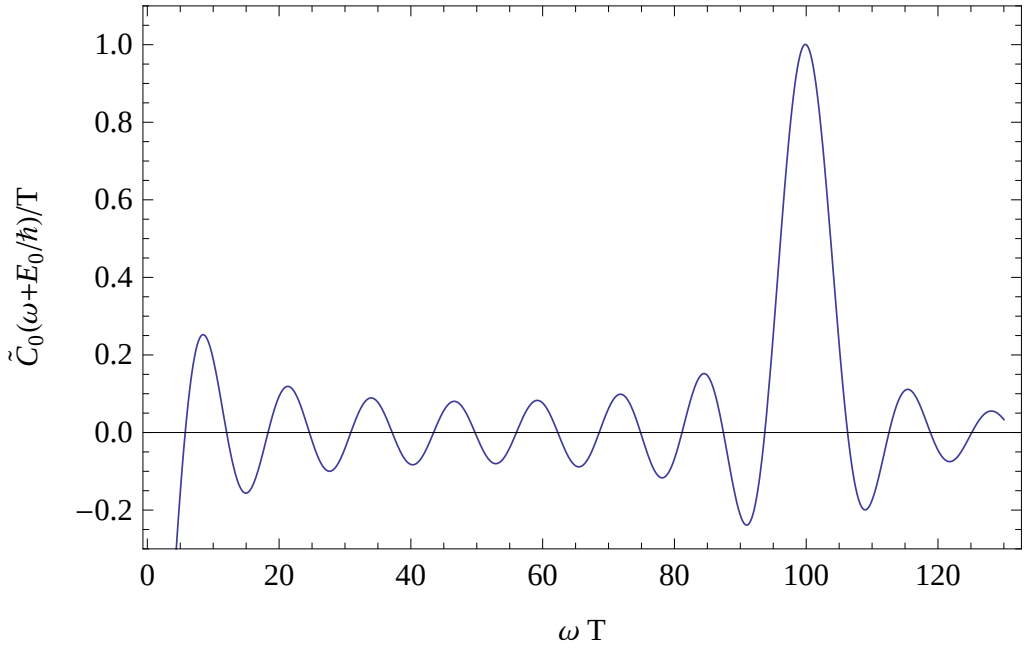

Figure 6.3: Fourier transform $\tilde{C}_0(\omega)$ of the uncoupled closed-channel amplitude component for a square-shaped magnetic field pulse with dimensionless energy $\varepsilon = 100$. In contrast to the Gaussian pulse spectrum, it exhibits a pronounced peak at $\omega T = \varepsilon$. Together with the connection (6.52) between $\tilde{C}(\omega)$ and the asymptotic dissociation state, this proves the capability of the scheme to provide relatively well-defined atom momenta, even though there is no way to tailor arbitrary dissociation states. In particular, sequences of such pulses then can serve to generate highly nonclassical motionally entangled states. (Since $E_0 < 0$ the pole at $\omega T = 0$ does not affect the asymptotic behavior of the atoms.)

and then rest at a plateau determined by the desired energy. The (idealized) optimal pulse with that respect is a square-shaped pulse,

$$P(\tilde{t}) = \Theta(\tilde{t}+1/2)\Theta(\tilde{t}-1/2), \tag{6.87}$$

for which (6.81) can be calculated directly, yielding

$$\frac{\tilde{C}_0(\omega+E_0/\hbar)}{T} = 2\pi\cos\left(\frac{\varepsilon}{2}\right)\delta(\omega T) + \mathrm{sinc}\left(\frac{\omega T-\varepsilon}{2}\right)\mathscr{P}\left(\frac{\varepsilon}{\omega T}\right). \tag{6.88}$$

The pole at $\omega T = 0$ can be traced back to the fact that the pulse function (6.87) is nonvanishing only on a finite time interval. For $E_0 < 0$, which corresponds to an asymptotic magnetic field in the bound regime, this pole lies at a negative energy irrelevant for the shape of the dissociation state, as was shown in Section 6.2. For our purposes it is thus legitimate to restrict the discussion to positive frequencies with $\omega + E_0/\hbar > 0$. A plot of (6.88) for $\varepsilon = 100$ is shown in Figure 6.3. As anticipated, the spectrum exhibits a pronounced peak at $\omega T = \varepsilon$, whose width is characterized by the pulse duration T. According to (6.52), the corresponding dissociation state therefore exhibits a narrow momentum distribution, which renders it useful for the implementation of DTE and HRE states.

Discussion

This concludes the search for the optimal magnetic field pulse shape. As indicated in the stationary phase calculation (6.86), by sweeping as fast as possible over undesired energies one singles out a momentum distribution peaked at the desired energy. This has been verified numerically for a large variety of pulse forms. (Idealized) square-shaped pulses thus optimize the spectrum with respect to its sharpness. In particular, it is now clear that smoothening the edges of the square shape inevitably enhances the undesired ripples in the region of the energies swept over, contradicting the naive expectation that they stem from the nondifferentiable ansatz (6.87) for the pulse.

More generally, we found that the nature of Feshbach dissociation dynamics puts strong limitations on the possible range of states that can be generated. It is in general not possible to find a pulse shape so as to generate a specified dissociation state. On the other hand, as was demonstrated in [35] and will be elaborated in the following chapters, the combination of a sequence of two dissociation pulses yields a promising perspective to generate highly nonclassical motionally entangled two-atom states–the DTE and HRE states–with the capacity to violate a Bell inequality.

Chapter 7

Dissociation-time entanglement in the Feshbach scenario

We have now all at hand to complete the description of the DTE scenario and to see whether a Bell violation is possible or not in the Feshbach dissociation scheme. In Chapter 5 I outlined the geometry of the experimental setup, and in the previous chapter the asymptotic form of the Feshbach-induced dissociation state was derived within this setting. Based on this preliminary work, I proceed to specialize to a double square-pulse dissociation state and determine the corresponding two-particle momentum distribution. After describing a possible implementation of the subsequent Mach-Zehnder interferometers, I determine the corresponding DTE fringe pattern based on the general results in Chapter 3. For an appropriate choice of parameters, the possibility of a Bell violation can be answered affirmatively.

7.1 Extraction of a DTE atom pair

Let me briefly recapitulate the course of the DTE scenario. Starting from a BEC of diatomic Feshbach molecules, which resides in an optical dipole trap, a sequence of two short magnetic field pulses dissociates a single atom pair, such that each atom is delocalized into two consecutive, macroscopically distinct wave packets, as depicted in Figure 7.1 a). The atoms propagate along the laser guide, where subsequent switched Mach-Zehnder interferometers serve to rejoin the early and the late wave packets on each side; the resulting interference in the output ports gives rise to nonlocal correlations, as was elaborated in Chapter 3. In Chapter 5, on the other hand, we saw that a setup with an overall extension on the order of $10\,\mathrm{cm}$ and atomic velocities of $v_{\mathrm{rel}} = 1\mathrm{cm}/\mathrm{s}$ is possible as far as the laser parameters are concerned. I now complement this feasibility study from the point of view of the state generation within the Feshbach dissociation scheme.

To this end, let us proceed by deriving the asymptotic form of the two-particle state that is generated by a double pulse sequence in the described setup, allowing us to verify that it has the DTE structure (3.2) as described in Chapter 3. In particular, we can then specify the corresponding momentum spectrum, which plays a crucial role for the feasibility of the Bell test. Below in Section 7.3, this result is used to demonstrate explicitly that the resulting DTE state can violate a Bell inequality, despite of wave packet dispersion.

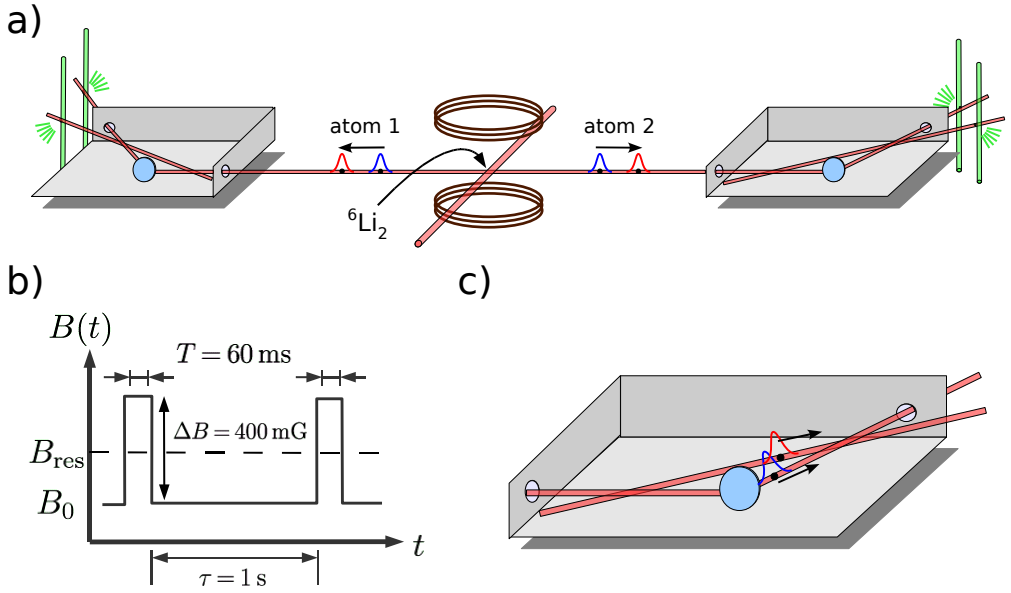

Figure 7.1: a) Experimental setup for the DTE Bell test. It starts with a $^6Li_2$ Bose-Einstein condensate of about 10^2 molecules in an optical dipole trap. A sequence of two short magnetic field pulses, as shown in b), dissociates on average one molecule per shot into a pair of counter-propagating atoms. The resulting two-particle state corresponds to a superposition of two subsequent dissociations, where each atom is delocalized into two consecutive wave packets that are separated by a distance of 5mm. The two atoms propagate in opposite directions along the laser guide and eventually enter switched, asymmetric Mach-Zehnder interferometers that are implemented by two more laser beams crossing the guide in a triangular arrangement at small angles. These second lasers are switched on after the early wave packets have passed the first crossing, but before the late wave packets arrive. An additional perpendicular, blue-detuned blocking laser beam, which is not depicted in the figure, may be used to support the deflection of the late wave packets. This way, the early wave packets have to take the long paths, whereas the late ones are directed into the short paths, as depicted in c). If the path length differences cancel the distance between the early and the late wave packets, they interfere and the joint probability of detection in the output ports of the interferometers exhibits a fringe pattern as a function of the path length difference variation. Correlations of the single-particle detection events thus have the potential to violate a Bell inequality.

Feshbach dissociation state

In the previous chapter we found that after an arbitrary magnetic field pulse sequence (close to an isolated resonance) the dissociated part of the state, $|\Phi_{\rm bg}(t)\rangle$, is described, for low energies, at positions far from the dissociation center, and at large times, by the asymptotic form (6.51)

$$|\Phi_{\rm bg}(t)\rangle \sim C_{\rm bg}|\varphi_{0,0}^{\rm cm}\rangle|\varphi_{0,0}^{\rm rel}\rangle \mathrm{U}_{z,t}^{(0)}|\Psi_z\rangle. \tag{7.1}$$

Here $\mathrm{U}_{z,t}^{(0)}$ denotes the free (two-particle) propagator in the longitudinal direction, while the transverse motion is frozen in the harmonic ground state, $|\varphi_{0,0}^{\rm cm}\rangle$ and $|\varphi_{0,0}^{\rm rel}\rangle$, resp., of the guiding laser beam. The longitudinal part of the two-particle state, expressed in the basis of the center of mass and relative momenta $p_{\rm cm}$ and $p_{\rm rel}$, is determined by (6.52)

$$\langle p_{\rm cm}, p_{\rm rel}|\Psi_z\rangle = \frac{\tilde{C}(p_{\rm cm}^2/4m\hbar + p_{\rm rel}^2/m\hbar + 2\omega_{\rm G})}{\|\tilde{C}\|}\langle p_{\rm cm}|\psi_{\rm T}\rangle, \tag{7.2}$$

where $\tilde{C}(\omega)$ is the Fourier transform of the closed-channel probability amplitude $C(t)$, $\tilde{C}(\omega) = \int_{-\infty}^{\infty} \mathrm{d}t \mathrm{e}^{\mathrm{i}\omega t} C(t)$. The Gaussian ground state of the trap laser $|\psi_{\rm T}\rangle$ reflects the trapping of the molecules before the dissociation. I substituted $U_{\rm bg} = 2\hbar\omega_{\rm G}$ in (7.2), neglecting the energy offset $-2U_{0,\rm G}$, which can be absorbed by a redefinition of the zero of energy. The quantity $\|\tilde{C}\|$ normalizes the spectrum according to (6.49), while the dissociation probability $|C_{\rm bg}|^2$ can be estimated by (6.53).

As was argued in the previous chapter, assuming a narrow resonance width and short pulse durations, such that on average only a single molecule dissociates out of the BEC, we can neglect the decay of the closed-channel amplitude $C(t)$ and restrict us to the uncoupled closed-channel amplitude $C_0(t)$. In a time-dependent magnetic field $B(t)$ its dynamics follows from (6.58)

$$C_0(t) = C_0(t_0)\exp\left(-\frac{\mathrm{i}}{\hbar}\int_{t_0}^{t} \mathrm{d}t'[E_{\rm res}(B(t')) - 2U_{0,\rm T} + \hbar\omega_{\rm G}]\right). \tag{7.3}$$

Note that I have substituted $U_{\rm cl} = -2U_{0,\rm T} + \hbar\omega_{\rm G}$, neglecting the comparatively small trap ground state energy $\hbar\omega_{\rm T}/2$ and the irrelevant offset $-2U_{0,\rm G}$. Let me remind the reader that the resonance energy $E_{\rm res}(B(t)) = \mu_{\rm res}(B(t) - B_{\rm res})$ is measured with respect to the background channel continuum threshold, whereas the trap laser potential depth $U_{0,\rm T}$ and the transverse trap frequency of the guiding laser $\omega_{\rm G}$ cause an additional energy offset that has to be overcome in the dissociation process. $C_0(t_0)$ indicates the probability amplitude for the two particles to be found in the resonance state at some initial time t_0 well before the dissociation pulses take place. Since we can assume that the magnetic field before t_0 has remained well below the resonance $B_{\rm res}$, the corresponding background channel component is negligible and we can safely set $C_0(t_0) = 1$ from now on.

Balanced double dissociation pulse

A DTE atom pair is extracted from the BEC by applying a sequence of two short square pulses in the external magnetic field, as shown in Fig. 7.1 b). We found in the last chapter that such square-shaped pulses optimize the momentum distribution with respect to its width. The pulse height must be chosen such that the desired dissociation velocity of $v_{\rm rel} = 1\mathrm{cm/s}$ is accomplished. To this end the pulses have to provide not only the

corresponding kinetic energy but also the energy required to overcome the longitudinal trap depth $U_{0,\mathrm{T}}$ and to reach the transversal ground state in the relative motion. The pulse duration, on the other hand, controls the width of the generated wave packets and the dissociation probability. For a sequence of two square pulses, each of height ΔB and duration T, separated by the time τ,

$$B(t) = B_0 + \Delta B\theta\left(t+\tau+\frac{T}{2}\right)\theta\left(-\tau+\frac{T}{2}-t\right) + \Delta B\theta\left(t+\frac{T}{2}\right)\theta\left(\frac{T}{2}-t\right), \quad (7.4)$$

the Fourier transform of (7.3) can be evaluated analytically, yielding

$$\begin{aligned}\tilde{C}_0(\omega) = &\frac{T\mu_{\mathrm{res}}\Delta B\,\mathrm{sinc}\left[\left(\omega-\mu_{\mathrm{res}}[B_0+\Delta B-B_{\mathrm{res}}]/\hbar+2U_{0,\mathrm{T}}/\hbar-\omega_{\mathrm{G}}\right)T/2\right]}{\hbar\omega-\mu_{\mathrm{res}}[B_0-B_{\mathrm{res}}]+2U_{0,\mathrm{T}}-\hbar\omega_{\mathrm{G}}} \\ &\times\left\{\exp\left(-\mathrm{i}\omega\tau\right)+\exp\left(\frac{\mathrm{i}}{\hbar}[2U_{0,\mathrm{T}}\tau-\mu_{\mathrm{res}}\Delta BT+\mu_{\mathrm{res}}(B_{\mathrm{res}}-B_0)\tau-\hbar\omega_{\mathrm{G}}\tau]\right)\right\},\end{aligned} \quad (7.5)$$

where we have neglected an irrelevant global phase. Here, B_0 stands for the magnetic field base value before and after the pulses, and B_{res} indicates the resonance position. Comparing (7.5) with the single pulse result (6.88), we confirm that on the level of the dissociation state the double pulse yields the superposition of the single pulse states, where the early wave packet undergoes a free time evolution in the period τ of the pulse separation. Note that we omitted the delta-function term, which only contributes at energies below the continuum threshold and hence does not affect the asymptotic dissociation state. It is now helpful to introduce the mean energy of the relative motion

$$\frac{p_0^2}{m} = \mu_{\mathrm{res}}(B_0+\Delta B-B_{\mathrm{res}})-2U_{0,\mathrm{T}}-\hbar\omega_{\mathrm{G}}, \quad (7.6)$$

as well as the characteristic width

$$\Delta p^2 = \frac{2m\hbar}{T}, \quad (7.7)$$

and the pulse energy $\bar{p}^2/m = \mu_{\mathrm{res}}\Delta B$. The dissociated state (7.2) thus takes the form

$$\begin{aligned}\|\tilde{C}_0\|\langle p_{\mathrm{cm}},p_{\mathrm{rel}}|\Psi_z\rangle = &\langle p_{\mathrm{cm}}|\psi_{\mathrm{T}}\rangle\frac{T\bar{p}^2\mathrm{sinc}\left[\left(p_{\mathrm{cm}}^2/4+p_{\mathrm{rel}}^2-p_0^2\right)/\Delta p^2\right]}{p_{\mathrm{cm}}^2/4+p_{\mathrm{rel}}^2-p_0^2+\bar{p}^2} \\ &\times\left\{\exp\left(-\mathrm{i}\left[\frac{p_{\mathrm{cm}}^2}{4m\hbar}+\frac{p_{\mathrm{rel}}^2}{m\hbar}\right]\tau\right)+\exp\left(\mathrm{i}\phi_\tau\right)\right\},\end{aligned} \quad (7.8)$$

where the relative phase between the early and the late dissociation component is given by

$$\phi_\tau = [2U_{0,\mathrm{T}}\tau-\mu_{\mathrm{res}}\Delta BT+\mu_{\mathrm{res}}(B_{\mathrm{res}}-B_0)\tau]/\hbar+\omega_{\mathrm{G}}\tau. \quad (7.9)$$

The DTE state

The desired dissociation velocity of $v_{\mathrm{rel}} = 1\mathrm{cm/s}$ is obtained for a narrow, sufficiently isolated resonance (resonance width $\Delta B_{\mathrm{res}} = 1\mathrm{mG}$ and $\mu_{\mathrm{res}} = 0.01\mu_{\mathrm{B}}$) by applying a pulse duration of $T = 60\,\mathrm{ms}$ and a pulse height of $B_0+\Delta B-B_{\mathrm{res}} = 200\,\mathrm{mG}$. The chosen pulse duration reconciles a small dissociation probability with the tight restrictions on the momentum distribution as imposed by dispersion, since the momentum spectrum (7.8) is sharply peaked at $(p_{\mathrm{cm}},p_{\mathrm{rel}}) = (0,\pm p_0)$, with $p_0/m = 5\mathrm{mm/s}$, for our choice of parameters. This is confirmed by considering the ratios $\sigma_{p,\mathrm{T}}/p_0$ and $\Delta p/p_0$, where $\sigma_{p,\mathrm{T}}$

denotes the momentum uncertainty exhibited by the longitudinal trap ground state $|\psi_{\rm T}\rangle$. In the harmonic approximation $\sigma_{p,{\rm T}} = \sqrt{\hbar\omega_{\rm T} m}$, this yields the ratio $\sigma_{p,{\rm T}}/p_0 = 0.024$, while the pulse duration $T = 60$ms implies $\Delta p/p_0 = 0.11$.

We can exploit the smallness of these ratios in order to calculate the normalization $\|\tilde{C}_0\|^2$ according to (6.49)

$$\|\tilde{C}_0\|^2 = \int_{-\infty}^{\infty} {\rm d}p_{\rm cm} \int_{-\infty}^{\infty} {\rm d}p_{\rm rel} \left| \tilde{C}_0 \left(\frac{p_{\rm cm}^2}{4m\hbar} + \frac{p_{\rm rel}^2}{m\hbar} + 2\omega_{\rm G} \right) \right|^2 |\langle p_{\rm cm}|\psi_{\rm T}\rangle|^2. \tag{7.10}$$

For this, we can focus on a single-pulse contribution, since in the limit $\tau \gg T$ the spectrum (7.8) represents the superposition of two spatially distinct dissociation states, which contribute equally to the norm. Within the range $\sigma_{p,{\rm T}}$ where $\langle p_{\rm cm}|\psi_{\rm T}\rangle$ is non-negligible, the Feshbach contribution $\tilde{C}_0(p_{\rm cm}^2/4m\hbar + p_{\rm rel}^2/m\hbar + 2\omega_{\rm G})$ to the right-hand side of (7.8) is only weakly dependent on the center-of-mass momentum $p_{\rm cm}$, which permits to replace $p_{\rm cm}$ by its mean value $p_{\rm cm} = 0$. The remaining integral over the relative momentum $p_{\rm rel}$ can be evaluated in good approximation by linearizing its argument in the vicinity of p_0. Setting $p_{\rm rel}^2 - p_0^2 \approx 2p_0(p_{\rm rel} - p_0)$ within the region of non-negligible $\tilde{C}_0(p_{\rm rel}^2/m\hbar + 2\omega_{\rm G})$ thus yields

$$\|\tilde{C}_0\|^2 = \frac{2\pi T^2 \Delta p^2}{p_0} \tag{7.11}$$

for the double pulse. With this, and acknowledging that the momentum dependent phase factor on the right-hand side of (7.8) effects a free time evolution, we end up with a longitudinal asymptotic wave packet of the form

$$|\Psi_z\rangle = \left({\rm U}_{z,\tau}^{(0)} + {\rm e}^{{\rm i}\phi_\tau} \right) |\Psi_0\rangle/\sqrt{2}. \tag{7.12}$$

Clearly, it has the structure (3.2) of a DTE state, being the superposition of an early and a late dissociation contribution, and the free time evolution of the early state component effecting a dispersion-induced distortion with respect to the late state component. The inferred single-pulse momentum spectrum reads

$$\langle p_{\rm cm}, p_{\rm rel}|\Psi_0\rangle = \frac{\sqrt{p_0}\bar{p}^2 {\rm sinc}\left[\left(p_{\rm cm}^2/4 + p_{\rm rel}^2 - p_0^2 \right)/\Delta p^2 \right]}{\sqrt{\pi}\Delta p \left(p_{\rm cm}^2/4 + p_{\rm rel}^2 - p_0^2 + \bar{p}^2 \right)} \langle p_{\rm cm}|\psi_{\rm T}\rangle, \tag{7.13}$$

which is plotted in Fig. 7.2 for our choice of parameters. Let me note that the trap ground state is determined by

$$\langle p_{\rm cm}|\psi_{\rm T}\rangle = \sqrt{\frac{\sqrt{(2/\pi)}\sigma_{\rm x,cm}}{\hbar}} \exp\left[-\left(\frac{\sigma_{\rm x,cm} p_{\rm cm}}{\hbar} \right)^2 \right], \tag{7.14}$$

where the position uncertainty follows from $\sigma_{\rm x,cm} = \sqrt{\hbar/(2\omega_{\rm T} M)}$. As anticipated, the spectrum (7.13) is sharply peaked at $(p_{\rm cm}, p_{\rm rel}) = (0, \pm p_0)$. In compliance with (3.3), the state $|\Psi_0\rangle$ describes a pair of symmetrically counterpropagating particles, in the sense that each particle can propagate in both directions, provided the other particle takes the opposite direction.

When the dissociation sequence is completed, and for our chosen time separation of $\tau = 1$s between the dissociation pulses, the early and late wave packets of each particle propagate at a velocity of 5 mm/s, separated by a distance of 5 mm on each side. Immediately after the dissociation process, the widths of the early and late single-particle wave

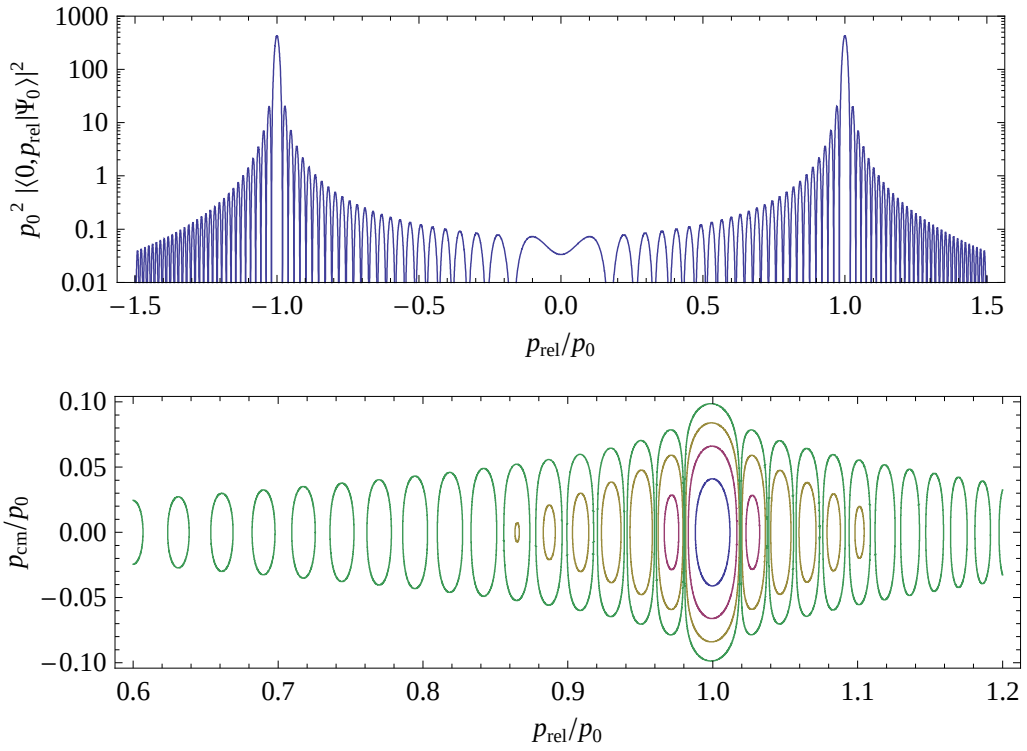

Figure 7.2: Momentum distribution $|\langle p_{\rm cm}, p_{\rm rel}|\Psi_0\rangle|^2$ for a single Feshbach dissociation pulse with pulse duration $T = 60$ms, magnetic field base value $B_{\rm res} - B_0 = 200$mG and pulse height $\Delta B = 400$mG. Assuming a longitudinal trap depth of $U_{0,\rm T}/k_B = 50$nK and a transverse trapping frequency of $\omega_{\rm G}/2\pi = 300$Hz this yields the dissociation velocity $p_0/m = 5$mm/s. The upper plot shows the momentum distribution in the $p_{\rm cm} = 0$ plane on a logarithmic scale. As required, the distribution exhibits sharp peaks at $(p_{\rm cm}, p_{\rm rel}) = (0, \pm p_0)$, corresponding to symmetrically counterpropagating particles. The lower logarithmic contour plot focuses on the vicinity of the $(p_{\rm cm}, p_{\rm rel}) = (0, +p_0)$ peak, including the dependence on the center of mass momentum $p_{\rm cm}$. The width in $p_{\rm rel}$ is characterized by $\Delta p^2 = 2m\hbar/T$, with $(\Delta p/p_0)^2 = 0.012$; the width in $p_{\rm cm}$ is essentially determined by the momentum uncertainty $\sigma_{p,\rm T}$ of the longitudinal trap laser ground state $|\psi_{\rm T}\rangle$, which follows from the trap frequency $\omega_{\rm T}/2\pi = 0.25$Hz, yielding $\sigma_{p,\rm T}/p_0 = 0.024$.

packets are on the order of about $200\,\mu$m. This follows from a Gaussian best fit on the momentum distribution (7.13) (which yields the general relation $\sigma_{p,\mathrm{rel}} \approx 2.4\mu\hbar/(p_0 T)$) and the Heisenberg uncertainty relation. The narrow momentum spectra of the wave packets guarantee that these extensions are not appreciably modified during the propagation to the interferometers if the propagation time does not exceed about 10 s. The early and late wave packets are thus still sufficiently separated when arriving at the interferometers for the switches to be applicable.

The dissociation probability for the double pulse sequence follows from Eqs. (6.53) and (7.11). It depends, apart from the shape of the magnetic field pulses, on the resonance parameters ΔB_{res} and μ_{res}, on the guiding laser trapping frequency ω_{G}, and on the background channel scattering length a_{bg}. For our parameters and a generic value of $a_{\mathrm{bg}} = 100a_0$, we get $|C_{\mathrm{bg}}|^2 \approx 0.04$, which confirms the assumed small dissociation fraction and thus justifies a posteriori the omission of the decay of the closed-channel amplitude in (7.3).

We rely on post-selection in order to guarantee that only one atom pair per shot enters the interferometers. This is unproblematic, since the final fluorescence detection of the slow, strongly confined atoms can be done with single particle resolution [91], such that it is easy to disregard the cases of multiple atom pairs in the process. For a start, we stick to this simple post-selection procedure; in a more refined setup it is conceivable to use a specially prepared optical lattice where each site is occupied by at most one molecule [95].

7.2 Interferometers and measurements

Since each atom in a DTE state is described by two spatially distinct, propagating wave packets, which correspond to the early and the late dissociation times, the use of switched, asymmetric Mach-Zehnder interferometers can serve first to endow these wave packets with additional relative phases and then to rejoin them. In detail, the early wave packets propagate through the long arms of the interferometers, whereas the late ones are directed through the short arms, see Fig. 7.1 c). If the detour of the early wave packets is chosen appropriately, they rejoin the late ones in the final beam splitters. The joint probability for detecting the particles in the output ports of the two interferometers then exhibits a fringe pattern under variation of either path length difference similar to Bell correlations. Let me remind the reader that in the DTE scenario the only relevant information required to extract these correlations is the output port combination where the atoms are detected. This information can be obtained by simple position measurements, without the need of a particular spatial or temporal resolution.

The interferometers may be implemented by two more red-detuned laser beams crossing the guide in a triangular arrangement at small angles, see Fig. 7.1. The path length differences must compensate the 5mm distance between the early and late wave packets of each particle. The variations of the path length differences required for the implementation of the Bell control parameters must be on the order of the de Broglie wave length $\lambda_{\mathrm{rel}} = 12.4\,\mu$m and can be achieved by shifting the crossing point of the two lasers or by inclining the mirror angles. The additional laser beams are switched on only after the early wave packets have passed the crossing points, but before the late ones arrive there. The crossings of the beams then act as beam splitters, while the required atom mirrors may be realized using evanescent light fields or blue-detuned laser beams perpendicular to the interferometer planes [106, 107]. Such perpendicular blocking beams at the crossing point of the first beam splitters could also support the full deflection of the

late wave packets into the short arms. This way, the early wave packets pass through the long arms, whereas the late wave packets are deflected into the short arms, as depicted in Fig. 7.1 c). Note that a simplified setup could do without the switching, replacing the switches by ordinary beam splitters, at the cost of 50% post-selection. The possibility to implement the switches with slow material particles, on the other hand, would avoid the drawback of a local hidden variable model, which photonic time-bin entanglement Bell tests have been suffering from [88, 89].

The particle detections in the output ports may be implemented by resonant laser beams crossing the guiding lasers behind the final beam splitters, as sketched in Fig. 7.1 a). They effect fluorescence detection with near unit efficiency and with single particle resolution [91]. As I argued in Chapter 3, it is natural from an experimental point of view to implement the detection by time-of-arrival measurements. This implies that one waits for the atoms to arrive at the continuously switched-on lasers. These are chosen sufficiently intense to detect the atoms at their passage with near unit efficiency, but without causing reflection of the wave packets [82–86]. In contrast to genuine position measurements, such time-of-arrival measurements do not require to illuminate a significant region in the output ports.

7.3 The DTE Bell test

In this section I demonstrate explicitly that the DTE state defined by (7.12) and (7.13), when subjected to the interferometric transformation, produces an experimentally resolvable fringe pattern that violates a Bell inequality.

DTE correlation function

In Chapter 3 we found that the joint probability for detecting a pair of counterpropagating atoms in a particular output port combination labeled by σ_1, σ_2 ($\sigma_i = \pm 1$) follows from

$$\begin{aligned} P_{\rm dte}(\sigma_1,\sigma_2|\ell_1,\ell_2) \\ =&\frac{1}{4}\left[1+\sigma_1\sigma_2 {\rm Re}\left\{{\rm e}^{-{\rm i}\phi_\tau}\int_{-\infty}^{\infty}{\rm d}p_{\rm cm}\int_{-\infty}^{\infty}{\rm d}p_{\rm rel}|\langle p_{\rm cm},p_{\rm rel}|\Psi_0^{(+)}\rangle|^2\right.\right. \\ &\left.\left.\times\exp\left({\rm i}\frac{p_{\rm cm}(\ell_1+\ell_2)}{2\hbar}+{\rm i}\frac{p_{\rm rel}(\ell_1-\ell_2)}{\hbar}-{\rm i}\frac{\tau(p_{\rm cm}^2/4+p_{\rm rel}^2)}{m\hbar}\right)\right\}\right]. \end{aligned} \tag{7.15}$$

In contrast to (3.17), it is convenient to evaluate the integrals in center of mass and relative coordinates. In accordance with (3.12), the two-particle momentum distribution $|\langle p_{\rm cm},p_{\rm rel}|\Psi_0^{(+)}\rangle|^2$ derives from the symmetric distribution $|\langle p_{\rm cm},p_{\rm rel}|\Psi_0\rangle|^2$ by restricting each particle to propagate into a particular direction, say, particle 1 into positive direction and particle 2 into negative direction. Hence we have

$$|\langle p_{\rm cm},p_{\rm rel}|\Psi_0^{(+)}\rangle|^2 = 2\theta(p_{\rm rel})|\langle p_{\rm cm},p_{\rm rel}|\Psi_0\rangle|^2,$$

where the additional factor 2 is imposed by normalization. If the two-particle momentum distribution $|\langle p_{\rm cm},p_{\rm rel}|\Psi_0\rangle|^2$ is sufficiently well-behaved and the path length differences ℓ_1, ℓ_2 are chosen such that the early and late wave packets overlap in the output ports, the detection probability (7.15) reveals a fringe pattern under variation of ℓ_1 and ℓ_2. It is remarkable that the quality of this fringe pattern is only affected by the free time evolution between the early and the late dissociation, whereas any subsequent time evolution does not have any effect, despite of the ongoing broadening of the wave packets.

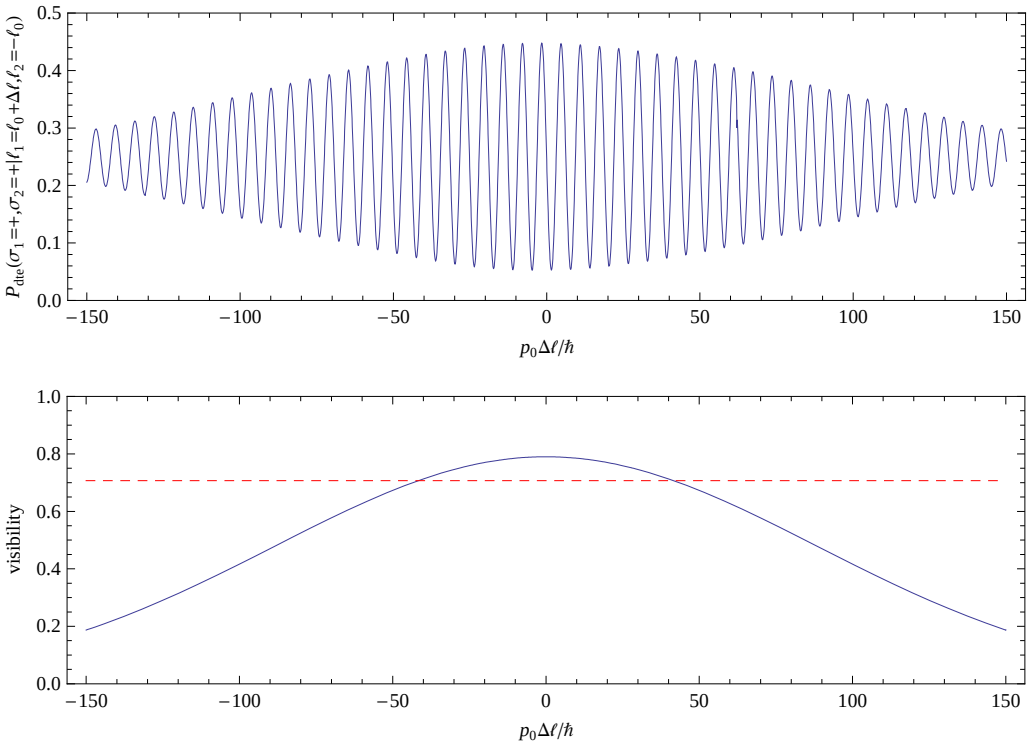

Figure 7.3: Joint probability $P_{\rm dte}(\sigma_1,\sigma_2|\ell_1,\ell_2)$ for detecting a pair of counter-propagating atoms in the output port combination $\sigma_1=+1$ and $\sigma_2=+1$ under variation of the path length difference ℓ_1. At the outset, ℓ_1 and ℓ_2 are chosen such that optimum overlap of the early and the late wave packets is achieved in the output ports of the beam splitters. The upper plot shows the resulting fringe pattern as it would be seen by the experimenter. The characteristic length for its period is set by the de Broglie wave length of the relative motion, $\lambda_{\rm rel}=12.4\mu$m. The finite range of the envelopes reflects the decreasing wave packet overlap with increasing offset $\Delta\ell$ from the optimum overlap value. The lower plot highlights the corresponding fringe visibility. The dashed line marks the visibility threshold that has to be exceeded in order to violate a Bell inequality. A sufficient number of fringes exceeds the threshold to manifest the corresponding violation.

For the single pulse momentum spectrum (7.13) of the DTE state (7.12) the joint detection probability (7.15) can be evaluated numerically. The resulting fringe pattern for the output port choice $\sigma_1=+1$ and $\sigma_2=+1$ under variation of ℓ_1 can be seen in Fig. 7.3. Specifically, we choose $\ell_1=\ell_0+\Delta\ell$ and $\ell_2=-\ell_0$, where $\ell_0=\tau p_0/m$ defines the optimum overlap path length difference canceling the separation between the early and the late wave packets. The variation of ℓ_2 or combinations of ℓ_1 and ℓ_2 would of course yield similar fringe patterns. The (constant) relative phase ϕ_τ is neglected since it only results in a phase shift of the fringe pattern, while the upper and lower envelope remain unaffected.

Inspecting Fig. 7.3, we can identify several generic features of the DTE fringe pattern. As it was the case for the Gaussian momentum distribution (3.20), the characteristic length for its period is set by the de Broglie wave length of the relative motion $\lambda_{\rm rel}=h/p_0$, indicating that the propagation-induced phase variation of the wave packets is responsible for their interference. In our case, we get $\lambda_{\rm rel}=12.4\mu$m. This means that,

in order to be able to detect the fringe pattern, the interferometers have to be kept stable by about 1μm.

The finite envelope size of the fringe pattern, on the other hand, can be traced back to the unavoidable offset from the optimum wave packet overlap when varying the path length differences. Interference cannot occur if the wave packets miss each other in the output ports. Indeed, the width of the fringe pattern, which is of about 200μm, matches approximately the initial position spread of the single-particle wave packets. Minor modifications to this can be traced back to the dispersion-induced distortion between the early and the late wave packets. We find that the envelope contains a sufficient number of fringes, which is in accordance with the Gaussian condition (3.21).

Possibility to observe a Bell violation

In Fig. 7.3 one observes an overall visibility reduction, which prevents the fringe pattern to vary with its maximum amplitude of 0.25 even in the case of optimum overlap. This was identified in Chapter 3 to be a genuine effect of the dispersion-induced distortion between the early and the late wave packets. Let me remind the reader of our insight that, if the early and late wave packets were identical up to displacement, the visibility should not be affected, independently of their shape, see also [36]. Taking the dispersion-induced distortion into account, only sufficiently well-behaved single-pulse momentum distributions guarantee the required fringe contrast. Indeed, the Gaussian analysis (3.20) revealed that the overall visibility is sensitive to the characteristic dispersion times $T_{\rm cm} = 2m\hbar/\sigma_{p,\rm cm}^2$ and $T_{\rm rel} = m\hbar/2\sigma_{p,\rm rel}^2$. The resulting fringe pattern can exceed the visibility threshold $1/\sqrt{2}$ as required for violating a Bell inequality only if these are at least on the order of the pulse separation time τ, $\tau/T_{\rm cm} \lesssim 1$ and $\tau/T_{\rm rel} \lesssim 1$, compare with (3.22). For our choice of τ and $v_{\rm rel}$, this translates into the condition that the center-of-mass and relative motion momentum spreads $\sigma_{p,\rm cm}$ and $\sigma_{p,\rm rel}$ be small compared to the average (relative) momentum p_0, $(\sigma_{p,\rm cm}/p_0)^2 \lesssim 2m\hbar/\tau p_0^2 \approx 10^{-3}$ and $(\sigma_{p,\rm rel}/p_0)^2 \lesssim m\hbar/2\tau p_0^2 \approx 10^{-4}$. As shown above, the momentum spreads are characterized in our case by $\sigma_{p,\rm T}/p_0 = 0.024$ and $(\Delta p/p_0)^2 = 0.012$. This yields indeed a momentum distribution that is sufficiently well peaked to violate a Bell inequality, as can be seen in the lower plot in Fig. 7.3. I emphasize that the potential violation sustains over a sufficient number of fringes to be resolvable in experiment.

Another viable approach to attain the expected fringe pattern is to fit the given (sufficiently well-behaved) momentum distribution with a Gaussian. This permits one to apply the above mentioned Gaussian analysis from Chapter 3, as was done in [35]. However, for spectra of the form (7.13) such a least square fit has the tendency to slightly overestimate the accessible visibility. A more conservative procedure than least square fitting would define the fit as an upper envelope of the corresponding momentum distribution. We note that the second momenta of the momentum distribution resulting from (7.13) are not useful for characterizing the widths of the peaks, while the Gaussian fitting procedure yields a comparatively good approximation in our context.

A final remark should be made on the relative phase ϕ_τ between the early and late state component. As can be seen in (7.15), it also enters the joint detection probability and hence influences the fringe pattern. It was neglected in the numerical investigation since it only effects a phase shift of the fringe pattern. Of course, this assumes that ϕ_τ remains constant from shot to shot, while an uncontrolled variation of ϕ_τ already on the order of 100 mrad would spoil the fringe pattern. In our Feshbach calculation ϕ_τ is determined by (7.9). Hence, we have to require that the magnetic field pulses can be

kept stable and are reproducible from shot to shot with a relative accuracy of 10^{-5}. This seems to be the most restrictive condition on the proposed experiment; surely it is not easy to achieve this accuracy, but it should be doable.

Conclusions Summarizing, I demonstrated that the implementation of the DTE Bell test within the Feshbach dissociation scheme is possible. Assuming viable experimental conditions, a double square-pulse dissociation state was shown to be capable of violating a Bell inequality. The setup allows one to reach macroscopic distances between the two measurement devices on the order of 10 centimeters. Remarkably, not only the two atoms are separated on a scale of several centimeters, but also the early and the late wave packets are separated by a distance of 5mm on each side. The experiment would thus manifest both delocalization and entanglement in the macroscopic regime.

Chapter 8

Hedgehog-rabbit Bell test in the Feshbach scenario

Following a line of arguments similar to the DTE case, I now discuss the generation of a HRE state in the Feshbach dissociation scenario. The HRE state generation protocol is distinguished from the DTE prescription by employing an unbalanced pulse sequence. Building on the results from Chapter 4, the corresponding Feshbach dissociation state is shown to exhibit Bell correlations with sufficient fringe contrast to support a Bell violation when subjected to position measurements in the overlap region and their a posteriori post-selection.

8.1 Extraction of a HRE atom pair

As pointed out in Chapter 4, the generation protocol for the HRE state is almost identical to that of the DTE state. A slight enhancement of the second dissociation pulse supplies the corresponding wave packets with a larger kinetic energy, enabling them to catch up with the preceding ones, see Figure 8.1. Position measurements in the overlap region on each side were shown to reveal nonlocal correlations, whose suitable dichotomization admits the formulation of a Bell test. I demonstrated the successful feasibility of the latter for Gaussian wave packets described by the parameters (4.10),

$$\begin{aligned} \tau = 1\,\mathrm{s}, \qquad & \sigma \approx 50\,\mu\mathrm{m}, \\ v_\mathrm{f} = 0.5\,\mathrm{cm/s}, \qquad & v_\mathrm{s} = 0.45\,\mathrm{cm/s}. \end{aligned} \tag{8.1}$$

We thus assume that these parameters are expedient candidates for the Feshbach scenario, as well. Here σ denotes the initial single-particle position uncertainty. Since these parameters are close to those of the DTE scenario, we can apply the same laser setup as presented in Chapter 5.1, where laser guiding of atoms with the nearby velocities v_f and v_s was shown to be possible. Moreover, the resulting meeting point $x_\mathrm{m} = 4.5\,\mathrm{cm}$ and meeting time $t_\mathrm{m} = 9\,\mathrm{s}$ satisfy the experimental limitations due to the finite Rayleigh length and photon scattering. The position uncertainty of the initial Gaussian center of mass state $|\psi_\mathrm{T}\rangle$ is determined by the trap laser and reads $\sigma_{x,\mathrm{T}} = \sqrt{\hbar/4\omega_\mathrm{T} m} \approx 40\,\mu\mathrm{m}$. It remains to be shown that the corresponding Feshbach dissociation state describing the relative motion with $\sigma_{x,\mathrm{rel}} \approx 50\,\mu\mathrm{m}$ is sufficiently well-behaved to support the required fringe contrast.

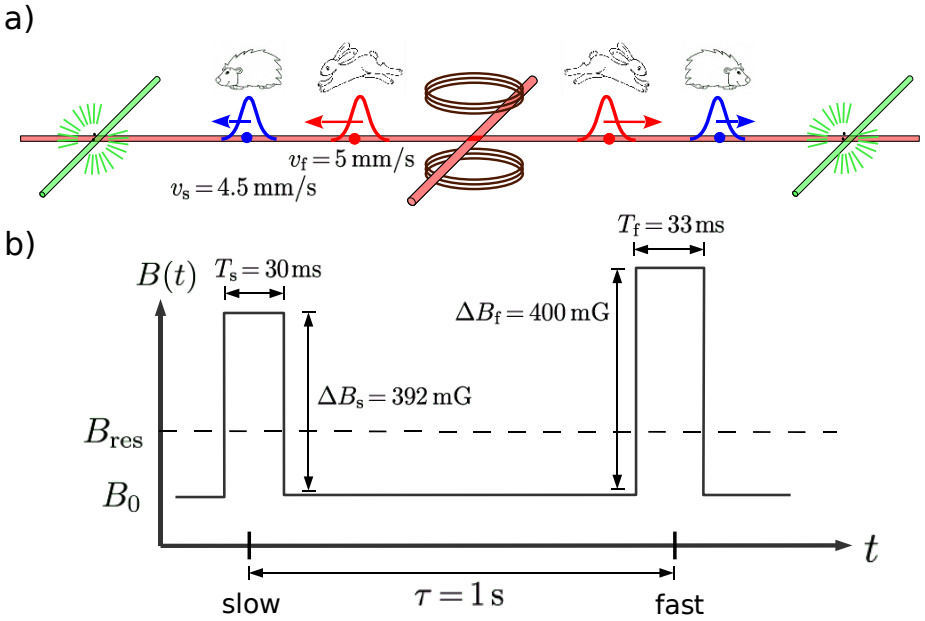

Figure 8.1: Generation of a HRE state in the Feshbach dissociation scenario. A sequence of two unbalanced, square-shaped magnetic field pulses, as shown in b), delocalizes each atom into two consecutive wave packets, such that the followers ("rabbits"), which are endowed with a larger kinetic energy, eventually catch up with the preceders ("hedgehogs"). The pulse parameters in b) yield wave packets that propagate with $v_s = 4.5\mathrm{mm/s}$ and $v_f = 5\mathrm{mm/s}$, respectively. Together with the resulting meeting point $x_m = 4.5\mathrm{cm}$ and time $t_m = 9\mathrm{s}$, these parameters are in compliance with the experimental frame presented in Chapter 5. Position measurements in the overlap region on each side reveal nonlocal correlations, whose suitable dichotomization admits their interpretation in terms of a Bell test. To this end, the measurement times take the role of the Bell control parameters. The square-shaped pulses yield momentum spectra that are sufficiently well-behaved to support the fringe contrast required for a Bell violation.

Unbalanced double dissociation pulse

We want to determine the Feshbach HRE state as produced by a sequence of two unbalanced square-shaped magnetic field pulses. In the previous Chapter we already found the Feshbach dissociation state for the balanced case. The reader is referred to this chapter for a short summary of the relation between applied magnetic field pulse and resulting asymptotic dissociation state. Generalizing to the situation depicted in Figure 8.1 b), a sequence of two dissociation pulses of duration T_s and T_f and height ΔB_s and ΔB_f, respectively,

$$B(t) = B_0 + \Delta B_\mathrm{s}\theta\left(t+\tau+\frac{T_\mathrm{s}}{2}\right)\theta\left(-\tau+\frac{T_\mathrm{s}}{2}-t\right) + \Delta B_\mathrm{f}\theta\left(t+\frac{T_\mathrm{f}}{2}\right)\theta\left(\frac{T_\mathrm{f}}{2}-t\right), \quad (8.2)$$

one obtains for the Fourier transform of the (uncoupled) closed-channel amplitude in close analogy to (7.5)

$$\begin{aligned}\tilde{C}_0(\omega) &= \frac{T_\mathrm{s}\mu_\mathrm{res}\Delta B_\mathrm{s}\mathrm{sinc}\left[(\omega-\mu_\mathrm{res}[B_0+\Delta B_\mathrm{s}-B_\mathrm{res}]/\hbar+2U_\mathrm{T}/\hbar-\omega_\mathrm{G})\,T_\mathrm{s}/2\right]}{\hbar\omega-\mu_\mathrm{res}[B_0-B_\mathrm{res}]+2U_\mathrm{T}-\hbar\omega_\mathrm{G}} \\ &\quad\times\exp(-\mathrm{i}\omega\tau) \\ &\quad+\frac{T_\mathrm{f}\mu_\mathrm{res}\Delta B_\mathrm{f}\mathrm{sinc}\left[(\omega-\mu_\mathrm{res}[B_0+\Delta B_\mathrm{f}-B_\mathrm{res}]/\hbar+2U_\mathrm{T}/\hbar-\omega_\mathrm{G})\,T_\mathrm{f}/2\right]}{\hbar\omega-\mu_\mathrm{res}[B_0-B_\mathrm{res}]+2U_\mathrm{T}-\hbar\omega_\mathrm{G}} \\ &\quad\times\exp\left(\frac{\mathrm{i}}{\hbar}[2U_\mathrm{T}\tau-\mu_\mathrm{res}\Delta B_\mathrm{s}T_\mathrm{s}+\mu_\mathrm{res}(B_\mathrm{res}-B_0)\tau-\hbar\omega_\mathrm{G}\tau]\right). \quad (8.3)\end{aligned}$$

Introducing again the mean energy $p_{0,\mathrm{s}}^2/m = \mu_\mathrm{res}(B_0+\Delta B_\mathrm{s}-B_\mathrm{res})-2U_\mathrm{T}-\hbar\omega_\mathrm{G}$, the characteristic width $\Delta p_\mathrm{s}^2 = 2m\hbar/T_\mathrm{s}$ and the pulse energy $\bar{p}_\mathrm{s}^2/m = \mu_\mathrm{res}\Delta B_\mathrm{s}$, and similar for $p_{0,\mathrm{f}}$, Δp_f and $\bar{p}_\mathrm{f}$, with ΔB_s and T_s replaced by ΔB_f and T_f, the dissociated state now reads as

$$\begin{aligned}\langle p_\mathrm{cm}, p_\mathrm{rel}|\Psi_z\rangle &= \langle p_\mathrm{cm}|\psi_\mathrm{T}\rangle\frac{T_\mathrm{s}\bar{p}_\mathrm{s}^2\mathrm{sinc}\left[\left(p_\mathrm{cm}^2/4+p_\mathrm{rel}^2-p_{0,\mathrm{s}}^2\right)/\Delta p_\mathrm{s}^2\right]}{\|\tilde{C}_0\|(p_\mathrm{cm}^2/4+p_\mathrm{rel}^2-p_{0,\mathrm{s}}^2+\bar{p}_\mathrm{s}^2)} \\ &\quad\times\exp\left(-\mathrm{i}\left[\frac{p_\mathrm{cm}^2}{4m\hbar}+\frac{p_\mathrm{rel}^2}{m\hbar}\right]\tau\right) \\ &\quad+\langle p_\mathrm{cm}|\psi_\mathrm{T}\rangle\frac{T_\mathrm{f}\bar{p}_\mathrm{f}^2\mathrm{sinc}\left[\left(p_\mathrm{cm}^2/4+p_\mathrm{rel}^2-p_{0,\mathrm{f}}^2\right)/\Delta p_\mathrm{f}^2\right]}{\|\tilde{C}_0\|(p_\mathrm{cm}^2/4+p_\mathrm{rel}^2-p_{0,\mathrm{f}}^2+\bar{p}_\mathrm{f}^2)}\exp(\mathrm{i}\phi_\tau). \quad (8.4)\end{aligned}$$

The relative phase between the early and the late dissociation component is given here by

$$\phi_\tau = [2U_\mathrm{T}\tau-\mu_\mathrm{res}\Delta B_\mathrm{s}T_\mathrm{s}+\mu_\mathrm{res}(B_\mathrm{res}-B_0)\tau]/\hbar+\omega_\mathrm{G}\tau. \quad (8.5)$$

As expected, the state superposes structurally similar wave packets of different velocities.

Pulse parameters

The aspired state properties (8.1) can be obtained by choosing the pulse parameters

$$\begin{aligned}B_0+\Delta B_\mathrm{s}-B_\mathrm{res} &= 192\,\mathrm{mG}, \qquad B_0+\Delta B_\mathrm{f}-B_\mathrm{res} = 200\,\mathrm{mG}, \\ T_\mathrm{s} &= 30\,\mathrm{ms}, \qquad T_\mathrm{f} = \frac{v_\mathrm{f}}{v_\mathrm{s}}T_\mathrm{s} = 33\,\mathrm{ms}. \quad (8.6)\end{aligned}$$

The pulse durations are chosen such that they yield equal dissociation probabilities for the early and late state component. In addition, the momentum spectra are sharply peaked at $(p_{\mathrm{cm}}, p_{\mathrm{rel}}) = (0, \pm p_{0,\mathrm{s}})$ and $(p_{\mathrm{cm}}, p_{\mathrm{rel}}) = (0, \pm p_{0,\mathrm{f}})$, with $p_{0,\mathrm{s}}/m = 4.5\,\mathrm{mm/s}$ and $p_{0,\mathrm{f}}/m = 5\,\mathrm{mm/s}$, respectively. The center of mass uncertainty $\sigma_{p,\mathrm{T}}/p_{0,\mathrm{f}} = 0.024$ remains unchanged as compared to the DTE scenario, since we choose the same trap laser parameters, and the corresponding ratio for the slow component is modified insignificantly to $\sigma_{p,\mathrm{T}}/p_{0,\mathrm{s}} = 0.027$. The uncertainties in the relative motion now amount to $\Delta p_{\mathrm{f}}/p_{0,\mathrm{f}} = 0.15$ and $\Delta p_{\mathrm{s}}/p_{0,\mathrm{s}} = 0.17$, which is due to the approximate halving of the pulse durations as compared to the DTE protocol. The smallness of these ratios admits to calculate the normalization $\|\tilde{C}_0\|^2$ following the same reasoning as in Chapter 7. One thus obtains

$$\|\tilde{C}_0\|^2 = \pi T_{\mathrm{s}}^2 \Delta p_{\mathrm{s}}^2/p_{0,\mathrm{s}} + \pi T_{\mathrm{f}}^2 \Delta p_{\mathrm{f}}^2/p_{0,\mathrm{f}}, \tag{8.7}$$

in analogy to (7.11). Since the chosen pulse durations yield equal dissociation probabilities for both pulses, this can be rewritten as

$$\|\tilde{C}_0\|^2 = 2\pi T_{\mathrm{s}}^2 \Delta p_{\mathrm{s}}^2/p_{0,\mathrm{s}} = 2\pi T_{\mathrm{f}}^2 \Delta p_{\mathrm{f}}^2/p_{0,\mathrm{f}}. \tag{8.8}$$

HRE state

The dissociation state (8.4) describes the superposition of two wave packets, where the momentum dependent phase factor on the right-hand side effects a free time evolution. We thus can write

$$|\Psi_z\rangle = \left(\widehat{\mathrm{U}}_{z,\tau}^{(0)}|\Psi_{\mathrm{S}}\rangle + \mathrm{e}^{\mathrm{i}\phi_\tau}|\Psi_{\mathrm{F}}\rangle\right)/\sqrt{2}. \tag{8.9}$$

Properly normalized, the early slow state component in momentum representation reads as

$$\langle p_{\mathrm{cm}}, p_{\mathrm{rel}}|\Psi_{\mathrm{S}}\rangle = \frac{\sqrt{p_{0,\mathrm{s}}}\bar{p}_{\mathrm{s}}^2 \mathrm{sinc}\left[\left(p_{\mathrm{cm}}^2/4 + p_{\mathrm{rel}}^2 - p_{0,\mathrm{s}}^2\right)/\Delta p_{\mathrm{s}}^2\right]}{\sqrt{\pi}\Delta p_{\mathrm{s}}\left(p_{\mathrm{cm}}^2/4 + p_{\mathrm{rel}}^2 - p_{0,\mathrm{s}}^2 + \bar{p}_{\mathrm{s}}^2\right)}\langle p_{\mathrm{cm}}|\psi_{\mathrm{T}}\rangle, \tag{8.10}$$

and similar for $|\Psi_{\mathrm{F}}\rangle$, with $p_{0,\mathrm{s}}$, Δp_{s} and $\bar{p}_{\mathrm{s}}$ replaced by $p_{0,\mathrm{f}}$, Δp_{f} and $\bar{p}_{\mathrm{f}}$. These momentum distributions are structurally similar to the DTE case depicted in Figure 7.2. The expressions (8.9) and (8.10) clearly reproduce the structure of the HRE state (4.1). The dissociation probability for the parameters (8.6) is approximately halved as compared to the DTE case, $|C_{\mathrm{bg}}|^2 \approx 0.02$, which stems from the halving of the pulse durations. This can be compensated by doubling the number of condensed molecules or by choosing a wider resonance.

In order to get an estimate of the position uncertainty in the relative motion, one may determine a Gaussian best fit on the momentum distribution (8.10) and then use the Heisenberg uncertainty relation. The thus obtained general relation

$$\sigma_{p,\mathrm{rel,s}} \approx 2.4\frac{\mu\hbar}{p_{0,\mathrm{s}}T_{\mathrm{s}}}, \tag{8.11}$$

and similar for $\sigma_{p,\mathrm{rel,f}}$, then yields $\sigma_{x,\mathrm{rel,s}} \approx 56\,\mu\mathrm{m}$ and $\sigma_{x,\mathrm{rel,f}} \approx 70\,\mu\mathrm{m}$ for the pulse parameters (8.6). This confirms, in combination with $\sigma_{x,\mathrm{T}} \approx 40\,\mu\mathrm{m}$, the approximate reproduction of the HRE parameters (8.1).

8.2 The HRE Bell test

In the following, we investigate the HRE scenario when applied to the Feshbach dissociation state (8.9) and (8.10).

Position correlations

In Chapter 4 we determined the joint probability density $\mathrm{P}(x_1,x_2|t_1,t_2)$ to detect atom 1 at position x_1 when measuring at time t_1 and atom 2 at position x_2 when measuring at time t_2 for a general HRE state, compare with (4.8). The HRE state was characterized by the two-particle momentum representations $\tilde{\Psi}_{\mathrm{S}}(p_1,p_2)$ and $\tilde{\Psi}_{\mathrm{F}}(p_1,p_2)$ of the early slow and late fast state components. Specializing to the Feshbach dissociation state (8.10), we must transform from the center of mass and relative coordinates to single-particle coordinates using $p_{\mathrm{cm}} = p_1 + p_2$ and $p_{\mathrm{rel}} = (p_1 - p_2)/2$, respectively; with this we can identify $\tilde{\Psi}_{\mathrm{S}}(p_1,p_2) = \langle p_{\mathrm{cm}}, p_{\mathrm{rel}}|\Psi_{\mathrm{S}}\rangle$, and similar for $\tilde{\Psi}_{\mathrm{F}}(p_1,p_2)$.

Remember that (4.8) was derived under the assumption that the wave packets are detected in the dispersion-dominated regime, where they are essentially determined by their momentum distribution, irrespectively of their initial spatial shape. For Gaussian wave packets it was shown by comparison with the exact result that this constitutes an excellent approximation for the parameters (8.1). Since the Feshbach dissociation state (8.10) reproduces these parameters fairly well, it is legitimate to transfer the validity of (4.8) to this state.

The resulting spatial fringe pattern is shown in Figure 8.2. The seemingly Gaussian shape of its envelope stems from the center of mass trap state; however, we will find that the dichotomic two-particle correlations are strongly influenced by the non-Gaussian relative motion. Linearization in the vicinity of the meeting point $x_{\mathrm{m}} = v_{\mathrm{f}}\tau/(v_{\mathrm{f}}/v_{\mathrm{s}} - 1) = 4.5\,\mathrm{cm}$ and the meeting time $t_{\mathrm{m}} = \tau/(v_{\mathrm{f}}/v_{\mathrm{s}} - 1) = 9\,\mathrm{s}$ predicts the spatial period $\lambda_{\mathrm{hre}} = h/(p_{\mathrm{f}} - p_{\mathrm{s}}) = 137\,\mu\mathrm{m}$ and the temporal period $T_{\mathrm{hre}} = h/(p_{\mathrm{f}}^2/2m - p_{\mathrm{s}}^2/2m) = 29\,\mathrm{ms}$. The former can be confirmed by inspection of Figure 8.2, the latter by inspection of Figure 8.3 b).

Dichotomic correlation function

In order to come up with Bell correlations, we introduced in Chapter 4 a prescription that assigned to each position measurement outcome a dichotomic value, adopting the periodic structure of the spatial fringe pattern, see Figure 8.2. The joint probability to detect atom 1 at a position that has been assigned to the dichotomic value σ_1 when measuring at t_1 and to detect atom 2 at a position that has been assigned to σ_2 when measuring at t_2 can then be written as

$$\mathrm{P}(\sigma_1,\sigma_2|t_1,t_2) = \int \mathrm{d}x_1 \int \mathrm{d}x_2 \chi_{\sigma_1}(x_1)\chi_{\sigma_2}(x_2)\mathrm{P}(x_1,x_2|t_1,t_2), \tag{8.12}$$

where the appropriate dichotomization functions $\chi_\sigma(x)$ are determined by (4.30). This definition of the dichotomization functions includes the possibility to disregard a fraction $p - 1 < 1$ of the position measurement outcomes, where p denotes the post-selected fraction. In principle, we can evaluate (8.12) numerically for the Feshbach dissociation state (8.10), as will be done below; however, a deeper insight into the correlation function is gained by making use of the scale separation (the envelope varies slowly over the extent of a spatial period) and the local linearizability of the fringe pattern. This permits one to derive the analytic expression (4.33) for the correlation function (normalized on the post-selected fraction),

$$\mathrm{P}^{(\mathrm{ps})}(\sigma_1,\sigma_2|t_1,t_2) = \frac{1}{4}\left\{1 + \sigma_1\sigma_2 E(t_1,t_2)\mathrm{sinc}^2\left[\frac{\pi}{2}p\right]\cos\left[\omega(\Delta t_1 + \Delta t_2) - \phi'\right]\right\}, \tag{8.13}$$

which makes the analogy with the Bell correlation function manifest. The validity of these assumptions for our set of parameters can be confirmed by inspection of Figure 8.2.

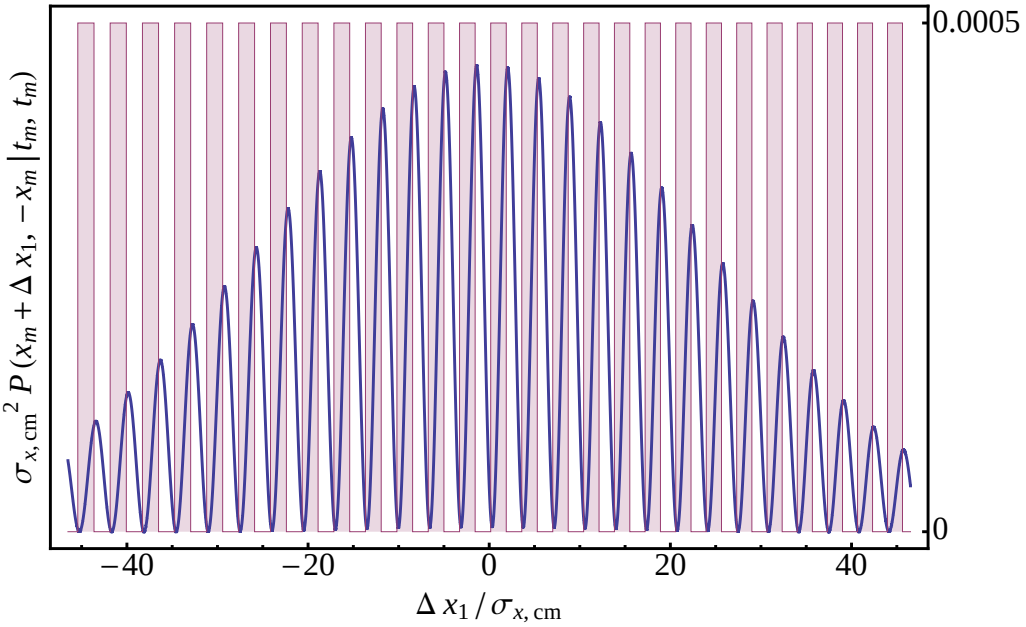

Figure 8.2: Joint detection probability density (4.8) for the Feshbach dissociation state (8.10), conditioned on one atom being detected at the meeting point and at the meeting time. This is superimposed by the corresponding dichotomization function (4.30) with $p = 1$ (truncated at 0.0005). Although the single-particle spatial fringe pattern seems to be dominated by the Gaussian center of mass state, the non-Gaussian relative motion in (8.10) strongly influences the two-particle correlations. The length scale of the fringe pattern is accurately reproduced by the linear prediction $\lambda_{\mathrm{hre}} = h/(p_{\mathrm{f}} - p_{\mathrm{s}}) = 137\mu\mathrm{m} = 3.4\,\sigma_{x,\mathrm{cm}}$, as expected. Interference patterns on that scale can be resolved conveniently, e.g., with laser illumination. The extent of the envelope Δx_{max}, on the other hand, which is on the order of $\Delta x_{\mathrm{max}} \approx 10^2 \sigma_{x,\mathrm{cm}} \approx 4\,\mathrm{mm}$, determines the region to be illuminated. From the plot we can confirm the slow variation of both the spatial period (local linearizability) and the envelope as compared to the wave length (scale separation). The analytic expression of the dichotomic correlation function (8.13) is based on these two assumptions. The superimposed dichotomization function (4.30) is chosen to adopt the periodic structure of the fringe pattern; in spite of the rather small variation of the spatial period, such an adaptive dichotomization is required in order to maintain the phase relation over the entire extent of the envelope.

The visibility of the fringe pattern is controlled, aside from the post-selection parameter p, by the envelope function $E(t_1,t_2)$, which describes the overlap of the early slow and late fast wave packets, compare with (4.28).

Bell violation

The structural similarity between the dichotomic correlation function (8.13) and the Bell correlation function (2.7) permits one to interpret the HRE scenario in terms of a Bell test. In order to establish a Bell violation it is required that the visibility of the fringe pattern exceeds the threshold value $1/\sqrt{2} \approx 0.71$, which can only be achieved when taking post-selection into account, $p < 0.63$, even in the case of optimum overlap, $E(t_\mathrm{m},t_\mathrm{m}) \approx 1$. In fact, for the dissociation state (8.10) the envelope function (4.28) evaluates at the meeting time as $E(t_\mathrm{m},t_\mathrm{m}) \approx 0.85$, which is certainly well above $1/\sqrt{2}$. However, it requires to post-select to a fraction with $p < 0.46$. Remarkably, the Gaussian states (4.2) yielded $E(t_\mathrm{m},t_\mathrm{m}) \approx 1$ for similarly chosen parameters, compare with (4.29). The visibility reduction regarding the dissociation state hence reflects the influence of its less well-behaved non-Gaussian relative motion.

Figure 8.3 a) shows the envelope function (4.28) evaluated for the dissociation state (8.10) as a function of the measurement time. It exhibits a plateau over a range of about 2 s in the vicinity of the meeting time, and hence covers a multitude of temporal periods $T_\mathrm{hre} = 29\,\mathrm{ms}$, which enables the experimenter to sweep over several fringe maxima without significant loss of contrast. Remember that she controls the measurement times and thus can ensure to remain close to t_m. Figure 8.3 b) compares the analytic correlation function (8.13) with the direct numerical evaluation of (8.12) for the dissociation state (8.10). The good agreement of their contrast confirms the validity of the underlying assumptions (scale separation and local linearizability), whose applicability was already indicated in Figure 8.2. The discrepancy in the phase can be traced back to the redefinition of the phase of the dichotomization functions in the derivation of (8.13).

8.3 Implementation of position measurements

The feasibility of the HRE Bell test is based on the experimental ability to perform position measurements with an accuracy sufficient to resolve the spatial fringe pattern, whose scale is determined by $\lambda_\mathrm{hre} = 137\,\mu\mathrm{m}$. Available technology suggests to employ laser illumination for the implementation of the position measurements, see Figure 8.1. The detection of emitted fluorescence photons with CCD cameras admits a spatial resolution on the order of $10\,\mu\mathrm{m}$ [91]. This resolution also accounts for the random walk the atoms undergo due to the photon absorption- and emission-induced momentum kicks. The spatial extent of the envelope of the fringe pattern, on the other hand, determines the required region of illumination. From Figure 8.2 we can estimate the width of the envelope to be $\Delta x_\mathrm{max} \approx 100\,\sigma_{x,\mathrm{cm}} = 4\,\mathrm{mm}$, which sets the scale for the beam waist.

Note that the finite resolution of the position measurements effects a coarse-graining of the detected fringe pattern, which diminishes the fringe contrast and hence has ultimately the potential to threaten the Bell violation. However, coarse-graining on the level of less than 10% of the period λ_hre renders this effect marginal. The resolution of the temporal period of the fringe pattern, $T_\mathrm{hre} = 29\,\mathrm{ms}$, on the other hand, does not pose any experimental challenge.

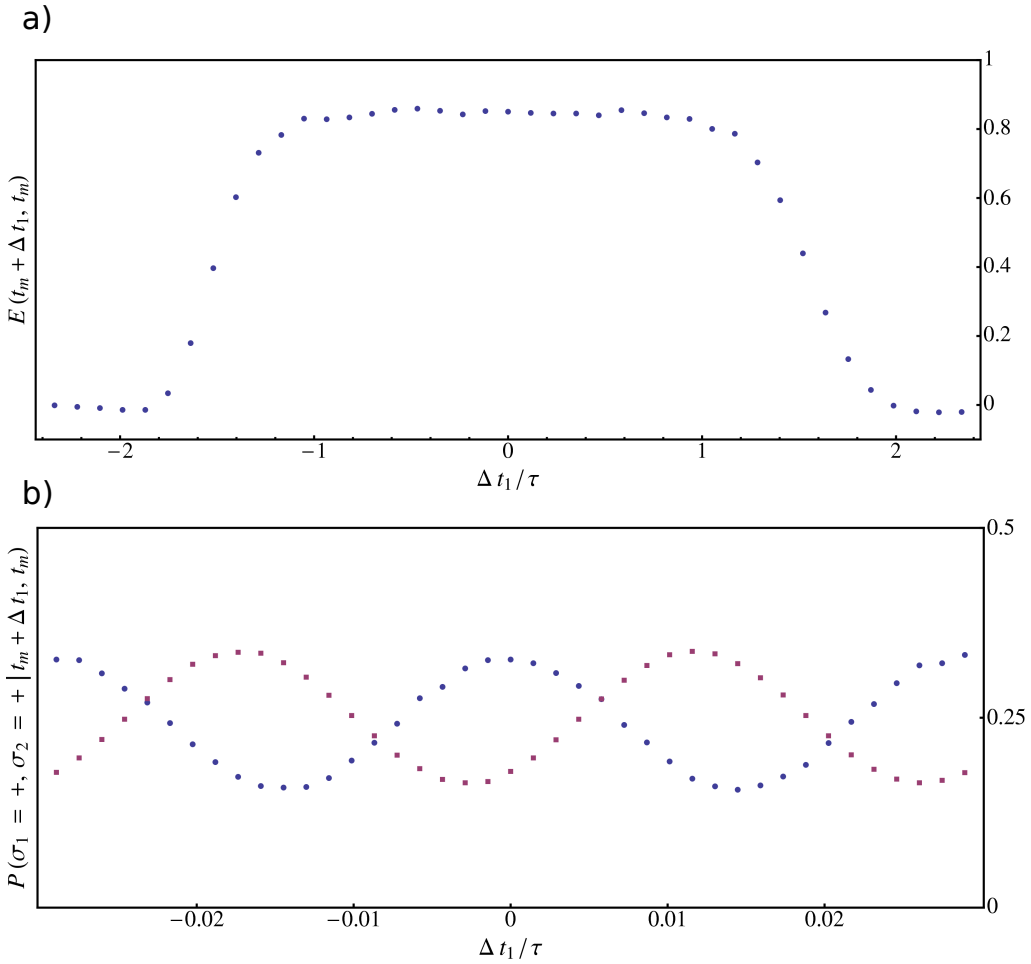

Figure 8.3: a) Envelope (4.28) of the correlation function (8.13) evaluated for the Feshbach dissociation state (8.10) as a function of the measurement time. It exhibits a plateau at approximately 0.85, which is sufficiently well above the Bell threshold value of $1/\sqrt{2} \approx 0.71$. Since the period of the fringe pattern, $T_{\text{hre}} = 29\,\text{ms}$ (compare with b)) is much smaller than the envelope width of about 2 s, the experimenter can probe a multitude of fringes without loss of contrast, the measurement times being under her control. In combination with moderate post-selection of a fraction of $p < 0.46$ of the measurement outcomes, the structural similarity of the HRE correlation function (8.13) to the Bell correlation function thus renders the violation of a Bell inequality in the Feshbach scenario possible. b) Comparison of the analytic correlation function (8.13) (squares) with the direct numerical evaluation of (8.12) for the dissociation state (8.10) (circles). One finds that the analytic expression reproduces the form of the fringe pattern accurately, thus confirming the validity of the underlying approximations. The relative phase shift stems from the deliberate redefinition of the phase of the dichotomization functions in the derivation of (8.13). As expected, the period of the fringe pattern matches the linear prediction $T_{\text{hre}} = 29\,\text{ms}$.

Summary

I demonstrated the experimental feasibility of the HRE Bell test in the Feshbach dissociation scheme with the prospect to achieve a Bell violation. In contrast to the DTE scenario, the HRE scenario needs not to employ interferometers and is based on a genuine matter wave state that does not have a photonic analogue. A successful HRE Bell test requires phase stability over the whole extent of the experiment, which is approximately 10 cm. However, this is not problematic for fringe distances on the order of $100\,\mu$m. Like in the DTE scenario, the magnetic field pulses should be reproducible from shot to shot with a relative accuracy of 10^{-5}, which is not easy, but doable.

Chapter 9

Conclusions

9.1 Summary

I presented two complementary scenarios to detect Bell correlations in the motion of material particles, bridging the gap between a nonclassicality test formulated for nontrivially related dichotomic observables and a continuous variable system that only has position measurements easily at its disposal. Both proposals are based on the gradual dissociation of ultracold Feshbach molecules and they feature macroscopic delocalizations of the atomic states. By giving a full account of these scenarios, including the coupled-channel description of the Feshbach dissociation, the optically guided dispersive propagation, interferometric processing and the final position measurements by laser illumination, I demonstrated in both cases the potential to violate a Bell inequality under experimentally viable conditions that would admit delocalizations and interatomic separations on the order of centimeters.

The **dissociation-time entanglement (DTE) scenario** superposes macroscopically distinct wave packets of equal velocity and relies on single-particle interferometry to accomplish the Bell correlations. It is shown that conclusive nonlocal correlations are achieved within a range of tolerance as imposed by dispersion. By tracing them back to the coherence properties between the early and late wave packets as a whole means that only port-selective measurements are needed, requiring neither prominent spatial nor temporal resolution. The asymmetric Mach-Zehnder interferometers can be implemented with laser beams, where the slow velocities of the ultracold atoms admit the easy realization of switches, in contrast to photonic time-bin entanglement. In addition, the nearly one hundred percent detection probability does not come into conflict with the detection loophole, outperforming the poor detection efficiency for photons. The implied first closure of the detection loophole at macroscopic separations would be a huge step forward with respect to a loophole-free refutation of local realism. Finally, since only single-particle interference has to be performed, the interferometers on the opposite sides do not have to be kept stable with respect to each other, which permits the experimenter to put them easily at large distances.

Hedgehog-rabbit entangled (HRE) states, on the other hand, are genuine matter wave states superposing wave packets of differing velocities. Position measurements in the overlap regions on both sides and their appropriate dichotomization replace the interferometers, requiring instead a higher spatial and temporal measurement resolution and phase stability between the measurement sites. The necessary post-selection relies on the fair sampling assumption; by redefining the measurement assignments, however, the whole sample can be involved in a Bell violation.

According to the **Feshbach dissociation scheme**, both the DTE and the HRE states are generated by applying sequences of two magnetic field pulses. Hence, no complicated manipulation of the molecular state is required, the only experimental demand is to keep the molecules trapped in a controlled way and to carry out the magnetic field pulses with sufficient accuracy.

A coupled-channel formalism describes the asymptotic Feshbach dissociation state for given magnetic field pulses. This is achieved in two steps: First, the background channel dissociation state is expressed in terms of the closed-channel amplitude, whose dynamics then are solved when exposed to a time-varying external magnetic field. The relation between applied magnetic field pulse and resulting dissociation state reveals that one faces strong limitations on the possibility to tailor a pulse shape so as to generate a desired dissociation state. However, square-shaped magnetic field pulses, which optimize the momentum distribution with respect to its sharpness, are shown to yield states that are sufficiently well-behaved to admit Bell violations in both scenarios.

An experiment that delocalizes and entangles the motion of matter waves on a macroscopic scale would **probe the validity of quantum mechanics** (QM) in a hitherto unexplored combination of parameter regimes and degrees of freedom that one usually attributes to the classical realm. The violation of a Bell inequality would, on the one hand, unambiguously verify both the entanglement and the delocalization of the states; on the other hand, it would extend the refutation of a local realistic description to the motion of material particles, at scales that are in principle amenable to a direct perception without any supplementary devices.

While such experiments must have been considered purely hypothetical in the early days of QM, the recent progress in the manipulation of ultracold atomic systems has brought them into experimental reach. Despite of the important contributions of photon experiments to foundational issues and their great use for quantum information technologies, this step from photons to material particles seems highly desirable from a fundamental point of view.

One might even think of a demonstration experiment, where only after the dissociation of the particles the experimenter makes the conscious decision whether she wants to check the correlation of the emission times, by “looking” at the particles in front of the interferometers (or before the overlap), or whether she wants to check the nonlocal correlations, by “looking” at the particles behind of the interferometers (or in the overlap region). This way, by performing such an experiment with proper, material particles and on truly macroscopic scales on the order of centimeters, nonclassical quantum correlations would be manifest for anyone who understands the basic concept of the position of a particle, even for cocksure classical physicists or a layman who is ignorant of physics.

9.2 Outlook

Let me conclude by mentioning some possible ways to build upon the results of this thesis. This is intended to demonstrate that its findings do not stand solitary, but can serve as the starting point of a research program of its own, exploring the possibilities, consequences and limitations of macroscopic entanglement in the motion of material particles.

Naturally, it would be illuminating to investigate the influence of various **sources of decoherence**. While the effect of scattering of off-resonant photons and the scattering of background particles was already found to be controllable [35], it would be interesting to check to what degree the present setups can be used to test possible unconventional

collapse theories, which predict a loss of coherence in the motion of material particles, e.g. due to purported quantum gravity effects, on the centimeter scale accessible for the first time with the present measurement schemes.

Turning towards further applications of the DTE scenario, the established motional implementation of the Bell experiment both on the state level and on the measurement level implies that it can be used to transfer other quantum information strategies to the motion of material particles, such as the **teleportation** of a qubit state [108, 109]. Encoding qubits in spatially distinct wave packets thus permits general single-qubit state processing to be based only on matter wave optics and subsequent position measurements. This gives us a simple and robust method at hand for performing some of the most relevant quantum tests in the *motion* of material particles.

In particular, the complete operational correspondence to the Bell state correlations in the DTE scenario including also "out of plane"-measurements should admit to **test Leggett's model of crypto-nonlocal realism** in the motion. As mentioned in Chapter 2, Leggett introduced a nonlocal model to account for the measurement outcomes in the spin Bell experiment [47]. It probes the idea that local properties should be describable by pure states, whereas correlations between the two parties may be nonlocal, merely restricted by the no-signaling condition. In the DTE scenario it would thus test whether the early and the late wave packets of each particle behave in local measurements as being in a pure superposition (more precisely, a classical mixture of such). Leggett could derive an inequality that is met by his model, but violated by QM [47]. In contrast to the Bell test, a violation of Leggett's inequality requires the implementation of "out of plane"-measurements; moreover, it can only be achieved when the visibility of the fringe pattern exceeds $v \approx 0.94$ [49]. While the former is naturally provided in the DTE scenario, the latter can only be achieved by either considerably decreasing the time separation τ between the dissociation pulses (which implies down-scaling the interferometers), or by further sharpening the momentum distributions of the wave packets. A thorough investigation to reassure the possibility of such a violation seems worthwhile.

The HRE scenario, on the other hand, might serve to **test (a conservative interpretation of) Bohmian mechanics**. Bohm originally introduced his version of QM as a means to explain the outcomes of position measurements (as described by Born's rule) by a classical probability distribution of realistically interpretable particle trajectories. While he was able to establish complete equivalence with the predictions of QM on the level of equal time measurements, it has been argued that measurements and correlations involving different times could come into conflict with QM [110]; in particular, this is the case if the correlations violate a Bell inequality [90]. Modern followers of Bohm's theory usually resolve this contradiction by adhering to a contextual interpretation of position measurements, which necessarily requires to describe the measurement apparatus within the theory in order to explain the emergence of measurement outcomes [51]. However, this way the probability distribution of the trajectories loses its original interpretation to describe the outcomes of position measurements, even at the level of equal time measurements. If one insists on the conservative interpretation originally intended by Bohm, the discrepancy between Bohmian and quantum mechanical predictions permits one to test which theory is favored by nature. The HRE scenario seems to be perfectly suited for such a comparison, since it has the measurement times as external control parameters, which are thus freely choosable by the experimenter; moreover since it does not involve any concepts besides the free time evolution of matter particles and position measurements, it should not be too hard to determine the corresponding Bohmian trajectories.

A variant of the HRE scenario would implement **time-of-arrival measurements** in-

stead of position measurements. With respect to the Bell test, this means that the detector positions take the role of the control parameters. One expects that the resulting correlation function would be similar to (4.33). A thorough investigation, however, should take the measurement backaction into account, which potentially deformes the fringe pattern [82–86]. One might suspect a trade-off between measurement backaction and measurement resolution. The question whether this admits a Bell violation or not surely deserves further, more detailed investigation, since time-of-arrival measurements would constitute another fascinating possibility for the demonstration of nonclassicality in the motion, aside from possible experimental amenities.

As a final example, let me mention that one might discard the restriction to the dissociation of a single pair and consider the simultaneous dissociation of a multitude of molecules in a **multi-pair Bell setting** [111–113]. Statistical effects due to the indistinguishability of the particles then require a theoretical treatment of the dissociation process beyond the single-molecule dynamics. To this end, one expects that the two-body transition amplitude between molecular initial state and asymptotic dissociation state, which follows from Eq. (6.51), may serve as an essential building block.

To get an idea of such a Bell test, let us consider the (oversimplified) bosonic N-particle time-bin entangled state

$$|\Phi_N\rangle = \frac{1}{N!\sqrt{N+1}}(a_{\mathrm{E}}^\dagger b_{\mathrm{E}}^\dagger + a_{\mathrm{L}}^\dagger b_{\mathrm{L}}^\dagger)^N, \tag{9.1}$$

where a_{E} annihilates a particle in the mode corresponding to the early dissociation time and propagating to the left (similar for the other annihilation operators). In analogy to (3.4), the Mach-Zehnder interferometers then effect a transformation onto modes in the output ports ($c_\pm$ on the left side, $d_\pm$ on the right), $a_{\mathrm{E}}^\dagger \to \mathrm{e}^{i\varphi_1}(c_+^\dagger + c_-^\dagger)/\sqrt{2}$ and $a_{\mathrm{L}}^\dagger \to (c_+^\dagger - c_-^\dagger)/\sqrt{2}$ (and similar on the right side), in terms of which the scattered state $|\Phi_N'\rangle$ can be reformulated. One determines the probability to detect, say, n_1^+ particles in the $(+)$-port on the left side and n_2^+ particles in the $(+)$-port on the right side according to

$$P^{(N)}(n_1^+, n_2^+|\varphi_1, \varphi_2) = |\langle n_1^+, N-n_1^+, n_2^+, N-n_2^+|\Phi_N'\rangle|^2, \tag{9.2}$$

with $|n_1^+, n_1^-, n_2^+, n_2^-\rangle = (c_+^\dagger)^{n_1^+}(c_-^\dagger)^{n_1^-}(d_+^\dagger)^{n_2^+}(d_-^\dagger)^{n_2^-}|0\rangle/\sqrt{n_1^+ n_1^- n_2^+ n_2^-}$. This joint detection probability can be dichotomized by defining a threshold number $M \leqslant N$, such that detected particle numbers larger or equal to M are assigned to the outcome "+". In the case of $M < N$, one speaks of majority voting, $M = N$ is denoted unanimous voting. We thus get the dichotomic joint probability

$$P^{(N)}(+,-|\varphi_1, \varphi_2) = \sum_{n_1^+=M}^{N} \sum_{n_2^+=0}^{M-1} P^{(N)}(n_1^+, n_2^+|\varphi_1, \varphi_2), \tag{9.3}$$

and corresponding expressions for the other three combinations. For the many-particle TBE state (9.1) one finds that the resulting joint dichotomic probability indeed violates the CHSH inequality for appropriate (N-dependent) choices of the φ_i and for all threshold numbers M [112]. This demonstrates that a Bell violation in such a multi-pair Bell setting is, in principle, possible. It is considerably more involved, but certainly not impossible, to determine the true many-particle Feshbach dissociation state (in the case of $^6\mathrm{Li}_2$ for a mixture of fermionic species) and to verify its potential to violate a Bell inequality when taking the dispersion-reduced visibility into account.

Appendix A

A.1 Free time evolution in the dispersion-dominated limit

To gain the desired expression for an arbitrary (one-dimensional) wave packet in the limit where its shape is determined by its momentum distribution, we start by formulating the time-evolved wave packet $\langle x|\psi(t)\rangle$, as emerged from its initial state $\langle x|\psi(0)\rangle$, mediated by the free propagator $K_0(x,x',t) = \sqrt{m/2\pi i\hbar t}\exp[im(x-x')^2/2\hbar t]$ [114],

$$\begin{aligned}\langle x|\psi(t)\rangle &= \int_{-\infty}^{\infty} \mathrm{d}x' K_0(x,x',t)\langle x'|\psi(0)\rangle \\ &= \sqrt{\frac{m}{2\pi i\hbar t}}\int_{-\infty}^{\infty}\mathrm{d}x' \mathrm{e}^{im(x-x')^2/2\hbar t}\langle x'|\psi(0)\rangle. \end{aligned} \tag{A.1}$$

Since non-vanishing contributions to the integral are only expected in the vicinity of the mean initial position $\bar{x} = \langle\psi(t)|\hat{x}|\psi(t)\rangle|_{t=0}$ for a localized wave packet, we reformulate the square in the exponent accordingly,

$$(x-x')^2 = x^2 - \bar{x}^2 - 2(x-\bar{x})x' + (x'-\bar{x})^2 \tag{A.2}$$

which permits one to rewrite the wave packet as

$$\begin{aligned}\langle x|\psi(t)\rangle &= \sqrt{\frac{m}{2\pi i\hbar t}}\mathrm{e}^{im(x^2-\bar{x}^2)/2\hbar t} \\ &\quad\times\int_{-\infty}^{\infty}\mathrm{d}x' \mathrm{e}^{-im(x-\bar{x})x'/\hbar t}\mathrm{e}^{im(x'-\bar{x})^2/2\hbar t}\langle x'|\psi(0)\rangle. \end{aligned} \tag{A.3}$$

We see that at sufficiently large times, $t \gg m\sigma_x^2/\hbar$, where σ_x denotes the initial position uncertainty, the second exponential evaluates to unity in the region of non-vanishing $\langle x|\psi(0)\rangle$, such that one can approximate

$$\langle x|\psi(t)\rangle \simeq \sqrt{\frac{m}{2\pi i\hbar t}}\mathrm{e}^{im(x^2-\bar{x}^2)/2\hbar t}\int_{-\infty}^{\infty}\mathrm{d}x' \mathrm{e}^{-im(x-\bar{x})x'/\hbar t}\langle x'|\psi(0)\rangle. \tag{A.4}$$

The final expression is obtained by identifying the integral with the momentum representation of the initial state,

$$\tilde{\psi}(p) = \langle p|\psi(0)\rangle = \int_{-\infty}^{\infty}\mathrm{d}x\langle p|x\rangle\langle x|\psi(0)\rangle = \int_{-\infty}^{\infty}\mathrm{d}x\frac{1}{\sqrt{2\pi\hbar}}\mathrm{e}^{-ipx/\hbar}\langle x|\psi(0)\rangle, \tag{A.5}$$

which yields

$$\langle x|\psi(t)\rangle \simeq \sqrt{\frac{m}{it}}\mathrm{e}^{im(x^2-\bar{x}^2)/2\hbar t}\,\tilde{\psi}\left(m(x-\bar{x})/t\right). \tag{A.6}$$

A.2 Scale separation

Let $\chi(x)$ be an oscillating function with the period λ. If we split the integral

$$I = \int_{-\infty}^{\infty} \mathrm{d}x \chi(x) E(x) \tag{A.7}$$

up into integrals over the wave length λ,

$$I = \sum_{n=0}^{\infty} \left\{ \int_{n\lambda}^{(n+1)\lambda} \mathrm{d}x \chi(x) E(x) - \int_{-n\lambda}^{-(n+1)\lambda} \mathrm{d}x \chi(x) E(x) \right\}, \tag{A.8}$$

and in addition assume that the envelope function $E(x)$ varies slowly on the scale λ (scale separation), we can pull the envelope function out of the integrals,

$$\begin{aligned} I &\approx \sum_{n=0}^{\infty} \left\{ E(n\lambda) \int_{n\lambda}^{(n+1)\lambda} \mathrm{d}x \chi(x) - E(-n\lambda) \int_{-n\lambda}^{-(n+1)\lambda} \mathrm{d}x \chi(x) \right\} \\ &= \sum_{n=0}^{\infty} \left\{ E(n\lambda) \int_{0}^{\lambda} \mathrm{d}x \chi(x) - E(-n\lambda) \int_{0}^{-\lambda} \mathrm{d}x \chi(x) \right\} \\ &= \sum_{n=0}^{\infty} \{E(n\lambda) + E(-n\lambda)\} \int_{0}^{\lambda} \mathrm{d}x \chi(x). \end{aligned} \tag{A.9}$$

Note that the second and the third line use the periodicity of $\chi(x)$. The remaining Riemann sum can be rewritten as integral according to

$$\int_0^{\infty} \mathrm{d}x E(x) \approx \lambda E(0) + \lambda E(\lambda) + \lambda E(2\lambda) + \ldots = \lambda \sum_{n=0}^{\infty} E(n\lambda), \tag{A.10}$$

yielding the final result

$$I \approx \int_{-\infty}^{\infty} \mathrm{d}x E(x) \frac{1}{\lambda} \int_0^{\lambda} \mathrm{d}x' \chi(x'). \tag{A.11}$$

A.3 Stationary phase approximation

Stationary phase approximation states that in the limit of large λ the integral

$$I(\lambda) = \int_a^b \mathrm{d}t f(t) \mathrm{e}^{i\lambda\Phi(t)} \tag{A.12}$$

gets its main contributions in the vicinity of the stationary points c_j of the real, twice differentiable function $\Phi(t)$. This suggests to expand $\Phi(t)$ to second order at the stationary points, and the real, integrable function $f(t)$ to zeroth order. Extending the range of integration to the entire real axis then yields

$$I(\lambda) \sim \sum_j \mathrm{e}^{i\lambda\Phi(c_j)} f(c_j) \sqrt{\frac{2\pi}{\lambda |\Phi''(c_j)|}} \mathrm{e}^{i(\pi/4)\mathrm{sgn}(\Phi''(c_j))}, \tag{A.13}$$

where we sum over all stationary points $\Phi'(c_j) = 0$, which are assumed to be isolated [105].

Evaluation for symmetric pulses We now consider the integral

$$\frac{\tilde{C}_0(\omega+E_0/\hbar)}{T} = \int_{-\infty}^{\infty} \mathrm{d}\tilde{t}\, \mathrm{e}^{i\varepsilon[(\omega T/\varepsilon)\tilde{t}-\phi(\tilde{t})]}, \tag{A.14}$$

with $\varepsilon \gg 1$. Taking $\phi(\tilde{t})$ to be anti-symmetric and strictly monotonically increasing and given that $\omega T/\varepsilon < \phi''_{\max}$ (only if this is satisfied one finds two (real) saddle points $\pm\tilde{t}_\omega$ of $\Phi(\tilde{t}) = (\omega T/\varepsilon)\tilde{t} - \phi(\tilde{t})$), one obtains

$$\begin{aligned} \frac{\tilde{C}_0(\omega+E_0/\hbar)}{T} &= \sum_{\sigma=\pm} \mathrm{e}^{i\varepsilon[(\omega T/\varepsilon)\sigma\tilde{t}_\omega - \sigma\phi(\tilde{t}_\omega)]} \sqrt{\frac{2\pi}{\varepsilon|\phi''(\tilde{t}_\omega)|}}\, \mathrm{e}^{i\sigma\pi/4} \\ &= \sqrt{\frac{8\pi}{\varepsilon|P'(\tilde{t}_\omega)|}} \cos\left[\omega T\tilde{t}_\omega - \varepsilon\phi(\tilde{t}_\omega) + \frac{\pi}{4}\right], \end{aligned} \tag{A.15}$$

where we identified $\phi''(\tilde{t}) = P'(\tilde{t})$ to render the influence of the pulse slope manifest.

A.4 Uniform asymptotic expansion

We adopt the notation from [105]. Consider a complex integral of the form

$$I(\lambda,\vec{\alpha}) = \int_C \mathrm{d}z\, g(z)\mathrm{e}^{\lambda w(z;\vec{\alpha})}, \tag{A.16}$$

where $w(z;\vec{\alpha})$ and $g(z)$ may denote analytic functions, λ be some large, real parameter, and C the integration contour. $\vec{\alpha} = (\alpha_+,\alpha_-)$, on the other hand, may represent two saddle points of $w(z;\vec{\alpha})$ lying in the vicinity of C. In the limit of large λ ($\lambda \to \infty$) one expects the main contributions to the integral to stem from the passage at these saddle points. We seek a uniform approximation of the integral that is valid even when the saddle points are nearby or coincide, a situation where ordinary stationary phase approximation fails. To this end, one substitutes $z \to t = t(z)$, such that $w(z;\vec{\alpha}) = -(t^3/3 - \gamma^2 t) + \rho$ and $t(\alpha_\pm) = \pm\gamma$. The existence of this transformation is guaranteed by the analyticity of w. The parameters γ and ρ then follow from

$$\begin{aligned} \frac{4\gamma^3}{3} &= w(\alpha_+;\vec{\alpha}) - w(\alpha_-;\vec{\alpha}), \\ \rho &= \frac{1}{2}\{w(\alpha_+;\vec{\alpha}) + w(\alpha_-;\vec{\alpha})\}. \end{aligned} \tag{A.17}$$

For large λ the integral thus reads as

$$I(\lambda,\vec{\alpha}) \sim \int\limits_{C_1\cap\hat{D}_{\vec{\alpha}}} \mathrm{d}t\, g(z(t))\frac{\mathrm{d}z}{\mathrm{d}t}\mathrm{e}^{\lambda[-(t^3/3-\gamma^2 t)+\rho]}, \tag{A.18}$$

where the integration is constrained to the transformed integration contour C_1 in the vicinity of the transformed saddle points. Expanding

$$G_0(t;\vec{\alpha}) := g(z(t))\frac{\mathrm{d}z}{\mathrm{d}t} = a_0 + a_1 t + (t^2-\gamma^2)H_0(t;\vec{\alpha}), \tag{A.19}$$

one can neglect the last term,

$$I(\lambda,\vec{\alpha}) \sim \mathrm{e}^{\lambda\rho} \int\limits_{C_1\cap\hat{D}_{\vec{\alpha}}} \mathrm{d}t\,(a_0 + a_1 t)\mathrm{e}^{-\lambda(t^3/3-\gamma^2 t)}, \tag{A.20}$$

since $H_0(t,\vec{\alpha})$ is regular at $t=\pm\gamma$. The coefficients are determined according to

$$\begin{aligned} a_0 &= \frac{1}{2}[G_0(\gamma;\vec{\alpha})+G_0(-\gamma;\vec{\alpha})], \\ a_1 &= \frac{1}{2\gamma}[G_0(\gamma;\vec{\alpha})-G_0(-\gamma;\vec{\alpha})]. \end{aligned} \tag{A.21}$$

The required derivative $\mathrm{d}z/\mathrm{d}t$, on the other hand, follows from de l'Hospital's rule,

$$\begin{aligned} \dot{z}^2|_{\substack{t=\pm\gamma \\ z=\alpha_\pm}} &= \frac{\mp 2\gamma}{w_{zz}(\alpha_\pm;\vec{\alpha})}; \quad \alpha_+\neq\alpha_-, \\ \dot{z}^3|_{\substack{t=\pm\gamma \\ z=\alpha_\pm}} &= \frac{-2}{w_{zzz}(\alpha_+;\vec{\alpha})}; \quad \alpha_+=\alpha_-. \end{aligned} \tag{A.22}$$

Using that $\mathrm{Ai}(x)=1/(2\pi i)\int_{C_1}\exp(sx-s^3/3)\mathrm{d}s$ and $\mathrm{Ai}'(x)=\partial_x\mathrm{Ai}(x)$ (the modification of the integration contour from $C_1\cap\hat{D}_{\vec{\alpha}}$ to C_1 introduces an asymptotically negligible error), one obtains

$$I(\lambda,\vec{\alpha})\sim 2\pi i\mathrm{e}^{\lambda\rho}[\frac{a_0}{\lambda^{1/3}}\mathrm{Ai}(\lambda^{2/3}\gamma^2)+\frac{a_1}{\lambda^{2/3}}\mathrm{Ai}'(\lambda^{2/3}\gamma^2)], \tag{A.23}$$

which represents the first term in an algebraic expansion with respect to $1/\lambda$. A detailed proof is given in [105].

Evaluation for error function In our case we have

$$\frac{\tilde{C}_0(\omega+E_0/\hbar)}{T}=\int_{-\infty}^{\infty}\mathrm{d}\tilde{t}\mathrm{e}^{\varepsilon i[(\omega T/\varepsilon)\tilde{t}-\mathrm{erf}(\tilde{t})]}, \tag{A.24}$$

which allows us to identify $w(z;\beta)=i[\beta z-\mathrm{erf}(z)]$, yielding the saddle points

$$\alpha_\pm=\begin{cases} \pm\sqrt{-\ln(\sqrt{\pi}\beta/2)}, \beta<2/\sqrt{\pi} \\ \pm i\sqrt{\ln(\sqrt{\pi}\beta/2)}, \beta>2/\sqrt{\pi} \end{cases}. \tag{A.25}$$

Since $\alpha_-=-\alpha_+$, $w(-z)=-w(z)$ and $g(z)\equiv 1$, one finds $\rho=0$, $a_1=0$, $\gamma^3=(3/2)w(\alpha_+;\beta)$ and $a_0^2=-2\gamma/w_{zz}(\alpha_+;\beta)$ for $\alpha_+\neq\alpha_-$ ($a_0^3=-2/w_{zzz}(\alpha_+;\beta)$ for $\alpha_+=\alpha_-$), where we choose the roots such that the final result is real.

Bibliography

[1] D. Bohm. A suggested interpretation of the quantum theory in terms of "hidden" variables. I and II. *Phys. Rev.*, 85:166–193, 1952.

[2] D. Bohm and B. J. Hiley. *The Undivided Universe: An Ontological Interpretation of Quantum Theory*. Routledge, 1993.

[3] G. C. Ghirardi, A. Rimini, and T. Weber. Unified dynamics for microscopic and macroscopic systems. *Phys. Rev. D*, 34:470–491, 1986.

[4] A. Bassi and G. Ghirardi. Dynamical reduction models. *Phys. Rep.*, 379:257 – 426, 2003.

[5] H. Everett. "Relative state" formulation of quantum mechanics. *Rev. Mod. Phys.*, 29:454–462, 1957.

[6] H.D. Zeh. On the interpretation of measurement in quantum theory. *Found. Phys.*, 1:69–76, 1970.

[7] W. H. Zurek. Pointer basis of quantum apparatus: Into what mixture does the wave packet collapse? *Phys. Rev. D*, 24:1516–1525, 1981.

[8] D. Giulini, E. Joos, C. Kiefer, J. Kupsch, I. O. Stamatescu, and H. D. Zeh. *Decoherence and the appearance of a classical world in quantum theory*. Springer, Berlin, 1996.

[9] M. A. Schlosshauer. *Decoherence and the quantum-to-classical transition*. Springer, 2007.

[10] J. F. Sherson, H. Krauter, R. K. Olsson, B. Julsgaard, K. Hammerer, I. Cirac, and E. S. Polzik. Quantum teleportation between light and matter. *Nature*, 443:557–60, 2006.

[11] S. Gleyzes, S. Kuhr, C. Guerlin, J. Bernu, S. Deléglise, U. B. Hoff, M. Brune, J. M. Raimond, and S. Haroche. Quantum jumps of light recording the birth and death of a photon in a cavity. *Nature*, 446:297–300, 2007.

[12] M. Halder, A. Beveratos, N. Gisin, V. Scarani, C. Simon, and H. Zbinden. Entangling independent photons by time measurement. *Nat. Phys.*, 3:692–695, 2007.

[13] D. L. Moehring, P. Maunz, S. Olmschenk, K. C. Younge, D. N. Matsukevich, L. M. Duan, and C. Monroe. Entanglement of single-atom quantum bits at a distance. *Nature*, 449:68–71, 2007.

[14] M. Aspelmeyer and K. Schwab. Focus on mechanical systems at the quantum limit. *New J. Phys.*, 10:095001, 2008.

[15] C. Monroe, D. M. Meekhof, B. E. King, and D. J. Wineland. A"Schrödinger cat" superposition state of an atom. *Science*, 272:1131, 1996.

[16] J. M. Raimond, M. Brune, and S. Haroche. Manipulating quantum entanglement with atoms and photons in a cavity. *Rev. Mod. Phys.*, 73:565–582, 2001.

[17] W. Tittel, J. Brendel, H. Zbinden, and N. Gisin. Violation of Bell inequalities by photons more than 10 km apart. *Phys. Rev. Lett.*, 81:3563–3566, 1998.

[18] R. Ursin, F. Tiefenbacher, T. Schmitt-Manderbach, H. Weier, T. Scheidl, M. Lindenthal, B. Blauensteiner, T. Jennewein, J. Perdigues, P. Trojek, et al. Entanglement-based quantum communication over 144 km. *Nat. Phys.*, 3:481–486, 2007.

[19] M. A. Rowe, D. Kielpinski, V. Meyer, C. A. Sackett, W. M. Itano, C. Monroe, and D. J. Wineland. Experimental violation of a Bell's inequality with efficient detection. *Nature*, 409:791–794, 2001.

[20] R. Blatt and D. Wineland. Entangled states of trapped atomic ions. *Nature*, 453:1008–1015, 2008.

[21] M. Arndt, O. Nairz, J. Vos-Andreae, C. Keller, G. van der Zouw, and A. Zeilinger. Wave–particle duality of C_{60} molecules. *Nature*, 401:680–682, 1999.

[22] S. Gerlich, L. Hackermüller, K. Hornberger, A. Stibor, H. Ulbricht, M. Gring, F. Goldfarb, T. Savas, M. Müri, M. Mayor, and M. Arndt. A Kapitza-Dirac-Talbot-Lau interferometer for highly polarizable molecules. *Nat. Phys.*, 3:711–715, 2007.

[23] E. A. Donley, N. R. Claussen, S. T. Thompson, and C. E. Wieman. Atom-molecule coherence in a Bose-Einstein condensate. *Nature*, 417:529–533, 2002.

[24] J. Cubizolles, T. Bourdel, S. J. J. M. F. Kokkelmans, G. V. Shlyapnikov, and C. Salomon. Production of long-lived ultracold Li_2 molecules from a Fermi gas. *Phys. Rev. Lett.*, 91:240401, 2003.

[25] S. Jochim, M. Bartenstein, A. Altmeyer, G. Hendl, S. Riedl, C. Chin, J. Hecker Denschlag, and R. Grimm. Bose-Einstein condensation of molecules. *Science*, 302:2101–2103, 2003.

[26] C. A. Regal, C Ticknor, J. L. Bohn, and D. S. Jin. Creation of ultracold molecules from a Fermi gas of atoms. *Nature*, 424:47–50, 2003.

[27] M. Greiner, C. A. Regal, and D. S. Jin. Emergence of a molecular Bose-Einstein condensate from a Fermi gas. *Nature*, 426:537–540, 2003.

[28] K. E. Strecker, G. B. Partridge, and R. G. Hulet. Conversion of an atomic Fermi gas to a long-lived molecular Bose gas. *Phys. Rev. Lett.*, 91:080406, 2003.

[29] S. Dürr, T. Volz, A. Marte, and G. Rempe. Observation of molecules produced from a Bose-Einstein condensate. *Phys. Rev. Lett.*, 92:020406, 2004.

[30] J. Herbig, T. Kraemer, M. Mark, T. Weber, C. Chin, H. C. Nagerl, and R. Grimm. Preparation of a pure molecular quantum gas. *Science*, 301:1510–1513, 2003.

[31] K. Xu, T. Mukaiyama, J. R. Abo-Shaeer, J. K. Chin, D. E. Miller, and W. Ketterle. Formation of quantum-degenerate sodium molecules. *Phys. Rev. Lett.*, 91:210402, 2003.

[32] T. Mukaiyama, J. R. Abo-Shaeer, K. Xu, J. K. Chin, and W. Ketterle. Dissociation and decay of ultracold sodium molecules. *Phys. Rev. Lett.*, 92:180402, 2004.

[33] S. Dürr, T. Volz, and G. Rempe. Dissociation of ultracold molecules with Feshbach resonances. *Phys. Rev. A*, 70:031601, 2004.

[34] K. M. Jones, E. Tiesinga, P. D. Lett, and P. S. Julienne. Ultracold photoassociation spectroscopy: Long-range molecules and atomic scattering. *Rev. Mod. Phys.*, 78:483–535, 2006.

[35] C. Gneiting and K. Hornberger. Bell test for the free motion of material particles. *Phys. Rev. Lett.*, 101:260503, 2008.

[36] C. Gneiting and K. Hornberger. Nonclassical correlations from dissociation-time entanglement. *Appl. Phys. B*, 95:237, 2009.

[37] C. Gneiting and K. Hornberger. Molecular Feshbach dissociation as a source for motionally entangled atoms. *Phys. Rev. A*, 81:013423, 2010.

[38] C. Gneiting and K. Hornberger. Entangling the free motion of a particle pair: an experimental scenario. *Opt. Spectrosc.*, 108:188–196, 2010.

[39] J. S. Bell. On the Einstein-Podolsky-Rosen paradox. *Physics*, 1:195, 1964.

[40] J. F. Clauser, M. A. Horne, A. Shimony, and R. A. Holt. Proposed experiment to test local hidden-variable theories. *Phys. Rev. Lett.*, 23:880–884, 1969.

[41] A. Aspect, J. Dalibard, and G. Roger. Experimental test of Bell's inequalities using time-varying analyzers. *Phys. Rev. Lett.*, 49:1804–1807, 1982.

[42] S. Kochen and E. P. Specker. The problem of hidden variables in quantum mechanics. *J. Math. Mech.*, 17:59–87, 1967.

[43] Y.-F. Huang, C.-F. Li, Y.-S. Zhang, J.-W. Pan, and G.-C. Guo. Experimental test of the Kochen-Specker theorem with single photons. *Phys. Rev. Lett.*, 90:250401, 2003.

[44] H. Bartosik, J. Klepp, C. Schmitzer, S. Sponar, A. Cabello, H. Rauch, and Y. Hasegawa. Experimental test of quantum contextuality in neutron interferometry. *Phys. Rev. Lett.*, 103:040403, 2009.

[45] A. J. Leggett and A. Garg. Quantum mechanics versus macroscopic realism: Is the flux there when nobody looks? *Phys. Rev. Lett.*, 54:857–860, 1985.

[46] L. Hardy. Quantum mechanics, local realistic theories, and Lorentz-invariant realistic theories. *Phys. Rev. Lett.*, 68:2981–2984, 1992.

[47] A. J. Leggett. Nonlocal hidden-variable theories and quantum mechanics: An incompatibility theorem. *Found. Phys.*, 33:1469–1493, 2003.

[48] S. Groblacher, T. Paterek, R. Kaltenbaek, C. Brukner, M. Żukowski, M. Aspelmeyer, and A. Zeilinger. An experimental test of non-local realism. *Nature*, 446:871, 2007.

[49] C. Branciard, A. Ling, N. Gisin, C. Kurtsiefer, A. Lamas-Linares, and V. Scarani. Experimental falsification of Leggett's nonlocal variable model. *Phys. Rev. Lett.*, 99:210407, 2007.

[50] H. M. Wiseman. From Einstein's theorem to Bell's theorem: a history of quantum non-locality. *Contemp. Phys.*, 47:79–88, 2006.

[51] D. Dürr and S. Teufel. *Bohmian Mechanics: The Physics and Mathematics of Quantum Theory*. Springer, 2009.

[52] E. Schrödinger. Discussion of probability relations between separated systems. *Proc. Camb. Phil. Soc.*, 31:555–563, 1935.

[53] A. Einstein, B. Podolsky, and N. Rosen. Can quantum-mechanical description of physical reality be considered complete? *Phys. Rev.*, 47:777–780, 1935.

[54] D. Bohm and Y. Aharonov. Discussion of experimental proof for the paradox of Einstein, Rosen, and Podolsky. *Phys. Rev.*, 108:1070–1076, 1957.

[55] A. Fine. Joint distributions, quantum correlations, and commuting observables. *J. Math. Phys.*, 23:1306–1310, 1982.

[56] B. S. Cirel'son. Quantum generalizations of Bell's inequality. *Lett. Math. Phys.*, 4:93–100, 1980.

[57] M. Pawlowski, T. Paterek, D. Kaszlikowski, V. Scarani, A. Winter, and M. Zukowski. Information causality as a physical principle. *Nature*, 461:1101–1104, 2009.

[58] S. Popescu and D. Rohrlich. Quantum nonlocality as an axiom. *Found. Phys.*, 24:379–385, 1994.

[59] Ll. Masanes, A. Acin, and N. Gisin. General properties of nonsignaling theories. *Phys. Rev. A*, 73:012112, 2006.

[60] H. Barnum, J. Barrett, M. Leifer, and A. Wilce. Generalized no-broadcasting theorem. *Phys. Rev. Lett.*, 99:240501, 2007.

[61] J. Barrett, L. Hardy, and A. Kent. No signaling and quantum key distribution. *Phys. Rev. Lett.*, 95:010503, 2005.

[62] P. Skrzypczyk, N. Brunner, and S. Popescu. Emergence of quantum correlations from nonlocality swapping. *Phys. Rev. Lett.*, 102:110402, 2009.

[63] Wim van Dam. Implausible consequences of superstrong nonlocality. *arXiv:quant-ph/0501159*, 2005.

[64] S. J. Freedman and J. F. Clauser. Experimental test of local hidden-variable theories. *Phys. Rev. Lett.*, 28:938–941, 1972.

[65] G. Weihs, T. Jennewein, C. Simon, H. Weinfurter, and A. Zeilinger. Violation of Bell's inequality under strict Einstein locality conditions. *Phys. Rev. Lett.*, 81:5039–5043, 1998.

[66] Z.-B. Chen, J.-W. Pan, G. Hou, and Y.-D. Zhang. Maximal violation of Bell's inequalities for continuous variable systems. *Phys. Rev. Lett.*, 88:040406, 2002.

[67] K. Banaszek and K. Wodkiewicz. Nonlocality of the Einstein-Podolsky-Rosen state in the Wigner representation. *Phys. Rev. A*, 58:4345–4347, 1998.

[68] H. Nha and H. J. Carmichael. Proposed test of quantum nonlocality for continuous variables. *Phys. Rev. Lett.*, 93:020401, 2004.

[69] M. Revzen, P. A. Mello, A. Mann, and L. M. Johansen. Bell's inequality violation with non-negative Wigner functions. *Phys. Rev. A*, 71:022103, 2005.

[70] R. W. Spekkens. Negativity and contextuality are equivalent notions of nonclassicality. *Phys. Rev. Lett.*, 101:020401, 2008.

[71] T. Opatrný and G. Kurizki. Matter-wave entanglement and teleportation by molecular dissociation and collisions. *Phys. Rev. Lett.*, 86:3180–3183, 2001.

[72] K. V. Kheruntsyan, M. K. Olsen, and P. D. Drummond. Einstein-Podolsky-Rosen correlations via dissociation of a molecular Bose-Einstein condensate. *Phys. Rev. Lett.*, 95:150405, 2005.

[73] K. V. Kheruntsyan. Quantum atom optics with fermions from molecular dissociation. *Phys. Rev. Lett.*, 96:110401, 2006.

[74] N. D. Mermin. Extreme quantum entanglement in a superposition of macroscopically distinct states. *Phys. Rev. Lett.*, 65:1838–1840, 1990.

[75] S. L. Braunstein and C. M. Caves. Wringing out better Bell inequalities. *Ann. Phys.*, 202:22 – 56, 1990.

[76] E. G. Cavalcanti, C. J. Foster, M. D. Reid, and P. D. Drummond. Bell inequalities for continuous-variable correlations. *Phys. Rev. Lett.*, 99:210405, 2007.

[77] Q. Y. He, E. G. Cavalcanti, M. D. Reid, and P. D. Drummond. Testing for multipartite quantum nonlocality using functional Bell inequalities. *Phys. Rev. Lett.*, 103:180402, 2009.

[78] J. Brendel, N. Gisin, W. Tittel, and H. Zbinden. Pulsed energy-time entangled twin-photon source for quantum communication. *Phys. Rev. Lett.*, 82:2594–2597, 1999.

[79] J. D. Franson. Bell inequality for position and time. *Phys. Rev. Lett.*, 62:2205–2208, 1989.

[80] W. Tittel, J. Brendel, H. Zbinden, and N. Gisin. Quantum cryptography using entangled photons in energy-time Bell states. *Phys. Rev. Lett.*, 84:4737–4740, 2000.

[81] C. Simon and J. P. Poizat. Creating single time-bin-entangled photon pairs. *Phys. Rev. Lett.*, 94:030502, 2005.

[82] G. R. Allcock. The time of arrival in quantum mechanics. *Ann. Phys.*, 53:253–348, 1969.

[83] R. Werner. Screen observables in relativistic and nonrelativistic quantum mechanics. *J. Math. Phys.*, 27:793, 1986.

[84] Y. Aharonov, J. Oppenheim, S. Popescu, B. Reznik, and W. G. Unruh. Measurement of time of arrival in quantum mechanics. *Phys. Rev. A*, 57:4130–4139, 1998.

[85] J. G. Muga and C. R. Leavens. Arrival time in quantum mechanics. *Phys. Rep.*, 338:353–438, 2000.

[86] J. A. Damborenea, I. L. Egusquiza, G. C. Hegerfeldt, and J. G. Muga. Measurement-based approach to quantum arrival times. *Phys. Rev. A*, 66:052104, 2002.

[87] J. R. Taylor. *Scattering Theory: The Quantum Theory on Nonrelativistic Collisions*. Wiley New York, 1972.

[88] S. Aerts, P. Kwiat, J.-Å. Larsson, and M. Żukowski. Two-photon Franson-type experiments and local realism. *Phys. Rev. Lett.*, 83:2872–2875, 1999.

[89] A. Cabello, A. Rossi, G. Vallone, F. De Martini, and P. Mataloni. Proposed Bell experiment with genuine energy-time entanglement. *Phys. Rev. Lett.*, 102:040401, 2009.

[90] J. Kiukas and R. F. Werner. Maximal violation of Bell inequalities by position measurements. *arXiv:0912.3740v1*, 2009.

[91] R. Bucker, A. Perrin, S. Manz, T. Betz, C. Koller, T. Plisson, J. Rottmann, T. Schumm, and J. Schmiedmayer. Single-particle-sensitive imaging of freely propagating ultracold atoms. *New J. Phys.*, 11:103039, 2009.

[92] J. F. Clauser and A. Shimony. Bell's theorem. experimental tests and implications. *Rep. Prog. Phys.*, 41:1881–1927, 1978.

[93] N. Gisin. Hidden quantum nonlocality revealed by local filters. *Phys. Lett. A*, 210:151 – 156, 1996.

[94] D. W. Berry, H. Jeong, M. Stobińska, and T. C. Ralph. The standard fair sampling assumption is not necessary to test local realism. *arXiv:0712.2490v2*, 2009.

[95] T. Volz, N. Syassen, D. M. Bauer, E. Hansis, S. Dürr, and G. Rempe. Preparation of a quantum state with one molecule at each site of an optical lattice. *Nat. Phys.*, 2:692–695, 2006.

[96] L. Mandel and E. Wolf. *Optical coherence and quantum optics*. Camb. Univ. Pr., 1995.

[97] J. D. Jackson. *Classical electrodynamics*. Wiley, 1962.

[98] D. R. Lide. *CRC handbook of chemistry and physics*. CRC press, 1993.

[99] T. M. Hanna, K. Góral, E. Witkowska, and T. Köhler. Classification of zero-energy resonances by dissociation of Feshbach molecules. *Phys. Rev. A*, 74:023618, 2006.

[100] T. Köhler, K. Góral, and P. S. Julienne. Production of cold molecules via magnetically tunable Feshbach resonances. *Rev. Mod. Phys.*, 78:1311–1361, 2006.

[101] N. Nygaard, R. Piil, and K. Mølmer. Two-channel Feshbach physics in a structured continuum. *Phys. Rev. A*, 78:023617, 2008.

[102] F. H. Mies, E. Tiesinga, and P. S. Julienne. Manipulation of Feshbach resonances in ultracold atomic collisions using time-dependent magnetic fields. *Phys. Rev. A*, 61:022721, 2000.

[103] E. Timmermans, P. Tommasini, M. Hussein, and A. Kerman. Feshbach resonances in atomic Bose-Einstein condensates. *Phys. Rep.*, 315:199–230, 1999.

[104] M. Olshanii. Atomic scattering in the presence of an external confinement and a gas of impenetrable bosons. *Phys. Rev. Lett.*, 81:938–941, 1998.

[105] N. Bleistein and R. Handelsman. *Asymptotic Expansions of Integrals*. Dover, 1986.

[106] C. S. Adams, M. Siegel, and J. Mlynek. Atom optics. *Phys. Rep.*, 240:143–210, 1994.

[107] H. Kreutzmann, U. V. Poulsen, M. Lewenstein, R. Dumke, W. Ertmer, G. Birkl, and A. Sanpera. Coherence properties of guided-atom interferometers. *Phys. Rev. Lett.*, 92:163201, 2004.

[108] C. H. Bennett, G. Brassard, C. Crepeau, R. Jozsa, A. Peres, and W. K. Wootters. Teleporting an unknown quantum state via dual classical and Einstein-Podolsky-Rosen channels. *Phys. Rev. Lett.*, 70:1895–1899, 1993.

[109] D. Bouwmeester, J. W. Pan, K. Mattle, M. Eibl, H. Weinfurter, and A. Zeilinger. Experimental quantum teleportation. *Nature*, 390:575–579, 1997.

[110] M. Correggi and G. Morchio. Quantum mechanics and stochastic mechanics for compatible observables at different times. *Ann. Phys.*, 296:371 – 389, 2002.

[111] M. D. Reid, W. J. Munro, and F. De Martini. Violation of multiparticle Bell inequalities for low- and high-flux parametric amplification using both vacuum and entangled input states. *Phys. Rev. A*, 66:033801, 2002.

[112] J.-D. Bancal, C. Branciard, N. Brunner, N. Gisin, S. Popescu, and C. Simon. Testing a Bell inequality in multipair scenarios. *Phys. Rev. A*, 78:062110, 2008.

[113] W. J. Mullin and F. Laloë. Interference of Bose-Einstein condensates: Quantum nonlocal effects. *Phys. Rev. A*, 78:061605, 2008.

[114] J. J. Sakurai. *Modern quantum mechanics*. Addison-Wesley, 1985.